# Aspects of Tachyon Field Cosmology


## Avinash Singh


*A thesis submitted for the partial fulfillment of*

*the degree of Doctor of Philosophy*



Department of Physical Sciences,

Indian Institute of Science Education and Research Mohali

Knowledge city, Sector 81, SAS Nagar, Manauli PO, Mohali 140306, Punjab, India.


June, 2020

# Declaration

The work presented in this thesis has been carried out by me under the guidance of Dr. Harvinder Kaur Jassal at the Indian Institute of Science Education and Research, Mohali. This work has not been submitted in part or in full for a degree, a diploma, or a fellowship to any other university or institute. Whenever contributions of others are involved, every effort is made to indicate this clearly, with due acknowledgment of collaborative research and discussions. This thesis is a bona fide record of original work done by me and all sources listed within have been detailed in the bibliography.

Avinash Singh
(candidate)

In my capacity as the supervisor of the candidate's thesis work, I certify that the above statements by the candidate are true to the best of my knowledge.

Harvinder Kaur Jassal
(Supervisor)

# *Acknowledgements*

*At this moment of accomplishment, first of all, I would like to express my sincere gratitude towards my thesis supervisor Dr. Harvinder Kaur Jassal, for her constant and unwavering guidance during my thesis work and for sharing her valuable insights of cosmology with me. The thing I admire most is the freedom she gave me to explore on my own and, at the same time, the guidance to recover when my steps faltered. I shall remain forever indebted for her patience, support, and encouragement, which has helped me to finish my dissertation in time.*

*I would like to acknowledge my thesis committee members, Prof. Jasjeet Singh Bagla, Dr. Smriti Mahajan, and Dr. Kinjalk Lochan, for their valuable comments and suggestions on my research work, manuscripts, and thesis. A special thanks to Prof. Jasjeet Singh Bagla, whose course work and project have polished my theoretical knowledge and computational skills. That project was the actual starting point of the path, which led me to the completion of my thesis work. I also admire him for discussions on cosmology, physics in general, and many academic or non-academic issues.*

*I want to thank my collaborators, Dr. Archana Sangwan and Dr. Manabendra Sharma, for their help, suggestions, and comments which helped me to complete the projects on time.*

*I acknowledge IISER, Mohali for the fellowship, funding, and all other facilities. I am also thankful to the High-Performance Computing facility at IISER, Mohali, which made it possible to achieve my projects' goals.*

*In the campus, I find myself very lucky to have friendship and bonding with some fantastic personalities. I enjoyed the company of my friends, Dr. Ankit Singh, Arnob Mukherjee, Dr. Sudhanshu Shekhar Chaurasia, Priyanka Madhu, Dr. Pooja Munjal, Dr. Satyam Ravi, and Dr. Swagatam Nayak during this period. Our discussion on scientific, social, and political issues with cups of tea, often in the evening, was my favorite time pass. I am also thankful to my friends, Manvendra, Ranbir, Ashish, Sandeep, and Swati, with whom I enjoyed a stress-free and comfortable environment in our scholar room. We often discuss cosmology and physics in general which helped me a lot to understand the subject better. I am also grateful to my friends Deepak, Ramu, Shyam, Anirban, Jaskaran, Jyotsana, Shekhar, Ritesh, Shalendar, Amit, Anzar, Aslam, Anshu, Shubhendu, Mayank, Sudipta and Sumit for their excellent company. I would also like to extend my gratitude to my undergraduate and master's friends, Pradeep, Satendra,*

*Deepak, Abhishek, Sandeep, Sanjay, Manju, Neelam, Kusum, Kiran, Shalinta, Sarita, Priya, Sumanta, and Malay for their valuable friendship, affection, and support.*

*My success and achievements would not have been possible without the constant love and support of my family. It is not possible to express in words the debt and gratitude I owe to my parents, Shri Deomuni Singh and Smt. Kalawati Devi. I shall forever be remain grateful to them for their love, care, blessings, and sacrifices they made for me. I would also like to thank my sisters, Late Smt. Krishna Kushwaha, Smt. Bindu Singh, Smt. Kiran Singh, my elder brother, Mr. Ajay Singh and sister-in-law, Smt. Babita Devi for their love, support, and constant encouragement through all ups and downs in my life. I also thank my nephews, nieces, and other family members for their love and support. Without them, I could not have fulfilled my dreams and achieved what I have achieved today.*

# Abstract

Observations have established that more than two-thirds of the energy density of the Universe is due to the contribution of dark energy. Dark energy accounts for the observed late-time acceleration of the universe. The nature of dark energy is, as yet, a mystery. To understand the nature of dark energy many models have been proposed, the simplest and the most favoured being the cosmological constant model ($\Lambda CDM$ model). The agent for cosmological constant is the energy density of the vacuum, and it remains constant throughout the evolution of the Universe. This simple explanation costs us some serious theoretical problems like 'the fine-tuning and the coincidence problem'. The $\Lambda CDM$ model also suffers from some observational inconsistencies between independent observations. There is a tension between the Planck observations and the other independent growth rate measurements in estimation of cosmological parameters. These facts motivate us to go for dynamical dark energy models, e.g., canonical and non-canonical dark energy models.

In this thesis, we have studied a particular scalar field dark energy model known as tachyon dark energy, and compared it with the cosmological constant and other dark energy models. This is a viable model in cosmology, and it has been shown that the tachyon scalar field can effectively explain dark energy. In this analysis, using low redshift distance measurement data, we obtain constraints on tachyon field parameters by way of combining these datasets. Our motivation is to compare the constraints on the tachyon models from previous studies using the same datasets and to check if the non-canonical scalar field models prefer different combinations of cosmological parameters. We find that constraints on tachyon models are stringent and these are as good as the $\Lambda CDM$ model to satisfy the low redshift data we have used.

Background data alone can not rule out degeneracy between different models. We study the effect of perturbations in tachyon dark energy in order to get constraints on parameters from observations other than distance measurements. We analyze the dynamics and nature of tachyon perturbations and their effect on the evolution of matter clustering. Calculating the linear growth rate of matter clustering, we compare our theoretical predictions with growth rate measurements. For tachyon models, the tension between the Planck observation and growth rate measurement is reduced. We find that dark energy perturbations are insignificant with respect to matter clustering at sub-Hubble scales, and dark energy can be considered homogeneous. However, at Hubble and super-Hubble scales, dark energy perturbations are significant when compared to the matter perturbation.

## List of Publications

- Avinash Singh, Archana Sangwan, H.K. Jassal, *Low redshift observational constraints on tachyon models of dark energy*, JCAP **04** (2019) 047.

- Avinash Singh, H. K. Jassal, Manabendra Sharma, *Perturbations in tachyon dark energy and their effect on matter clustering*, JCAP **05** (2020) 008.

# Contents

# Chapter 1

# Introduction

The cosmos is a large lab to test our current knowledge of physics. A cosmologist attempts to describe what is there in the Universe, how it is distributed, and how it is moving. We gather light (electromagnetic radiation) from distant galaxies and clusters in our instruments, and recreate a picture of our past universe. Cosmologists then try to explain these observations based on current knowledge of physics, and make any modification if needed. In the last two decades, human capability to observe the Universe has improved significantly. It is possible to cover a large range of the electromagnetic band, from radio to X-rays and gamma-rays. In near future, it will also be possible to take a snapshot of our universe using gravitational waves.

When we map our universe at higher redshifts (earlier in time), we find that the currently observable part of the universe was much smaller, extremely hot and dense. This suggests that the Universe originated from an explosion (the 'Hot Big Bang theory', HBB). This was followed by an inflationary era. During this era, the Universe expanded exponentially for a tiny fraction of a second. Evidence of HBB and inflation comes from observation of the 'Cosmic Microwave Background' (CMB) which is the relic radiation from the HBB. Small fluctuations (of the oder of $10^{-5}$) in otherwise isotropic CMB suggest that the seeds for structure formation in the Universe were planted during inflation. Once the inflationary era ended, the Universe entered a decelerating phase of radiation and subsequently a phase of matter domination. During the matter dominated era all the structures of the Universe, e.g. galaxies, clusters of galaxies and super-cluster were formed.

The present time is an era of high-precision data and large-scale surveys. With this technological advantage, it is discovered that the Universe is accelerating its expansion at present. In late 1990s, two teams, the Supernova Cosmology Project [4]

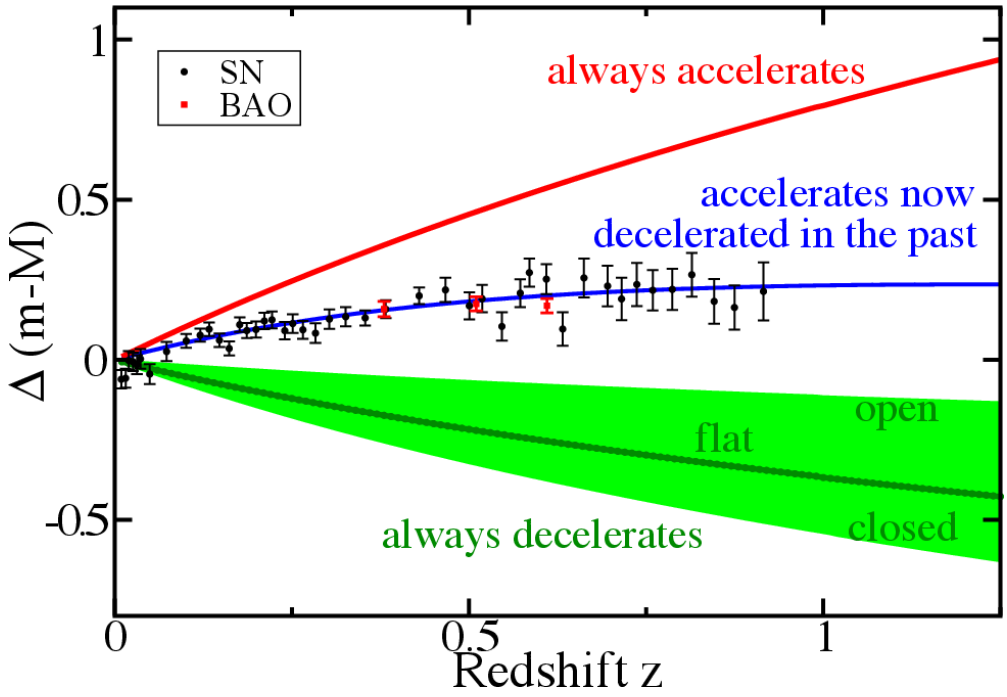


Figure 1.1: Distance modulus vs redshift plot as an evidence for the transition from deceleration in the past to acceleration today. Black data points are SN Ia data from the Supercal compilation [1], whereas the read data points are extracted from recent BAO measurements (BOSS DR12) [2]. Green area represents models for flat, closed and open universe with only matter ( $0.3 \leq \Omega_m \leq 1.5$ ). Red curve is for the model in which the Universe always accelerates ( $\Lambda$-only models ). Finally, the blue curve represents the model which fit the data well, and in which expansion of the Universe makes a transition from decelerating phase to an accelerating one at lower redshift. Image credit - Huterer and Shafer (2017) [3]. License agreement to reuse this figure is in appendix A.

and the High-z Supernova Search Team [5] discovered it independently. Later, this discovery was also confirmed by other observations, e.g. observations of Baryon Acoustic Oscillations (BAO), Cosmic Microwave Background, etc. This discovery ruled out many existing models of expanding universe at that time, and it became clear that only those models will be favored by the data which exhibit a low redshift accelerated expansion after the decelerating phases. From figure 1.1, it is clear that models in which the Universe is always decelerating ( e.g. flat, open and closed universe models with only matter ), or always accelerating models ( $\Lambda$-only models ), are ruled out entirely [3].

Explanation of late-time accelerated expansion requires more than two-thirds of the energy density of the Universe to be made up of an exotic negative pressure medium, called 'dark energy'. The challenge is to explain the origin, nature, and behavior of this component. The equation of state parameter $w$, the ratio of pressure to energy density, is a key parameter in the study of dark energy. At present, many

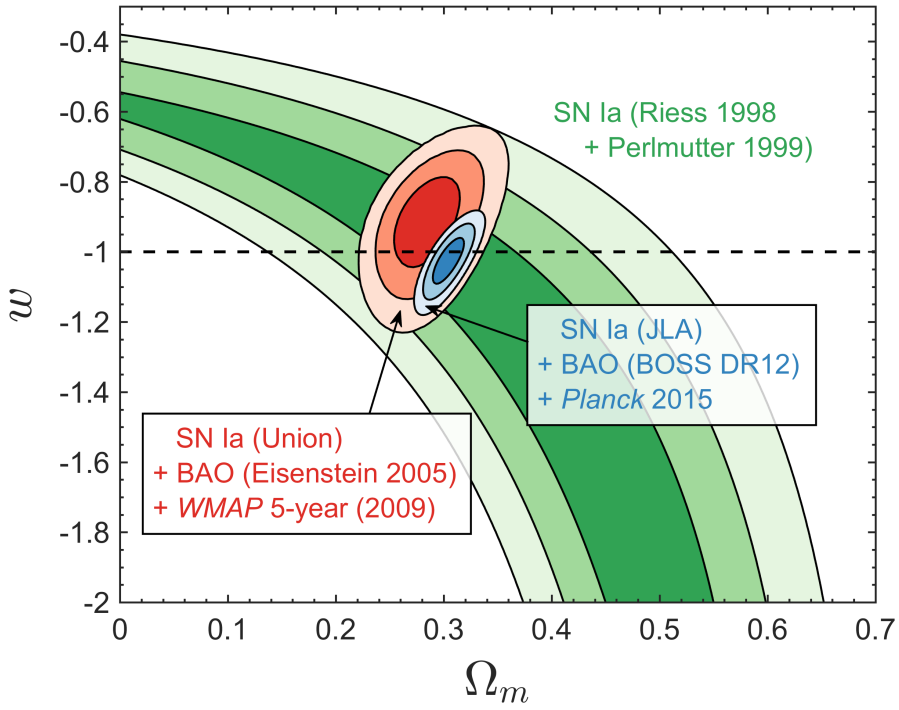


Figure 1.2: Evolution history of constraints on parameter space in $\Omega_m - w$ plane, assuming a flat universe such that $\Omega_{de} = 1 - \Omega_m$. Image credit - Huterer and Shafer (2017) [3]. License agreement to reuse this figure is in appendix A.

models exist. The simplest and the most favored being the cosmological constant model ($\Lambda CDM$ model) [6, 7, 8]. The cosmological constant is the energy density of the vacuum, and it remains a constant. The equation of state parameter for this component is given by $w = -1$. This simple explanation comes at the cost of some serious theoretical problems like 'the fine-tuning and the coincidence problem' [8]. Therefore, cosmologists need to search for alternatives to this model. One of the main goals in modern cosmology is to find the true value of the equation of state parameter and deviation, however small, from $-1$. At present many large surveys, e.g. the Dark Energy Survey (DES), are specially dedicated to achieve this purpose. In figure 1.2, a history of evolution of constraints on $w$ with another key cosmological parameter, present day value of matter density parameter $\Omega_m$, is shown. We can see that, in approximately two decades, with development of technology, constraints on parameter space of $w$–$\Omega_m$ plane has become significantly tighter. There still remains room for other cosmological models with $w \neq -1$.

Apart from the theoretical problems mentioned above, the $\Lambda CDM$ model suffers from tension between a few independent observations. The Planck mission has constrained the cosmological parameters for this model to a very high precision. On the other hand, we also have a robust set of 'growth-rate data' obtained from several surveys, e.g. SDSS, BOSS, WiggleZ, Euclid, LSST, etc. There is a discrepancy be-

tween the Planck observations and other independent growth rate measurements in estimation of cosmological parameters in the context of $\Lambda CDM$ model [9]. These include the estimation of the Hubble constant $H_0$, the root mean square matter power fluctuation in 8 $h^{-1}$ $Mpc$ radius $\sigma_8$, and the present day matter density parameter $\Omega_{m0}$. This problem persists for the constant $w$ model. These facts motivate us to go for dynamical dark energy models e.g., canonical and non-canonical dark energy models.

Dynamical dark energy models are an alternative to $\Lambda CDM$ model and typically have an evolving equation of state parameter. These models include the barotropic fluid models, canonical and non-canonical scalar field models, etc. A fluid dark energy equation of state parameter is considered to be a function of redshift or the scale factor. There are two key parameters, the present day value of the equation of state parameter $w_0$, and the value of its derivative $w_0'$. Detailed studies of the background evolution and constraints on the parameters for these models have been done in [10, 11, 12, 13, 14, 15, 16, 17]. Quintessence scalar field is also a candidate for dark energy. Using a slow rolling potential, the late-time accelerated expansion can be achieved. The equation of state parameter of this field is a function of time, and its value depends on the functional form of the potential term and the kinetic energy of the field. Quintessence models are broadly classified into 'freezing' and 'thawing' depending on whether the equation of the state parameter is approaching to a cosmological constant like value or departing from it. The background cosmology in the presence of the canonical scalar field has been studied in [18, 19, 20, 21, 22, 23, 24, 25]. The perturbations in the quintessence field, its dynamics, and its effect on the evolution of matter clustering have been studied in [26, 27, 28, 29].

Alternative to the canonical scalar field and the fluid model are the non-canonical scalar field models, e.g., the 'tachyon model' and the 'K-essence model'. The K-essence scalar fields were introduced as the K-inflation models by Armendariz-Picon [30]. This idea was extended as dynamical dark energy models to explain late-time accelerated expansion [31, 32, 33]. Tachyon scalar field arises as a decay mode of D-branes in string theory [34, 35, 36]. The background cosmology for this model has been studied in [37, 38, 39] and it is potentially a good candidate for dark energy. Tachyon scalar field has also been used to explain inflation [40, 41, 42, 43, 44, 45, 46, 47]. Since its equation of state becomes dust like in the course of time, it is also considered a viable candidate for dark matter [35, 36, 48, 49, 50, 51, 52]. The tachyon model is in good agreement with current observations; data puts tight constraints on cosmological parameters and the fine-tuning problem is less severe

than the cosmological constant model. Observations can not however completely distinguish this model from the $\Lambda CDM$ and other models. Perturbation in dark energy can potentially break the degeneracy between models, for instance via the Integrated Sachs-Wolf Effect (ISW effect) as it affects the low $l$ CMB angular power spectrum [53, 54].

The Einstein's theory of general relativity is an essential tool for studying the cosmos. It is one of the most beautiful creations of the human mind. In chapter 1, we begin with the mathematical machinery required for studying cosmology. The Einstein's equation, which relates the geometry of the Universe to its matter-energy contents, is discussed in section 1.1. Then, the simplest model of the Universe, the Friedmann model, is discussed in section 1.2. Models for the accelerated expansion of the Universe, $\Lambda CDM$, and dark energy models, are discussed in section 1.3. In section 1.4, we explain the distances in cosmology. Linear perturbation theory to study the structure is explained in section 1.5. The observational data sets used to obtain constraints on cosmological parameters are described in section 1.6.

## 1.1 General Relativity and Cosmology

According to Einstein's theory of general relativity, gravity is a manifestation of geometry or curvature of space-time. The geometry of space-time is imprinted in metric element

$$ds^2 = g_{\mu\nu}\, dx^\mu\, dx^\nu; \quad \mu,\ \nu = 0, 1, 2, 3, \tag{1.1}$$

where, $g_{\mu\nu}$ is the 'metric tensor'. The metric tensor contains all geometrical properties of space-time. Einstein's theory of general relativity provides us necessary mathematical machinery to study our Universe. The theory of general relativity relates the geometrical property of space-time to the matter-energy contents of the Universe, namely energy-momentum tensor $T_{\mu\nu}$. These two parts are related to each other via the Einstein field equation, given by

$$G_{\mu\nu} \equiv R_{\mu\nu} - \frac{1}{2} g_{\mu\nu} R = \frac{8\pi G}{c^4} T_{\mu\nu}, \tag{1.2}$$

where constants $G$ and $c$ are the universal gravitational constant and the speed of light in vacuum respectively. $G_{\mu\nu}$ is known as the Einstein tensor. $R_{\mu\nu}$ and $R$ are the Ricci curvature tensor and the Ricci scalar. Quantities $R_{\mu\nu}$ are, defined by

$$R_{\mu\nu} = \frac{\partial \Gamma^\lambda_{\mu\nu}}{\partial x^\lambda} - \frac{\partial \Gamma^\lambda_{\mu\lambda}}{\partial x^\nu} + \Gamma^\lambda_{\mu\nu}\Gamma^\delta_{\lambda\delta} - \Gamma^\delta_{\mu\lambda}\Gamma^\lambda_{\nu\delta}, \tag{1.3}$$

where $\Gamma^{\lambda}_{\mu\nu}$ are the Christoffel symbols and can by calculated from the metric tensors via the relation

$$\Gamma^{\lambda}_{\mu\nu} = \frac{1}{2} g^{\lambda\tau} \left( g_{\tau\mu,\nu} + g_{\tau\nu,\mu} - g_{\mu\nu,\tau} \right). \tag{1.4}$$

The Ricci scalar $R$ can be calculated by contracting the Ricci tensor

$$R = g^{\mu\nu} R_{\mu\nu}. \tag{1.5}$$

The general solution of equation (1.2) is not possible. To get a solution, we first need to specify the source term, the energy-momentum tensor $T_{\mu\nu}$.

### 1.1.1 The Energy-Momentum Tensor

The energy-momentum tensor $T_{\mu\nu}$ is a second rank symmetric tensor which comprises of everything that can curve the space-time or gravitate. It describes the flux of $\mu$ component of 4-momentum across the constant $x^{\nu}$ surface. Since it is a symmetric tensor, it has only ten independent components [55, 56, 57].

- $T^{00} = T^{tt}$ represents energy density.
- $T^{0i}$ (i=1,2,3) represents the flow of energy across the $x^i$ surface.
- $T^{i0}$ represents the i-component of momentum density.
- $T^{ij}$, for $i \neq j$, represents the shear stress.
- $T^{ii}$ represents the normal stress or pressure.

The energy-momentum tensor is symmetric tensor, i.e. $T_{\mu\nu} = T_{\nu\mu}$, so it has only ten independent components [55, 56, 57]. Now we describe some well-known energy-momentum tensors, commonly used in cosmology.

1. **Dust-** Identical, massive, non-interacting, electrically neutral particles constitute dust. The energy-momentum tensor for dust is given by

$$T^{\mu\nu} = \rho u^{\mu} u^{\nu}. \tag{1.6}$$

   In the rest frame of dust $u^{\mu} = (1, 0, 0, 0)$, therefore the only non-vanishing component of the energy-momentum tensor is $T^{00} = \rho$.

2. **Perfect Fluid-** Fluid which has no heat conduction or viscosity, consists of a collection of particles with small (non-relativistic) random motions has energy-momentum tensor

$$T^{\mu\nu} = (\rho + p)u^{\mu}u^{\nu} \pm pg^{\mu\nu}, \tag{1.7}$$

where $\rho$ and $p$ are the density and pressure of the fluid. Here, in '$\pm$' and at other places in this thesis, top and bottom signs correspond to $(-,+,+,+)$ and $(+,-,-,-)$ signatures of the metric element respectively.

3. **Scalar Field-** For a scalar field $\phi$, the energy-momentum tensor can be derived from its Lagrangian $L_{\phi}$ using equation

$$T^{\mu\nu}_{(\phi)} = \frac{2}{\sqrt{-g}} \frac{\delta\ (\sqrt{-g}L_{\phi})}{\delta\ g_{\mu\nu}.} \tag{1.8}$$

For a canonical scalar field, which is describe by a Lagrangian $L_{\phi} = \mp\frac{1}{2}g^{\mu\nu}\partial_{\mu}\phi\,\partial_{\nu}\phi - V(\phi)$, the energy-momentum tensor is given by

$$T^{\mu\nu}_{(\phi)} = \partial^{\mu}\phi\,\partial^{\nu}\phi \pm L_{\phi}g^{\mu\nu}, \tag{1.9}$$

We describe a canonical scalar field as dark energy in section 1.3.4. The energy-momentum tensor for a tachyon field, which has a Lagrangian $L = -V(\phi)\sqrt{1 \pm g^{\mu\nu}\partial_{\nu}\phi\,\partial_{\mu}\phi}$, can be derived from

$$T^{\mu\nu}_{(\phi)} = \frac{V(\phi)\partial^{\mu}\phi\,\partial^{\nu}\phi}{\sqrt{1 \pm g^{\alpha\beta}\partial_{\alpha}\phi\,\partial_{\beta}\phi}} \pm L_{\phi}g^{\mu\nu}. \tag{1.10}$$

Here, $V(\phi)$ is an arbitrary potential. We discus the tachyon field in sections 1.3.5.

From equation (1.2), we can deduce that $G^{\mu\nu}_{;\mu} = 0$ (the Bianchi identity). In other words, the Einstein tensor has zero divergence. This leads us to the conservation of the energy-momentum tensor

$$T^{\mu\nu}_{;\mu} = 0, \tag{1.11}$$

or

$$T^{\mu}_{\nu;\mu} \equiv \frac{\partial T^{\mu}_{\nu}}{\partial x^{\mu}} + \Gamma^{\mu}_{\alpha\mu}T^{\alpha}_{\nu} - \Gamma^{\alpha}_{\nu\mu}T^{\mu}_{\alpha} = 0. \tag{1.12}$$

With all the tools of general relativity described above, we can study the dynamics of the Universe. To do so, we need to specify the line element (or metric ) which represent the geometrical part and the form of energy-momentum tensor or species of contents of the Universe.

## 1.2 Friedmann Universe

The simplest model of the Universe is one in which the geometrical properties of space-time are independent of a spatial location and of direction. Such a universe will be spatially homogeneous and isotropic. This assumption is called the 'cosmological principle'. To hold the cosmological principle in the Universe, Einstein's equations demand homogeneity and isotropy in the matter field. We certainly see the structures like galaxies and clusters etc. in it. As we go to larger and larger scales, the Universe become more and more homogeneous. Therefore, we assume that at larger scales ($> 100Mpc$) these inhomogeneities can be ignored, and the matter distribution is described by a smoothed out average density. The geometrical properties of homogeneity and isotropy in the space-time are evident in the metric, given by

$$ds^2 = -c^2dt^2 + a^2(t)\left[\frac{dr^2}{1-Kr^2} + r^2\left(d\theta^2 + sin^2\theta d\phi^2\right)\right], \tag{1.13}$$

where $a(t)$ is scale factor of universe. This metric is called the 'Friedmann-Lemaitre-Robertson-Walker (FLRW)' metric. This coordinate system is called the 'comoving coordinate system', and world lines with $x^\alpha =$ constant are geodesics. Observer following these world lines is called a fundamental (or comoving) observer. Constant '$K$' specifies the geometry of 3-space (the spatial hypersurface); $K = +1,\ 0,\ -1$ corresponds to close, flat and open geometry, respectively.

### 1.2.1 Kinematics

Let the comoving separation between two observers, located at two different special locations in the Universe, is $\delta x$. Then the proper separation between them is given by

$$\delta l = a(t)\delta x. \tag{1.14}$$

In the expanding Universe, each of these observer sees other to moving with velocity

$$\delta v = \frac{d\delta l}{dt} = \dot{a}\delta x = \left(\frac{\dot{a}}{a}\right)\delta l. \tag{1.15}$$

Now, let's assume an electromagnetic signal of frequency $\omega$ is sent by one observer. Since, these observers are receding with each other with velocity $\delta v$, the other observer will receive a Doppler shifted electromagnetic wave with frequency $\omega + \delta\omega$,

where

$$\frac{\delta\omega}{\omega} = -\frac{\delta v}{c} = -\delta v = -\frac{\dot{a}}{a}\delta l = -\frac{\dot{a}}{a}\delta t = -\frac{\delta a}{a}. \tag{1.16}$$

Integrating above equation we get

$$\omega(t)a(t) = \text{constant}. \tag{1.17}$$

Thus in the expanding Universe, the frequency of electromagnetic waves is proportional to inverse of scale of expansion, that is $\omega \propto a^{-1}$. If a radiation is emitted from a location at $t_e$ with wavelength $\lambda_e$ and received at $t_0$ with wavelength $\lambda_0$ at another location, then $\lambda_0 > \lambda_e$ if $a(t_0) > a(t_e)$. In such an expanding universe we can associate a redshift $z$ with time $t$ by the relation

$$1 + z \equiv \frac{\lambda_0}{\lambda} = \frac{a(t_0)}{a(t)} = \frac{a_0}{a}. \tag{1.18}$$

Thus, the variables $t$, $a$ and $z$ are interchangeable. Here, $z = 0$ corresponds to present epoch, and without loss of generality we can set $a_0 = 1$. Further details on kinematics of the Friedmann Universe can be found in [55, 58].

### 1.2.2 Hubble's Law

Hubble and Slipher, individually, observed redshift in the spectrum of distant galaxies, although Slipher did not know those were galaxies. This redshift can be expressed by equation (1.18). The physical distance of an object from another observer in the Universe is given by $\mathbf{r} = a\mathbf{x}$, where $\mathbf{x}$ is comoving distance. Then, taking derivative with respect to cosmic time $t$, we get

$$\dot{\mathbf{r}} = H\mathbf{r} + a\dot{\mathbf{x}}, \tag{1.19}$$

where $H = \dot{a}/a$ is known as 'Hubble parameter' and it is the expansion rate of the Universe. The first term on the right, $H\mathbf{r}$, describe the cosmic expansion or Hubble flow. Whereas, second term, $a\dot{\mathbf{x}}$, is called 'the peculiar velocity', caused by local gravitational field. Now, the speed of an object along the line of sight is given by

$$v \equiv \dot{\mathbf{r}} \cdot \mathbf{r}/r = Hr + \mathbf{v_p} \cdot \mathbf{r}/r, \tag{1.20}$$

where $r \equiv |\mathbf{r}|$ and $\mathbf{v_p} = a\mathbf{x}$. In general, the peculiar velocity is much smaller than the Hubble expansion rate, so we can write

$$v \simeq H_0 r. \tag{1.21}$$

Here, $H_0$ is the present day value of the Hubble parameter $H(z)$ and known as the 'Hubble constant.' This equation holds for $z \ll 1$ and is known as the 'Hubble law' [59]. Edwin Hubble observed twenty five galaxies and found their distances, and also their velocities by calculating redshift in their spectrum. In 1929, he published his article [59], and first time showed that the Universe is expanding. Hubble derived the value of the Hubble constant $H_0 \sim 500\ km\ s^{-1}Mpc^{-1}$, which, due to large uncertainty in his data, is much larger than the current estimate. Planck-2018 collaboration provides $H_0 = 67.4 \pm 0.04\ km\ s^{-1}Mpc^{-1}$ [60].

### 1.2.3 Friedmann Equations and their Solutions

In a homogeneous and isotropic universe, described by the FLRW metric (1.13), the source term ($T_{\mu\nu}$) is restricted to perfect fluid given by equation (1.7). For such a universe, (00) and (ii) components of the Einstein equations (1.2) can be obtained as

$$\frac{\dot{a}^2 + K}{a^2} = \frac{8\pi G}{3}\rho, \tag{1.22}$$

$$\frac{2\ddot{a}}{a} + \frac{\dot{a}^2 + K}{a^2} = -8\pi G\ \rho. \tag{1.23}$$

Once the equation of state $p = p(\rho)$ is defined, these two equations completely determined the quantity $a(t)$, $\rho(t)$ and $p(t)$. These are known as the 'Friedmann equations.' Eliminating $K$ from equation (1.23) and using equation (1.22) we get the acceleration equation of the Universe, given by

$$\frac{\ddot{a}}{a} = -\frac{4\pi G}{3}(\rho + 3p). \tag{1.24}$$

Clearly, if $(\rho + 3p) > 0$ or $(1 + 3p/\rho) > 0$ then $\ddot{a} < 0$ and the expansion of universe will be decelerating, otherwise it will be accelerating. Since, the energy density $\rho$ remains always positive, the equation of state defined as

$$w = \frac{p}{\rho}, \tag{1.25}$$

decide the fate of the Universe, whether it will accelerating or decelerating depending on $w < -1/3$ or $w > -1/3$ respectively.

From equation (1.22) we get $\rho a^3 = (3/8\pi G)a\left(\dot{a}^2 + K\right)$. Differentiating it with respect to cosmic time and using equation (1.23) we end up with relation

$$\frac{d}{da}(\rho a^3) = -3a^2 p. \tag{1.26}$$

This equation is called the conservation or continuity equation. We can also derive this equation by solving conservation equation of energy-momentum tensor, i.e. $T^{\mu}_{\nu;\mu} = 0$, for the FLRW background.

The continuity equation (1.26) suggests that, if the equation of state parameter $w$ is a constant, we get a solution of the Friedmann equations, given by

$$\rho \propto a^{-3(1+w)}. \tag{1.27}$$

For non-relativistic matter $w = 0$ (because its pressure is negligible), so $\rho_{nr} \propto a^{-3}$. The equation of state of relativistic matter (or radiation) is $w = 1/3$, so $\rho_r \propto a^{-4}$. If $p = -\rho$ (corresponding to vacuum), then $w = -1$ and $\rho =$ constant or independent of $a$.

The curvature term in equation (1.22) can be expressed as

$$\frac{K}{a^2} = \frac{\dot{a}^2}{a^2}\left[\frac{\rho}{\rho_{cr}} - 1\right], \tag{1.28}$$

where $\rho_{cr} = 3H^3/8\pi G$ is known as 'the critical density'. Equation (1.28) motivate to define a 'density parameter' given by

$$\Omega(t) = \frac{\rho}{\rho_{cr}}, \tag{1.29}$$

and curvature term can be express in terms of matter content of a universe as

$$\frac{K}{a^2} = \frac{\dot{a}^2}{a^2}\left[\Omega - 1\right]. \tag{1.30}$$

Clearly the closed, flat and open geometry of the Universe, corresponding to $K = +1,\ 0,\ -1$, can be expressed by $\Omega > 1$, $\Omega = 1$, and $\Omega < 1$ respectively. Hence in terms of the density parameter the Friedmann equation (1.22) can be written as

$$\frac{\dot{a}^2 + K}{a^2} = \frac{8\pi G}{3}\rho = H^2\Omega(t). \tag{1.31}$$

Here, the energy density $\rho$ (and $\Omega$) are sum of energy densities of all the matter species in the Universe, i.e., $\rho = \sum \rho_i$ and $\Omega = \sum \Omega_i$. For late time cosmology, it is

sufficient to consider only the relativistic matter, the non-relativistic matter, and a negative pressure medium. Then the equation (1.31) takes the form

$$\frac{\dot{a}^2 + K}{a^2} = H_0^2 \left[ \Omega_{r0} a^{-4} + \Omega_{m0} a^{-3} + \Omega_{\Lambda 0} \right], \tag{1.32}$$

Here, and everywhere else in this thesis, the subscript '0' represents the present time ($t = t_{present}$ or $z = 0$). The symbols $\Omega_{r0}$, $\Omega_{m0}$, and $\Omega_{\Lambda 0}$ denote the present day values of corresponding quantities. These are defined as

$$\Omega_{r0} = \frac{8\pi G}{3H_0^2}\rho_{r0}\,, \quad \Omega_{m0} = \frac{8\pi G}{3H_0^2}\rho_{m0}\,, \quad \text{and} \quad \Omega_{\Lambda 0} = \frac{8\pi G}{3H_0^2}\rho_{\Lambda}. \tag{1.33}$$

If we defined a density parameter for curvature term as $\Omega_{K0} = -K/H_0^2$, we can add it on the right hand side of the equation (1.32), given as

$$\frac{\dot{a}^2}{a^2} \equiv H^2 = H_0^2 \left[ \frac{\Omega_{r0}}{a^4} + \frac{\Omega_{m0}}{a^3} + \frac{\Omega_{K0}}{a^2} + \Omega_{\Lambda 0} \right], \tag{1.34}$$

The Cosmic Microwave Background observations have constrained the spatial curvature to be very near to zero, i.e., the Universe is spatially flat. The WMAP 5 year data provide constraint on curvature as $-0.0175 < \Omega_{K0} < 0.0085$ at the $2\sigma$ confidence level [61]. Hence, for further analysis in this thesis, we assume a flat universe considering $\Omega_{K0} = 0$. From equation (1.30), we can see that this requires the sum of all density parameters to be unity, i.e. $\Omega \equiv \Omega_r + \Omega_m + \Omega_\Lambda = 1$. From equation (1.34), it is clear that during the evolution of the Universe, each species dominate the energy budget at a different epoch. In radiation and matter dominated era, since the equation of state parameter is $w = 1/3$ and 0 respectively, hence $\ddot{a} < 0$, and the Universe went through a decelerating phase. Only if the energy budget is dominated by a negative pressure medium with an equation of state $w < -1/3$, the Universe can go to an accelerating phase.

## 1.3 Accelerated Expansion of the Universe

Observations have confirmed that the Universe underwent a transition from decelerating to accelerating expansion in recent past [62] and accelerating since then [4, 5, 63]. The simplest model considers vacuum energy density, with an equation of state $w = -1$, as the reason for this transition and accelerated expansion. We shed some light on this model (known as $\Lambda CDM$ model), how it agrees with observations, and theoretical problems it suffers from.

### 1.3.1 $\Lambda CDM$ Model

The acceleration in the expansion rate of the Universe can be explained by adding a constant $\Lambda$, known as 'the cosmological constant', in the Einstein field equations. It was originally introduced by Einstein in 1917 to get solution for a static universe, but after the discovery of the expanding Universe by Hubble, it was dropped. Addition of constant $\Lambda$ in the source part of Einstein field equations, alter the Friedmann equations in the form, given by

$$\frac{\dot{a}^2 + K}{a^2} = \frac{8\pi G}{3}\rho + \frac{\Lambda}{3}, \tag{1.35}$$

$$\frac{\ddot{a}}{a} = -\frac{4\pi G}{3}(\rho + 3p) + \frac{\Lambda}{3}. \tag{1.36}$$

The physical explanation of the cosmological constant is given by introducing vacuum energy density (which is constant). The energy density and the density parameter of vacuum, in terms of cosmological constant, take the form [64, 65]

$$\rho_\Lambda = \frac{\Lambda}{8\pi G}, \quad \text{and} \quad \Omega_\Lambda = \frac{\Lambda}{3H^2}. \tag{1.37}$$

The pressure density of vacuum is given by $p_\Lambda = -\rho_\Lambda = -\Lambda/8\pi G$. Hence, the equation of state of this component $w = p_\Lambda/\rho_\Lambda = -1$, and it remains constant during the evolution of the Universe. With these definitions, we can write the Friedmann equation as

$$\frac{\dot{a}^2}{a^2} \equiv H^2 = H_0^2\left[\frac{\Omega_{r0}}{a^4} + \frac{\Omega_{m0}}{a^3} + \Omega_{\Lambda 0}\right], \tag{1.38}$$

here, we have considered the geometry of a universe flat, i.e. $\Omega_K = 0$. The non-relativistic component is sum of pressure-less baryonic matter and dark matter, i.e., $\Omega_{m0} = \Omega_{b0} + \Omega_{dm0}$.

In the top left panel of figure 1.3, we show the phases of the evolution for this model. We can see that after decelerating phases of radiation and matter domination, the Universe goes through a transition in recent past and start accelerating. In the right panel of the same figure, we show the evolution of the density parameters of all three components. The $\Lambda CDM$ model is consistent with most of the current cosmological observations [4, 5, 60, 63, 66]. For example, in the second row of figure 1.3, we show comparison $\Lambda CDM$ model with SN-Ia union 2.1 and H(z) data. Although, This model is simple and the most favoured one, it runs into problems at theoretical front.

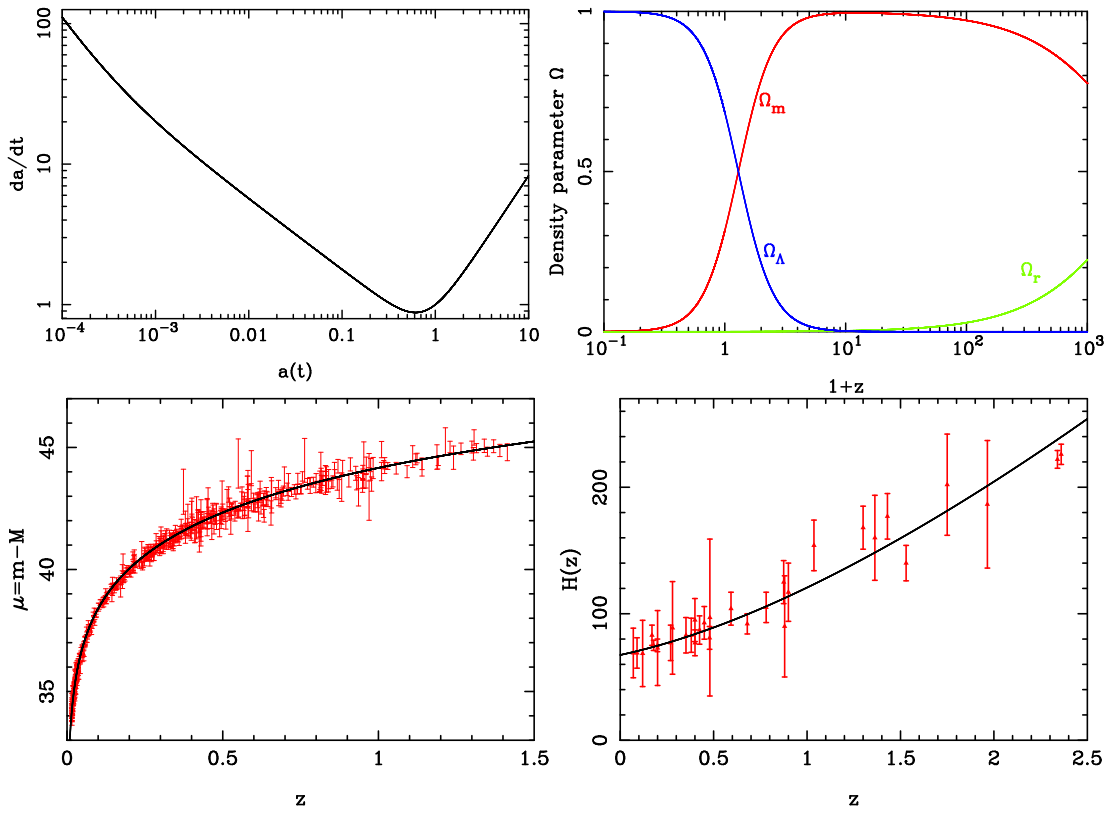


Figure 1.3: In the top left panel, we show the phases of evolution of the Universe for the $\Lambda CDM$ model. The evolution of the density parameters of matter (in red), vacuum (in blue), and radiation (in orange) are shown in top right panel. In these plots, we set the parameter $\Omega_{m0} = 0.315$ and $H_0 = 67.4\ km\ s^{-1} Mpc^{-1}$ (Planck-2018 best fit values). In the bottom left and right panels, we show comparison of this model with SN-Ia union 2.1 data and direct measurements of Hubble parameter H(z).

### 1.3.2 Fine Tuning Problem in the Cosmological Constant Model

Despite the success of the $\Lambda CDM$ model, it suffers from some theoretical issues. One of these issues is the discrepancy between theoretical and observational values of the cosmological constant. In $\Lambda CDM$ model, the cosmological constant is equivalent to a zero point vacuum energy density, $\rho_{vac} = \Lambda/8\pi G$. The value of the vacuum energy density calculated from zero point vacuum fluctuation in field theory is $\rho_{vac}^{theory} \sim 2 \times 10^{110} erg\ cm^{-3}$, whereas the value obtained by observations in cosmology is $\rho_{vac}^{obs} \sim 2 \times 10^{-10} erg\ cm^{-3}$, for details refer to [67]. We can see that there is a discrepancy of 120 order of magnitude between these values. This problem is known as 'the cosmological constant problem.'

The relative scaling $\rho_\Lambda/\rho_m \propto a^3$ implies that the cosmological constant was negligible in the past (in the matter-dominated era), and will dominate in future. If the cosmological constant is set as an initial condition at very early in the matter-

dominated era, it has to be set or tuned precisely. A couple of orders higher value can result in lack of large-scale-structure today, and a couple of orders smaller value results in cosmological constant to be undetectable. There is no explanation as to why the energy density of the cosmological constant has the same order of magnitude as that of the matter density at present. This problem is known as the 'coincidence problem'. Current observational data, however, does not rule out the value of the equation of state parameter $w \neq -1$ and dynamical nature of energy density replacing the vacuum density. These facts motivate the study of alternate sources for accelerated expansion, namely dark energy.

### 1.3.3 Barotropic Fluid Models of Dark Energy

The simplest alternative to the cosmological model are those for which the dynamical nature of the equation of state parameter is assumed by considering a functional form or parametrization of $w$. Here, the equation of state is either a constant (with $w \neq -1$) or a function of redshift or scale factor. In these models, the two important parameters are the present value of the equation of state parameter, $w_0$, and it's derivative, $w'(z=0)$. Following parameterizations are among the most popular and widely used

- The Chevallier-Polarski-Linder (CPL) parameterization [68, 69] in which

$$w(a) = w_0 + w'(a=1)(1-a), \tag{1.39}$$

  or

$$w(z) = w_0 + w'(z=0)\frac{z}{1+z}. \tag{1.40}$$

- The Jassal-Bagla-Padmanabhan parameterization [70] in which

$$w(z) = w_0 + w'(z=0)\frac{z}{(1+z)^2}. \tag{1.41}$$

- The logarithmic parameterization [71] in which

$$w(z) = w_0 + w'(z=0)log(1+z). \tag{1.42}$$

All these models agree with each other at low redshifts, but as we see in the figure 1.4, at higher redshift their behavior starts deviating from each other. Although, the equation of state parameter is a well-behaved function for all these parameterizations at high redshifts and present, it diverges in far future. The most general

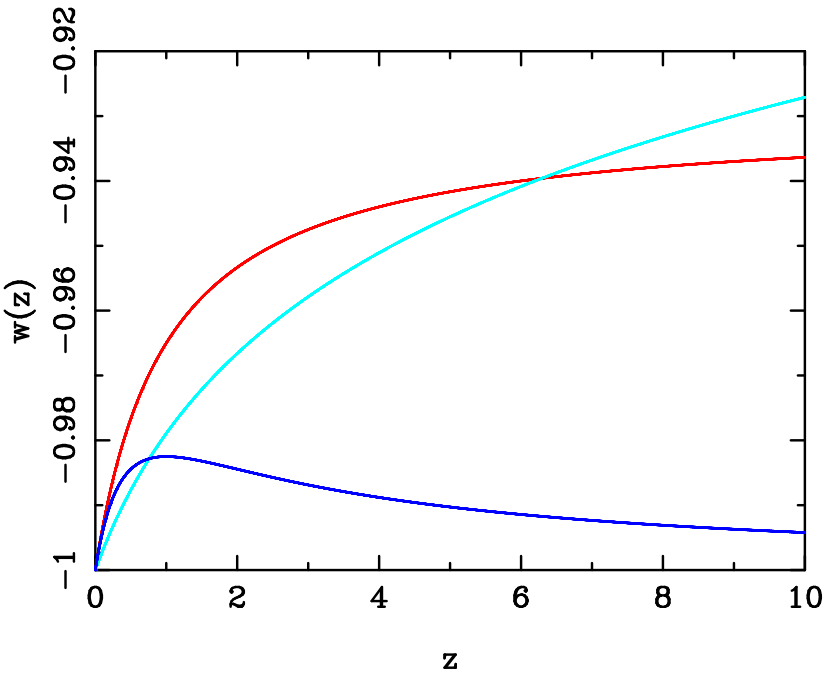


Figure 1.4: Evolution of equation of state with redshift for parametrized models of dark energy. Read, blue and sky-blue colours represent the CPL model, the JBP model and the logarithmic model respectively. For the purpose of this plot, we have set $w_0 = -1.0$ and $w'(z=0) = 0.05$.

parameterization of $w$ is the 'Pade parameterization', which does not diverge at small and high redshifts. The Pade approximation [72, 73] of oder $(m,\ n)$ of a function $f(x)$ is given by

$$f(x) = \frac{a_0 + a_1 x + a_2 x^2 + ... + a_m x^m}{b_0 + b_1 x + b_2 x^2 + ... + b_n x^n}. \tag{1.43}$$

The Pade parameterizations have been found consistent with the current expansion data [16, 74]. Some examples of Pade parameterizations are as follows [16, 73]

- Expansion of $w(a)$ with respect to (1-a) up to oder $(1,\ 1)$, given by

$$w(a) = \frac{w_0 + w_1(1-a)}{1 + w_2(1-a)}. \tag{1.44}$$

  Clearly, if $w_2 = 0$ this parameterization reduces to CPL model.

- Parameterization of $w(a)$ as a function of $ln\ a$ up to oder $(1,\ 1)$, given by

$$w(a) = \frac{w_0 + w_1 ln\ a}{1 + w_2 ln\ a}. \tag{1.45}$$

In oder to avoid singularity in parameterization 1.44, we need to impose condition $w_2 \neq 0$ and $-1$, where as in parametrization 1.45 $w_2 \neq 0$. Then, these Pade parameterizations are well-behaved functions in the range $0 \leq a \leq \infty$. More detailed

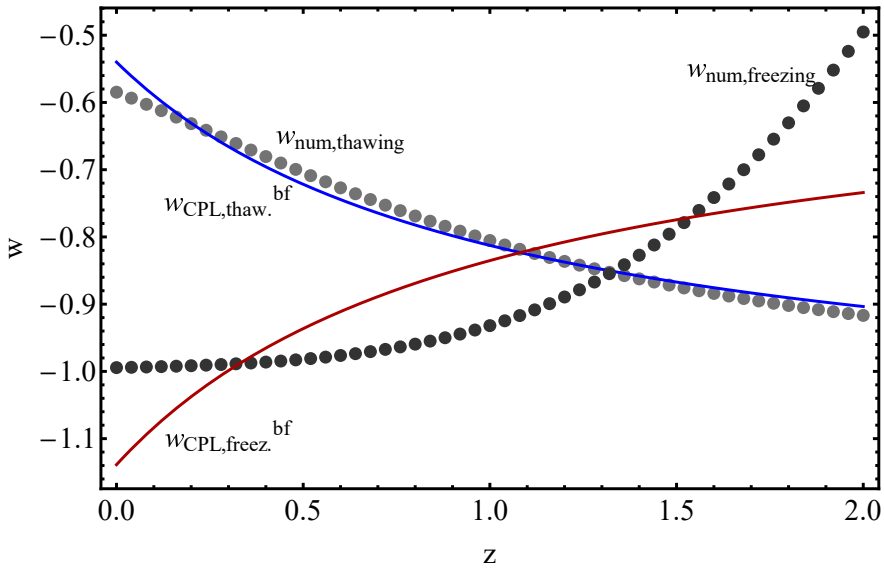


Figure 1.5: A comparison between thawing and freezing quintessence models (dotted curves). Solid lines represent best fit CPL parameterizations. Clearly, CPL parameterization fits thawing model better than freezing model. Image credit - Pantazis et. al. (2016) [77]. License agreement to reuse this figure is in appendix A.

discussion on Pade parameterizations, constraints on parameters and cosmological evolution under these models can be found in [16, 73, 74]. There are many other parametrized models described in [10, 11, 12, 75, 76].

### 1.3.4 Canonical Scalar Field Model of dark Energy

Canonical scalar field, also known as the quintessence field, is a well studied dark energy model. In scalar field models, the present day accelerated expansion of the Universe is achieved by a slow rolling field. The quintessence field is described by a canonical Lagrangian

$$L = \mp\frac{1}{2}g^{\mu\nu}\partial_\mu\phi\,\partial_\nu\phi - V(\phi), \tag{1.46}$$

where $V(\phi)$ is an arbitrary potential. The dynamics of a homogeneous quintessence field are governed by the equation

$$\ddot{\phi} + 3H\dot{\phi} + \frac{dV(\phi)}{d\phi} = 0. \tag{1.47}$$

To study the evolution of the Universe, we need to solve the Friedmann equation along with equation (1.47). The energy density and pressure of a quintessence field is given by

$$\rho_\phi = \frac{1}{2}\dot{\phi}^2 + V(\phi), \quad \text{and} \quad P_\phi = \frac{1}{2}\dot{\phi}^2 - V(\phi). \tag{1.48}$$

The equation of state parameter for quintessence model is given by

$$w_\phi = \frac{P_\phi}{\rho_\phi} = \frac{\dot{\phi}^2 - 2V(\phi)}{\dot{\phi}^2 + 2V(\phi)}. \tag{1.49}$$

Clearly, the functional form of the equation of state parameter depends on whether the kinetic term dominates, or the potential term is the dominating one. For a slowly evolving scalar field, $\dot{\phi}^2/2V(\phi) << 1$ then we get $w_\phi \approx -1$. In this case, the scalar field behaves like a slowly varying vacuum energy with $\rho_{vac}(t) \simeq V(\phi(t))$. In general, $w_\phi$ can take any value between -1 to +1, depending on whether the scalar field is slowly varying or evolving rapidly respectively.

Based on the evolution of the equation of state parameter the quintessences models are broadly classified into 'thawing' and 'freezing' models [19, 20, 78]. In the first class of models, value of the equation of state parameter at early time remain frozen at its initial value ( $w \simeq -1$) due to large Hubble damping. Only in the near past the Hubble damping decreases and the potential starts rolling to its minimum, the equation of state starts to evolve from a cosmological constant like value [25, 77, 79]. In the freezing models, at early time due to steep potential the kinetic term rolls down towards its minimum and it is non-zero. At later time, the potential becomes shallower and the kinetic term negligible. Therefore, the equation of state parameter asymptotically freezes to a value $w = -1$. Depending on the details of the dynamics, the freezing models are also sub-classified into 'tracking' and 'scaling' models [77, 80, 81, 82]. In figure 1.5, we can see the comparison between thawing and freezing quintessence models with their best fit CPL parameterizations. Because of concave nature of CPL and other parameterizations mentioned in section 1.3.3, when increasing, they fit thawing model better than the freezing model [77]. Nevertheless, quintessence models do not have the fine-tuning problem that $\Lambda CDM$ model suffers from; they have tuning problem of their own. To achieve present-day accelerated expansion they require an ad-hoc potential. The detailed study on quintessence model can be find in [18, 19, 20, 21, 22, 23, 24, 25, 80].

### 1.3.5 Non-Canonical Scalar Field - Tachyon Scalar Field Model

Tachyon scalar field is a non-canonical scalar field which arises naturally in string theory as a decay mode of D-branes [34, 35, 36]. The tachyon scalar field is described by the Lagrangian

$$L = -V(\phi)\sqrt{1 \pm g^{\mu\nu}\partial_\mu\phi\,\partial_\nu\phi}, \tag{1.50}$$

where $V(\phi)$ is an arbitrary potential. The energy density and pressure of tachyon field are

$$\rho_\phi = \frac{V(\phi)}{\sqrt{1-\dot{\phi}^2}}\,, \qquad P_\phi = -V(\phi)\sqrt{1-\dot{\phi}^2}. \tag{1.51}$$

Therefore, the equation of state parameter of the tachyon field is $w_\phi = P_\phi/\rho_\phi = \dot{\phi}^2 - 1$. The dynamics of the scalar field is governed by the equation of motion for the scalar field

$$\ddot{\phi} = -(1-\dot{\phi}^2)\left[3H\dot{\phi} + \frac{1}{V(\phi)}\frac{dV}{d\phi}\right]. \tag{1.52}$$

As $\dot{\phi}$ approaches $\pm 1$, the equation of state becomes dust like, and the quantity $\ddot{\phi}$ goes to zero. Therefore, the equation of state remains dust like for a long time. The cosmological evolution in this model too depends on the choice of potential. We consider two runaway potentials which have been employed to study tachyon dynamics. The runaway potentials naturally arise in string theory and M-theory, and they are capable of generating the late time accelerated expansion of the Universe [83, 84, 85, 86]. The background cosmology in the presence of two different tachyon scalar field potentials is summarized in section 2.1.1 and 2.1.2. We discuss tachyon scalar field as smooth homogeneous dark energy, its dynamics and constraints on parameters, in chapter 2. The effect of perturbations in tachyon dark energy on clustering of matter and its growth rate are discussed in chapter 3.

## 1.4 Distances in Cosmology

Most of the observations used to constrain the cosmological parameters are based on measurements of distances. Actually, cosmological history is hidden in the relation between distance and redshift. But in cosmology, we can not measure distances directly, they are measured through changes in some physical quantities, like luminosity and the angular diameter of some object in the Universe. The electromagnetic signal (light) gets redshifted while traveling along the path between the source and the observer. The amount of redshift depends on the expansion rate of the Universe and its energy budget. Since these quantities are model dependent, the distances in cosmology also depend on the model we are considering [55, 56, 87].

Let a photon emitted at time $t = t_e$ from $r = r_e$ (redshift $z$) reaches the observer at time $t = t_0$ with $r = 0$ (and $z = 0$). This light travels along the null geodesic

$ds^2 = -c^2dt^2 + a^2(t)dr^2 = 0$. Therefore, distance $r$ is given by equation

$$r_c \equiv r = \int_0^r dr = \int_{t_e}^{t_0} \frac{c}{a} dt = \int_{a_e}^{a_0} \frac{c}{a\dot{a}} da. \tag{1.53}$$

This distance is known as 'comoving distance'. Using equation (1.18), we can write comoving distance as

$$r_c = \frac{c}{a_0 H_0} \int_0^z \frac{dz}{E(z)}, \tag{1.54}$$

here, $E(z) = H(z)/H_0$. Equation (1.54) provide an intuitive way of defining distance, but it is not directly measurable. The observable distances are the luminosity distance and the angular diameter distance described bellow.

### 1.4.1 Luminosity Distance

If we know the luminosity of an object, a 'standard candle', by observing its flux, we can calculate its distance. One such important standardized candle is the supernova type Ia. The luminosity distance of an object at redshift $z$ is defined by equation

$$D_L^2 = \frac{L_e}{4\pi\mathscr{F}}, \tag{1.55}$$

where $L_e$ is the absolute luminosity of the source and $\mathscr{F}$ is flux observed. Note that the luminosity observed at $z = 0$ is different from absolute luminosity $L_e$ because of expansion. The flux of an object at comoving distance $r_c$ is $\mathscr{F} = L_0/4\pi r_c^2$. Then the luminosity distance (1.55) reduce to

$$D_L^2 = r_c^2 \frac{L_e}{L_0}. \tag{1.56}$$

Now, if a source emit $\Delta E_e$ energy in time interval $\Delta t_e$, its absolute luminosity is $L_e = \Delta E_e/\Delta t_e$. Similarly, observer receive $\Delta E_0$ energy in time interval $\Delta t_0$, its observed luminosity is $L_0 = \Delta E_0/\Delta t_0$. Since the wavelength is inversely proportional to energy, we can find that $\Delta E_e/\Delta E_0 = \lambda_0/\lambda_e = 1 + z$. On the other hand, $\Delta t_0/\Delta t_e = \lambda_0/\lambda_e = 1 + z$. Hence, the ratio of luminosities is

$$\frac{L_e}{L_0} = \frac{\Delta E_e}{\Delta E_0} \frac{\Delta t_0}{\Delta t_e} = (1+z)^2. \tag{1.57}$$

Then, the luminosity distance is

$$D_L = (1+z)r_c = \frac{c}{H_0}(1+z)\int_0^z \frac{dz}{E(z)}. \tag{1.58}$$

This equation clearly show that the luminosity distance is directly related to the expansion rate of the Universe. In the top panel of figure 1.6, we can see the evolution of luminosity distance (in unit of $cH_0^{-1}$) with redshift. Here, we have considered a flat-$\Lambda CDM$ model with $\Omega_{r0} = 4.5 \times 10^{-5}$, and we have varied $\Omega_{m0}$. We can see that as we increase $\Omega_{m0}$, the luminosity distance decreases at a fixed redshift. For more general discussion on the luminosity distance refer to [55, 58, 88].

### 1.4.2 Angular Diameter Distance

If the object of actual or physical size $\Delta l$ orthogonal to the line of sight subtends an angle $\Delta\theta$ at the observer, then its distance given by

$$D_A = \frac{\Delta l}{\Delta\theta}. \tag{1.59}$$

This distance is known as the 'angular diameter distance'. If the angle, subtended by an object of known physical size called the 'standard ruler' in cosmology is measured, its distance can be calculated from the above equation. One such standard ruler is provided by 'the Baryon Acoustic Oscillations (BAO)', and it is described in section 1.6.3. If the comoving distance of the object is $r_c$, then its physical size is given by $\Delta l = a(t_e)r_c\Delta\theta$. Then the angular diameter distanced is reduce to

$$D_A = a(t_e)r_c = \frac{c}{H_0}\frac{1}{1+z}\int_0^z \frac{dz}{E(z)}. \tag{1.60}$$

Clearly, the relation between angular diameter and luminosity distance is

$$D_A = \frac{D_L}{(1+z)^2}. \tag{1.61}$$

This known as duality or reciprocity or Etherington relation.

In the bottom panel of figure 1.6, we can see the evolution of the angular diameter distance. We have considered the same model described in section 1.4.1 to generate this plot. Unlike luminosity distance, angular diameter distance does not evolve monotonically with redshift. Initially, it grows with redshift, takes a maximum then decreases as we increase the value of redshift. We can see that similar to

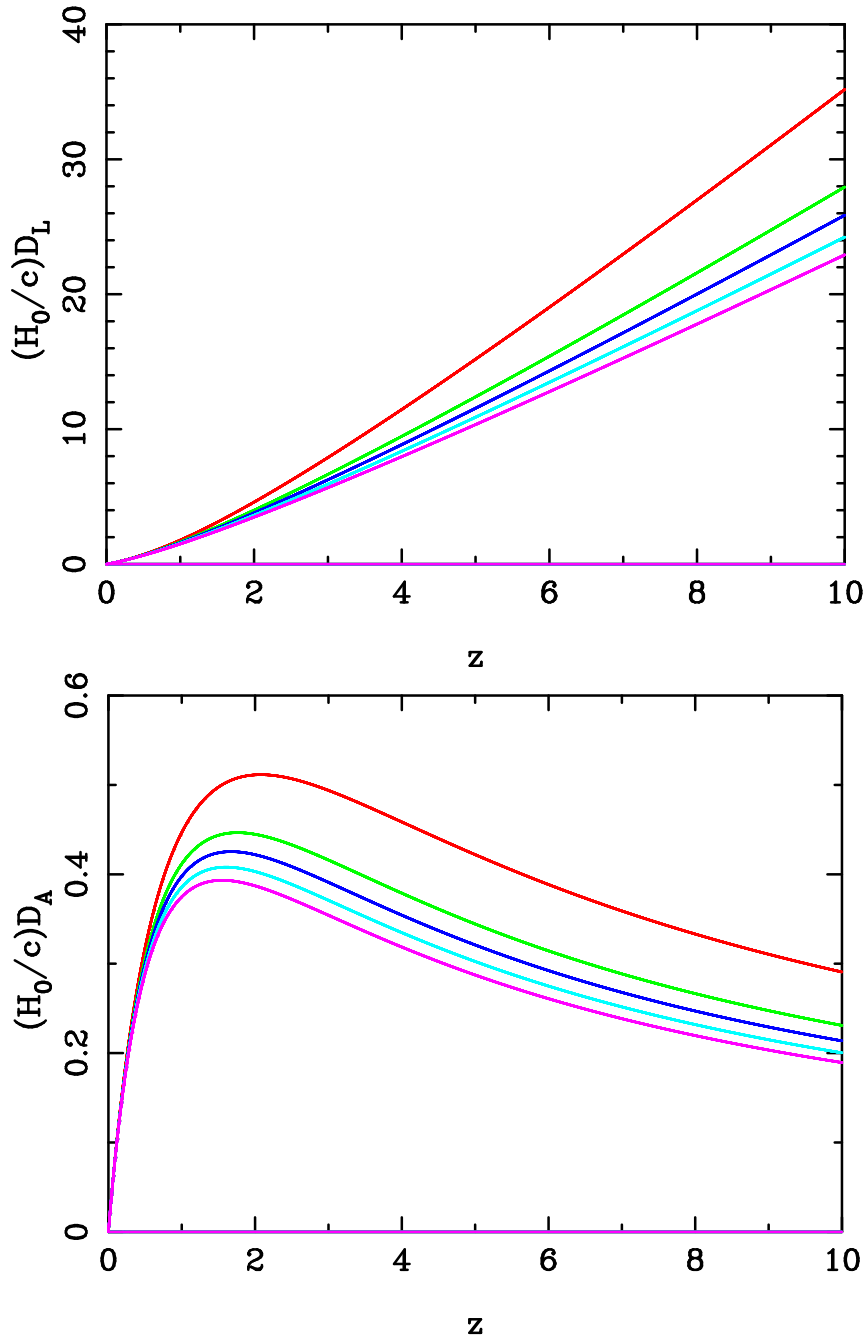


Figure 1.6: Evolution of luminosity and angular diameter distance and their dependence on $\Omega_{m0}$ for flat $\Lambda CDM$ model. Here, $D_L$ and $D_A$ are in the unit of $cH_0^{-1}$. Red, green, blue, light-blue and pink colours are for $\Omega_{m0} = 0.1,\ 0.2,\ 0.25,\ 0.3,$ and $0.35$ respectively.

luminosity distance, angular diameter distance also decreases as we increase $\Omega_{m0}$ at a fixed redshift. Further discussion on the Angular diameter distance can be found in [55, 58, 88]. so for we have described a homogeneous and isotropic universe. These assumptions are true at large scales. We can certainly see structures like galaxies, clusters, etc. In the next section, we present theory for the structure formation in the Universe.

## 1.5 Inhomogeneity in the Universe and Linear Perturbation Theory

The small but important anisotropy in cosmic microwave background radiation (CMB), indicates that our universe was already inhomogeneous at $z \sim 1000$. In the form relative temperature fluctuation it was $\Delta T/T \approx 10^{-5}$. This fact allows us to assume that for the structures we see today, seeds were planted in the past (during the inflationary era) in the form of small deviation from homogeneities in our universe. These small inhomogeneities, then grew due to gravitational instability with time and formed structures like galaxies and clusters, etc. The inhomogeneity can be quantified using 'relative density contrast', defined by equation

$$\delta(\mathbf{r},t) = \frac{\rho(\mathbf{r},t) - \bar{\rho}(t)}{\bar{\rho}(t)}, \tag{1.62}$$

where $\bar{\rho}(t)$ is average density of the Universe at time $t$. Clearly, $\delta \geq -1$, because $\rho \geq 0$. The $\delta > 0$ are overdense region and produce additional gravitational potential than the cosmic average, whereas region with $\delta < 0$ are underdense. In overdense region the expansion rate is slower than the average Hubble expansion due to the stronger gravitational field, and it also increases the clumping further. For under dense region, situation is just the opposite. In this thesis, we mainly concentrate on overdense region with $\delta > 0$. There are three possible cases, first when $\delta \ll 1$, then it is possible to linearize Einstein equations and get solutions which describe the growth of linear perturbations. On the other hand, if $\delta \approx 1$ or $\delta \gg 1$ then a solution is possible only with some specific assumptions, e.g. assumption of spherical symmetry, or by numerical computation. We focus only on linear case. We study matter perturbations as well as dark energy perturbations. This makes the equation fairly complicated, and it is only possible to solve them numerically.

### 1.5.1 Linear Perturbation Theory

The Poisson equation, which relates the matter density to the gravitational potential, is a linear equation. This fact enables us to consider the effect of homogeneous matter distribution and that of density fluctuations separately. Hence the total gravitational field can be considered as a sum of the gravitational field of homogeneous part and that of density fluctuations. To study structure formation, we consider perturbations in the metric $g_{\mu\nu}$ and the source $T_{\mu\nu}$ into the form $g_{\mu\nu} + \delta g_{\mu\nu}$ and $T_{\mu\nu} + \delta T_{\mu\nu}$. Here, ( $g_{\mu\nu}$ , $T_{\mu\nu}$ ) represents the background universe, and ( $\delta g_{\mu\nu}$ , $\delta T_{\mu\nu}$ ) represents the perturbation. Considering perturbations small, we solve linearized Einstein's equations and get a solution in the form

$$\hat{\mathrm{L}}(g_{\mu\nu})\delta g_{\mu\nu} = \delta T_{\mu\nu}, \tag{1.63}$$

where $\hat{\mathrm{L}}$ is a linear differential operator. It depends only on the background universe. Because of linearity of the equations, their solution can be expand in terms of some mode functions. For the flat universe ($\Omega = 1$) mode functions will be plane waves. By transforming variables in Fourier space we get a set of equations

$$\hat{\mathrm{L}}_{(k)}\delta g_{(k)} = \delta T_{(k)}, \tag{1.64}$$

for each mode. Here, $k$ represents the magnitude of wave vector $\mathbf{k}$. Solutions of equation (1.64) determine the evolution of each mode or 'k' separately.

### 1.5.2 Gauge Freedom in Cosmology

The field equations remain invariant under a general coordinate transformation. So we are free to use any frame of reference. We select those transformations that leave $g_{\mu\nu}$ invariant and only change $\delta g_{\mu\nu}$, because we want the background to remain FRLW like. These transformations are called 'gauge transformations'. Hence, going from one frame to other and by scaling coordinates, we can make small perturbations large and vice versa. These can even vanish in some frame. This ambiguity needs to be resolved before obtaining meaningful results. There is a simple solution to this problem. We choose to work in a fixed coordinate system and compute physical quantities. If this coordinate system is well motivated, all physical quantities will be well defined. Two widely used gauges are the synchronous gauge and the conformal Newtonian gauge (also known as the longitudinal gauge) [89]. Metric in

the synchronous gauge is defined by

$$ds^2 = a^2(\tau)\{-d\tau^2 + (\delta_{ij} + h_{ij})dx^i dx^j\}, \tag{1.65}$$

where $\tau$ is conformal time. The quantity $h_{ij}$ is the metric perturbation. More details about this gauge can be found in [55, 89]. The conformal Newtonian gauge is physically well motivated and better in dealing with the scalar degree of metric perturbations. In this gauge, the line element is given by

$$ds^2 = -(1+2\Psi)dt^2 + a^2(t)(1+2\Phi)\delta_{ij}dx^i dx^j, \tag{1.66}$$

where $t$ is cosmic time which has relation with conformal time as $dt = a(t)d\tau$. Here, $\Psi$ and $\Phi$ define the scalar degrees of freedom of metric perturbation. The tensor perturbations are eliminated here because the dynamical equations for these (which govern the evolution of gravitational waves) decouple from the rest [55].

For our purpose, it is sufficient to study only scalar degree of freedom. In equation (1.66), we can see that the metric in this gauge is diagonal. Another advantage of working in this gauge is that the metric perturbation $\Psi$ represents the gravitational potential in Newtonian limit, and hence has a simple physical interpretation. In the absence of anisotropic stress in the energy-momentum tension $T^{ij}$ we get $\Psi = -\Phi$, and we have only one scalar degree of freedom [55, 89]. In the next section we present the solution of perturbed Einstein equations for this gauge.

### 1.5.3 Solution of Perturbed Einstein Equations

In the absence of anisotropic stress, the Einstein equations in longitudinal gauge reduce to the following set of equations.

$$\nabla^2\Phi + 3a^2H\left(H\Psi - \dot{\Phi}\right) = 4\pi G a^2 \delta T^0_0, \tag{1.67}$$

$$a\nabla^2\left(\dot{\Phi} - H\Psi\right) = -\frac{4}{3}\pi G a^2 \delta T^i_{0,i}, \tag{1.68}$$

$$\Psi = -\Phi, \tag{1.69}$$

$$\ddot{\Phi} + 3H\dot{\Phi} - H\dot{\Psi} - \left(3H^2 + 2\dot{H}\right)\Psi = -\frac{4}{3}\pi G \delta T^i_i. \tag{1.70}$$

Here dot represents a derivative with respect to cosmological time $t$, and $\nabla$ represents spatial derivatives evaluated with the background metric. The equation (1.69) follows from $\delta T^i_j = 0$. In oder to solve above set of linear perturbation equations, first we need to specify perturbed energy-momentum tensor $\delta T^\mu_\nu$. We discuss a simple case of single perfect fluid as a source, for illustration.

**Solution for a single fluid:** Let us consider a single fluid model with the energy-momentum tensor $T^\mu_\nu$ defined equation (1.7). In oder to calculate the perturbed energy-momentum tensor $\delta T^\mu_\nu$, we need to find the perturbed part of the four-velocity $u^\mu = \frac{dx^\mu}{ds}$. To first oder in all perturbed quantities, using conformal gauge defined in equation (1.66), we obtain

$$u^\mu = \left[(1-\Psi)\ ,\quad \frac{v^i}{a}\right], \quad u_\mu = g_{\mu\nu}u^\nu, \quad u_\mu u^\mu = -1, \tag{1.71}$$

where $v^i = \frac{dx^i}{d\tau} = a\frac{dx^i}{dt}$ is the peculiar velocity of matter with respect to the Hubble expansion. Substituting equation (1.71) in equation (1.7), we get the perturbed part of the energy-momentum tensor

$$\delta T^0_0 = -\delta\rho, \quad \delta T^0_i = -\delta T^i_0 = (1+w)\bar{\rho}v^i, \quad \delta T^1_1 = \delta T^2_2 = \delta T^3_3 = \delta p. \tag{1.72}$$

Here $w = \bar{\rho}/\bar{p}$. The energy-momentum tensor satisfies the continuity equation $T^\mu_{\nu;\mu} = 0$. The first-oder perturbed counter part of this equation $\delta T^\mu_{\nu;\mu} = 0$ provides some useful equations. For $\nu = 0$, this equation reduces to

$$\delta\rho + 3aH(\delta\rho + \delta p) = -(\bar{\rho}+\bar{p})\left(\theta + 3a\dot{\Phi}\right), \tag{1.73}$$

where $\theta = \nabla_i v^i$ is the divergence of velocity. Using unperturbed continuity equation, $\dot{\bar{\rho}} + 3aH(\bar{\rho}+\bar{p}) = 0$, with equation (1.73), we get equation for the density contrast $\delta = \frac{\delta\rho}{\bar{\rho}}$, given by

$$\dot{\delta} + 3H\left(c_s^2 - w\right)\delta = -\frac{1}{a}(1+w)\left(\theta + 3a\dot{\Phi}\right), \tag{1.74}$$

called the 'perturbed continuity equation'. Equation for $\theta$, can be derived by solving equation $\delta T^\mu_{i;\mu} = 0$, and given by

$$\dot{\theta} + \left[H(1-3w) + \frac{\dot{w}}{1+w}\right]\theta = -\frac{1}{a}\nabla^2\left(\frac{c_s^2}{1+w}\delta + \Psi\right), \tag{1.75}$$

where the sound velocity $c_s^2 = \frac{\delta p}{\delta\rho}$.

Since all necessary equations are linear in all perturbed quantities, we use the Fourier technique to solve them. We define Fourier space counterpart of each quantity using relation

$$A(\vec{x},t)=\int d^3kA_k e^{i\vec{k}.\vec{x}}. \tag{1.76}$$

Here $A(\vec{x},t)$ stands for quantities $(\Phi,\Psi,\delta,\theta)$ in real space, whereas $A_k$ stands for their Fourier space or k-space counter parts. The symbol $k$ represents the wave number for each Fourier mode. It is related to physical length scale of perturbation $\lambda_p$ through relation $\lambda=2\pi a/k$. Using equations (1.67) - (1.70) , (1.74) and (1.75) we get the following set of equations for each Fourier mode

$$k^2\Phi+3a^2H\left(\dot{\Phi}-H\Psi\right)=4\pi Ga^2\bar{\rho}\delta, \tag{1.77}$$

$$ak^2\left(\dot{\Phi}-H\Psi\right)=-4\pi Ga^2(1+w)\bar{\rho}\theta, \tag{1.78}$$

$$\Psi=-\Phi \tag{1.79}$$

$$\ddot{\Phi}+3H\dot{\Phi}-H\dot{\Psi}-\left(3H^2+2\dot{H}\right)\Psi=-4\pi Gc_s^2\bar{\rho}\delta \tag{1.80}$$

$$\dot{\delta}+3H\left(c_s^2-w\right)\delta=-\frac{1}{a}(1+w)\left(\theta+3a\dot{\Phi}\right), \tag{1.81}$$

$$\dot{\theta}+\left[H(1-3w)+\frac{\dot{w}}{1+w}\right]\theta=\frac{k^2}{a}\nabla^2\left(\frac{c_s^2}{1+w}\delta+\Psi\right), \tag{1.82}$$

where, now $\theta=i\vec{k}.\vec{v}$. In above equations, we have used same symbols for $(\Phi,\Psi,\delta,\theta)$ to represent their Fourier space counter parts.

Among equations (1.77) - (1.82) only three are independent. By combining equations (1.77) and (1.78) we get

$$k^2\Phi=4\pi Ga^2\bar{\rho}\tilde{\delta}, \tag{1.83}$$

where $\tilde{\delta}=\left[\delta+3aH(1+w)\theta/k^2\right]$. Similarly, by combining equation (1.77) , (1.79) and (1.80) we get dynamical equation for $\Phi$, given by

$$\ddot{\Phi}+H(4+3c_s^2)\dot{\Phi}+\left(\frac{c_s^2k^2}{a^2}+3H^2c_s^2+3H^2+2\dot{H}\right)\Phi=0. \tag{1.84}$$

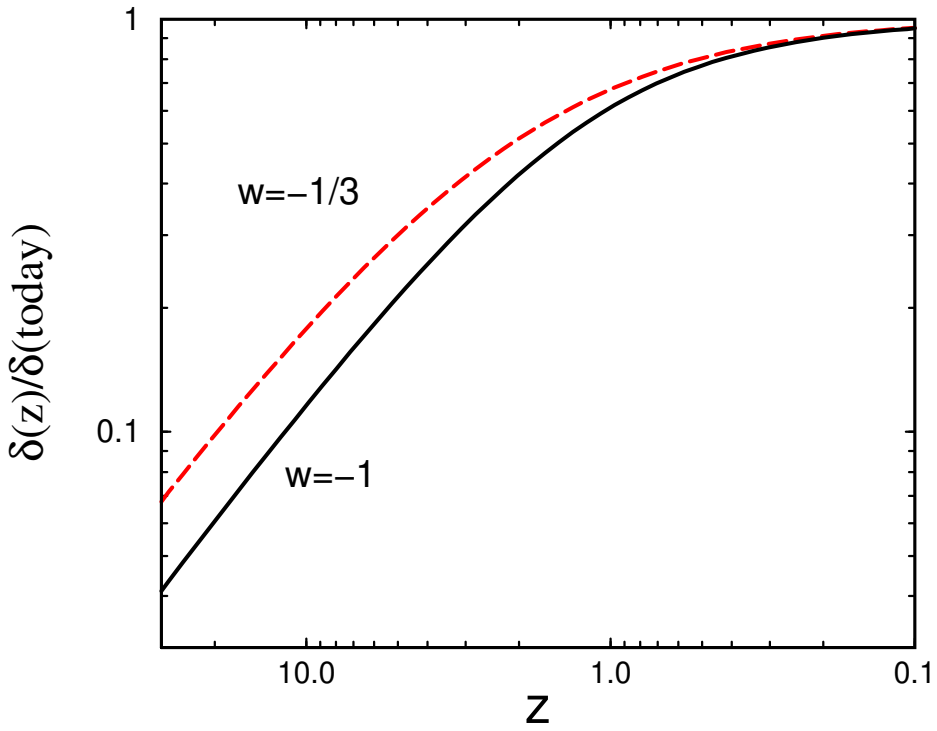


Figure 1.7: Evolution of linear growth factor $D_m^+ = \delta(z)/\delta(0)$ at sub-Hubble scale in a flat universe with dark energy. Here, a constant $w$ model of dark energy is considered with fixed $\Omega_{DE}$. Image credit - Frieman et.al.(2008) [64]. License agreement to reuse this figure is in appendix A.

In the long-wavelength limit $\lambda_p >> H^{-1}$ or equivalently $k << aH$. In this limit, for a single-component universe with $w = c_s^2 =$ constant (true for radiation and matter), equation (1.84) reduces to

$$\ddot{\Phi} + H(4 + 3c_s^2)\dot{\Phi} = 0. \tag{1.85}$$

Clearly, $\dot{\Phi} = 0$ is a solution to this equation. Now, neglecting $k^2\Phi$ term in the equation (1.77) we get

$$3H^2\Phi = 8\pi G\bar{\rho}\delta. \tag{1.86}$$

Substitution of $3H^2 = 8\pi G\bar{\rho}$ from the Friedmann equation reduces above equation to

$$\delta = 2\Phi. \tag{1.87}$$

Here, we can conclude that $\Phi =$ constant implies $\delta =$ constant in the long-wavelength limit. Thus we find that in a single-component universe with $c_s^2 = w$ at scale larger than the Hubble radius the gravitational potential remains constant. But, during the transition between two eras (e.g. transition from radiation to matter dominated era), this condition is violated.

Now, we show the results for sub-Hubble scale, i.e. for $k >> aH$. In this limit, equation (1.78) indicates that $\dot{\Phi} - H\Psi \approx 0$. Therefore, equation (1.77) reduces to $k^2\Phi = 4\pi G a^2 \bar{\rho}\delta$. Taking derivative with respect to $t$ and using equations (1.81) and (1.82) with straightforward algebra we get dynamical equation for density contrast, given by

$$\ddot{\delta} + 2H\dot{\delta} + \left(\frac{c_s^2 k^2}{a^2} - \frac{3}{2}H^2\right)\delta = 0. \tag{1.88}$$

If $H \to 0$ (the Minkowski limit), then equation (1.88) reduces to a fluid like wave equation $\ddot{\delta} + (c_s^2 k^2/a^2)\delta = 0$. Equation 1.88 shows that perturbations undergo damped oscillations and do not grow if $(c_s^2 k^2/a^2 - 3H^2/2) > 0$, i.e. if the physical length of perturbation $\lambda_p = 2\pi a/k$ is smaller than the Jeans length, $\lambda_J = c_s\sqrt{\pi/G\rho}$.

For the case $c_s k << aH$, gravity overcomes the pressure, and the perturbations grow freely. In this case, the sub-Horizon equation (1.88) for a single pressure less fluid becomes

$$\ddot{\delta} + 2H\dot{\delta} - 4\pi G\bar{\rho}\delta = 0. \tag{1.89}$$

Solution of above equation can be written in the form $\delta(\vec{x}, t) = D(t)\tilde{\delta}(\vec{x})$. Here, $\tilde{\delta}(\vec{x})$ is an arbitrary function of the spatial coordinate, and $D(t)$ satisfies the equation

$$\ddot{D} + 2H\dot{D} - 4\pi G\bar{\rho}D = 0. \tag{1.90}$$

This equation has two linearly independent solutions. The growing mode $D_+(t)$ increases with time, whereas other is the decreasing mode $D_-(t)$. As time progresses growing mode dominates, and decaying solution become irrelevant. If $D_+(t)$ is normalized such that $D_+(t_0) = 1$, then the solution of the equation (1.89) can be written as

$$\delta(\vec{x}, t) = D_+(t)\delta_0(\vec{x}), \tag{1.91}$$

where $D_+(t)$ is known as the 'linear growth factor' and $\delta_0(\vec{x})$ is 'linearly extrapolated density fluctuation field'. The form of solution (1.91) indicates that in linear theory only the amplitude of density fluctuation increases, its spacial shape remains frozen in comoving coordinates. In matter-dominated era $a(t) = (t/t_0)^{2/3}$, hence the solutions of the equation (1.89) come out to be

$$\delta_+ \propto a = (t/t_0)^{2/3}, \quad \delta_- \propto a^{-3/2} = (t/t_0)^{-1}. \tag{1.92}$$

Substituting $\delta_+$ into the Poisson equation (1.86), we get $\Phi \propto$ constant. Therefore, we conclude that in matter-dominated era, the gravitational potential remain constant.

Once the dark energy starts to dominate the energy budget and accelerates the expansion of the Universe, gravitational potential decays. Then, due to the Hubble damping term $2H\dot{D}$ in the equation (1.90), growth of matter is suppressed. Figure 1.7 shows the effect of dark energy on growth of linear growth factor $D_m^+ = \delta(z)/\delta(0)$ at sub-Hubble scale in a flat universe with dark energy. For dark energy a constant $w$ model is considered. Two cases with $w = -1/3$ and $-1$ are shown for a fixed value of dark energy density parameter $\Omega_{DE}$. Clearly, growth of matter perturbation comes to an end when dark energy starts to dominate, in this case at $z = (\Omega_m/\Omega_{DE})^{1/3w} - 1$. For a fixed $\Omega_{DE}$, larger the equation of state parameter $w$, it starts suppressing the growth of structure earlier . This means, to achieve the same amplitude today, it has to start with a larger amplitude and the growth needs to be faster at higher redshifts. This example shows that the observation of matter clustering at different redshifts can be used as a tool for studying nature and behavior of dark energy. In above analysis, dynamical nature of dark energy and clustering in it are neglected. Such a analysis for the tachyon model and a comparison with $\Lambda CDM$ model are shown in the chapter 3.

Analysis becomes more complicated in the case of a multicomponent fluid with time dependent $w$ and $c_s^2$. At cosmological scales, it is sufficient to consider the components of our universe to be photons, neutrinos, baryons, dark matter and dark energy. All these components contribute to the background density and drive expansion. When these components get perturbed, a density contrast $\delta_A = \delta\rho_A/\bar{\rho}_A$ arises for each component. In this case, it is $\delta_{total} = \delta\rho_{total}/\bar{\rho}_{total}$, where $\delta\rho_{total} = \sum\bar{\rho}_A\delta_A$ and $\bar{\rho}_{total} = \sum\bar{\rho}_A$, leads to a perturbed gravitational potential that drives the instability. Then, this potential further drives the inhomogeneities whereas the expansion of the Universe works against it. In chapter 3, we present a study on growth of perturbation in presence of dark matter fluid with perturbed tachyon scalar field dark energy as well as with a smooth cosmological constant background.

Linear theory breaks down when $|\delta| \gtrsim 1$, because approximations we made are no longer valid. In this case over dense regions decouple from cosmic expansion and grow independently. Mathematical formalism to study such a non-linear structure, e.g. 'spherical collapse model', is well established. Details of such formalism and along with linear perturbation theory can be found in [55, 56, 88, 90]. After setting up the mathematical machinery in linear perturbation theory, we also need statistical tools to quantify results and compare them with observations.

### 1.5.4 Correlation Function and Power Spectrum

In this section we introduce the statistical tools to quantify the order of clustering or structures in the Universe. It is clear that no simulation can generate the same copy of the Universe we live in, i.e., it is not possible to create the same distribution of matter around our galaxy (Milky way) as we see. Instead, we can at best generate, using laws of physics, a universe which is statistically similar to our universe. Structures in the Universe are formed in the form of galaxies. These galaxies are not distributed randomly, rather they are found in groups, clusters or even in super clusters. Therefore, it is more probable to find a galaxy near another. To quantitatively describe this fact, we consider two locations $\mathbf{x}$ and $\mathbf{y}$ with a volume element $dV$ around them. If the average number density of galaxy is $\bar{\rho}_n$, then the average number of particle in volume element $dV$ is $\bar{\rho}_n dV$. Now, the average number of pairs at $\mathbf{x}$ and $\mathbf{y}$ separated by distance $r_{xy} = |\mathbf{x}-\mathbf{y}|$ is given by

$$dN_{xy} = \langle n_x n_y \rangle = (\bar{\rho}_n dV)^2[1 + \xi_g(\mathbf{r_{xy}})]. \tag{1.93}$$

This equation defines the 'two-point correlation function $\xi(r)$' of galaxies. The averaging is done over an ensemble of distributions that have identical statistical properties. The Universe is considered as statistically homogeneous, therefore, the correlation function $\xi$ can only depend on separation $\mathbf{r} = \mathbf{x}-\mathbf{y}$, not on a specific location. Then the ensemble average can be replace by spatial averaging, i.e., the system is ergodic. This is important because we have only one universe available to measure. Clearly, if the distribution of galaxies are uncorrelated (and distribution is completely random) then the average number of pairs $dN_{xy} = \langle n_x n_y \rangle = (\bar{\rho}_n dV)^2$ is just the product of particles at both locations. In this case the correlation function $\xi$ vanishes. If it is non-zero, then

$$\xi(r_{xy}) = \frac{dN_{xy}}{(\bar{\rho}_n dV)^2} - 1 = \langle \delta(r_x)\delta(r_y) \rangle, \tag{1.94}$$

where we have used the relations $\delta(r_x) = n_x/\bar{\rho}_n dV$ and $\langle \delta(r_x) \rangle = \langle \delta(r_y) \rangle = 0$. In equation (1.94), the average is sample average, the two-point correlation function can be written as

$$\xi(\mathbf{r}) = \frac{1}{V} \int \delta(\mathbf{y})\delta(\mathbf{y}+\mathbf{r}) dV_y, \tag{1.95}$$

where the integration is over specified volume $V$ at all possible locations $y$. If we further impose the condition of isotropy, correlation function only depends on $|\mathbf{r}|$, i.e., $\xi \equiv \xi(r)$.

An alternate description of the structure formation in the Universe is the 'power spectrum' $P(k)$. It describes the level of clustering at length scale $\lambda = 2\pi/k$, where $k$ is wave number. Higher the value of power spectrum $P(k)$, larger the amplitude of fluctuations on the length scale $2\pi/k$. In linear theory, the density fluctuations can be decomposed into a sum of plane waves, i.e., $\delta(\mathbf{x}) = \sum A_k cos(\mathbf{x}.\mathbf{k})$. Then, $P(k)$ describes the distribution of amplitudes $A_k$ with equal $k = |\mathbf{k}|$. The power spectrum is defined as

$$P(k) = V|\delta_k|^2 = V\delta_k\delta_k^*. \tag{1.96}$$

Here $\delta_k$ is Fourier coefficient of the density contrast $\delta(\mathbf{x})$. We can see that the power spectrum has the dimension of volume. Using equation (1.95), the equation (1.96) can be written as

$$\begin{aligned} P(k) &= \frac{1}{V}\int \delta(\mathbf{x})\delta(\mathbf{y})e^{-i\mathbf{k}.(\mathbf{x}-\mathbf{y})}dV_x dV_y \\ &= \int \xi(\mathbf{r})e^{-i\mathbf{k}.\mathbf{r}}dV. \end{aligned} \tag{1.97}$$

We can see that the power spectrum is the Fourier transform of the correlation function. This is known as 'Wiener-Khinchin theorem'. Imposing isotropy in equation (1.97), we get

$$P(k) = 4\pi\int \xi(r)\frac{sin\ kr}{kr}r^2 dr. \tag{1.98}$$

The power spectrum is an important quantity in the structure formation study. We can relate other quantities of interest with it. A popular way to describe power on a particular scale $R$ is to compute rms fluctuation in a sphere of radius $R$, i.e., $\sigma_R^2 = \langle\delta_R^2(x)\rangle$, where

$$\delta_R^2(\mathbf{x}) = \int d^3x'\delta(\mathbf{x}')W_R(\mathbf{x}-\mathbf{x}'). \tag{1.99}$$

Here $W_R(x) = 1$ for $x < R$ and 0 otherwise, and it is known as the tophat window function. In terms of power spectrum $P(k)$, the rms fluctuation $\sigma_R$ can be reduced as

$$\sigma_R^2 = \frac{1}{2\pi^2}\int P(k)W_R^2(k)k^2 dk, \tag{1.100}$$

where, $W_R(k)$ is the Fourier coefficient of tophat window function. For more details on correlation function, power spectrum and other statistical quantities see [56, 87]
.

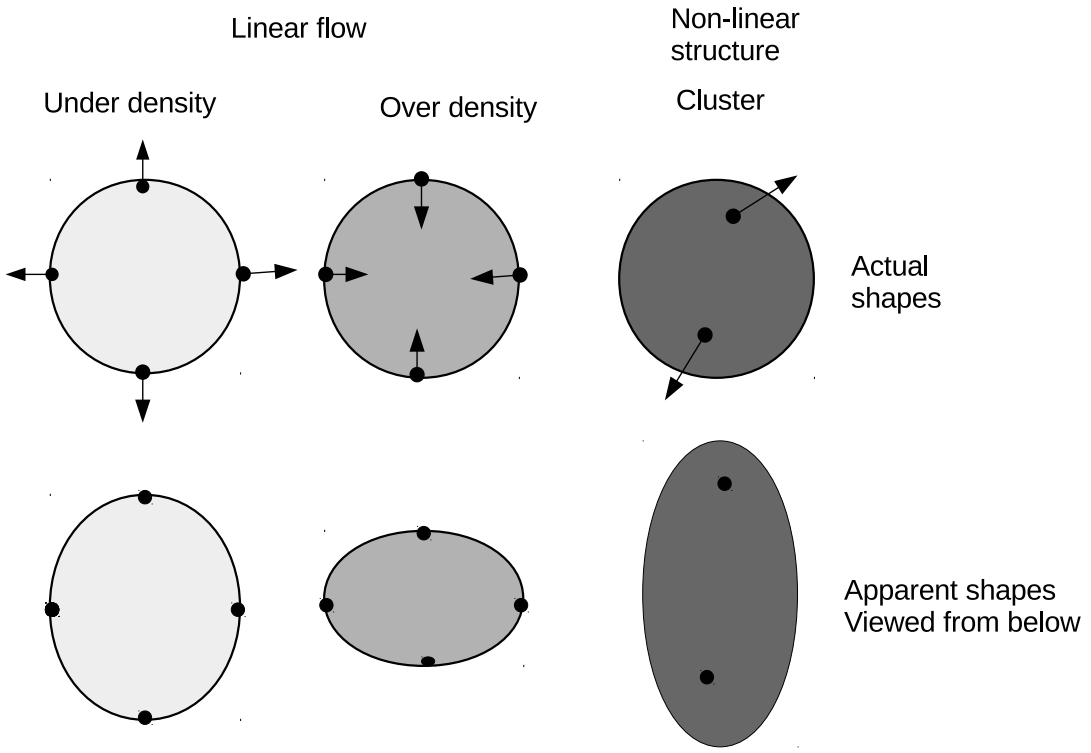


Figure 1.8: Schematic diagram showing how real space space shapes change in redshift space. Darker shades represent higher oder of clustering.

### 1.5.5 Peculiar Velocity and Redshift Space Distortion

The distances of galaxies are measured through their redshift. The measured redshift of a galaxy includes contribution of peculiar velocity. So, there is an error in distance measurement. Due to the peculiar velocity the position of a galaxy in redshift space is actually distorted in comparison with the real space. Let us consider a slightly overdense spherical region of galaxies. In this region, galaxies will move towards the centre of overdense region. The galaxies closer to us move away from us and appear farther from us than they actually are. Similarly, the galaxies of other side move toward us and appear closer to us than they actually are. Because of this, there is an apparent quadrupole moment in a circular overdense region. In figure 1.8, we schematically show how the actual shapes of underdense, overdense and non-linear structures change in redshift space. In nonlinear overdense region the nature of radshift space distortion is different from linear region. In nonlinear region, the sign of quadrupole moment is opposite to that in linear region. We restrict ourselves to linear overdensity for the purpose of our discussion.

To extract the correlation function or power spectrum from some redshift survey, we need first to find out how these distorted quantities are related to their true real

space spectrum. This relation was derived for linear theory by Nick Kaiser [91]. Up to the first oder, the over-density in redshift space is sum of the over-density in real space and contribution due to peculiar velocity [88], i.e.,

$$\delta_s(\mathbf{x}) = \delta(\mathbf{x}) - \frac{\partial}{\partial x}\left[\frac{\mathbf{v}(\mathbf{x})\cdot\hat{\mathbf{x}}}{H_0}\right]. \tag{1.101}$$

Here subscript 's' is for quantity in redshift space. The second term in the right hand side is due to the peculiar velocity. In the distant observer approximation the Fourier-transformation of equation (1.101) reduced to [88]

$$\delta_s(\mathbf{k}) = \left[1 + f\mu_{\mathbf{k}}^2\right]\delta(\mathbf{k}). \tag{1.102}$$

Here $\mu_{\mathbf{k}}$ is the cosine of the angle between wevevector $\mathbf{k}$ and the line of sight. Quantity $f$ is the dimension less linear growth rate, define as,

$$f = \frac{d\ ln\ \delta}{d\ ln\ a}. \tag{1.103}$$

Since $f\mu_{\mathbf{k}}^2 > 0$, the overdensity in redshift space appears larger than in the real space. From equation (1.102), we can calculate the relation for power spectra in redshift space and real space as [88]

$$P_s(\mathbf{k}) = P(\mathbf{k})\left[1 + \beta\mu_{\mathbf{k}}^2\right]^2. \tag{1.104}$$

Here the parameter $\beta$ accounts for the fact that the mass density $\delta$ is not necessarily equal to the galaxies overdensity $\delta_g$. The velocity samples the mass density, i.e. $\mathbf{v} \propto \delta \propto \delta_g/b$, where '$b$' is bias defined as

$$b = \frac{\delta_g}{\delta}, \tag{1.105}$$

and hence the parameter $\beta = f/b$. According to the equation (1.104), by measuring the redshift space distortion we can compute $\beta$, a combination of linear growth rate and bias. This can be achieved by measuring the ratio of the quadrupole to the monopole of the power spectrum [9, 88, 92].

## 1.6 Statistical Analysis and Observational Data

A model is characterized by a hypothesis and set of parameters. Bayesian statistics has been a standard tool for testing viability of a model, estimation of likelihood,

and for comparison between models. We have a rich sets of cosmological data to achieve this purpose. According to the Bayes theorem, the posterior probability of a model parameters $\mathbf{p} \equiv (p_1,\ p_2,\ ...)$ of a model $M$ for a given data set $D$ is given by [93, 94, 95]

$$\mathscr{P}(\mathbf{p}|D,M) = \frac{\mathscr{P}(D|\mathbf{p},M)\mathscr{P}(\mathbf{p}|M)}{\mathscr{P}(D|M)}. \tag{1.106}$$

Here, $\mathscr{P}(\mathbf{p}|M)$ is prior probability distribution of $\mathbf{p}$ before arrival of data , and it is often taken to be flat. Quantity $\mathscr{P}(D|\mathbf{p},M)$ is likelihood of data. Denominator $\mathscr{P}(D|M)$ is a normalization constant, known as 'Bayesian evidence'. It is to ensure that the posterior is normalized, hence given by [93, 94, 95]

$$Evidence \equiv \mathscr{P}(D|M) = \int \mathscr{P}(D|\mathbf{p},M)\mathscr{P}(\mathbf{p}|M)d\mathbf{p}. \tag{1.107}$$

Bayesian evidence is an important quantity for model selection. Clearly, posterior of parameter $\mathbf{p}$ can be calculated by computing the likelihood $\mathscr{P}(D|\mathbf{p},M)$.

### 1.6.1 Likelihood and Confidence Intervals

By maximizing likelihood $\mathscr{L}(\mathbf{p}) \equiv \mathscr{P}(D|\mathbf{p},M)$ we can find most likely parameters for given data. If the distribution of data points are Gaussian then the likelihood $\mathscr{L}(\mathbf{p}) \propto exp(-\chi^2/2)$, where $\chi^2$ is defined as [93, 94, 95, 96]

$$\chi^2(\mathbf{p}) = \sum_{i,j=1}^{N} [X_{th,i}(\mathbf{p}) - X_{obs,i}] C^{-1}_{i,j} [X_{th,j}(\mathbf{p}) - X_{obs,j}], \tag{1.108}$$

where $N$ is the number of data points in the dataset, $X_{th}$ is a vector of the theoretical value of corresponding observable, and $X_{obs}$ is a vector of the observational values. $C_{ij}$ is the covariance matrix of data points. The posterior distribution of a particular parameter in the set $\mathbf{p} \equiv (p_1,\ p_2,\ ...)$ can be computed by marginalizing $\chi^2(\mathbf{p})$ over other parameters, e.g., for parameter $p_1$

$$\chi^2(p_1) = \frac{\int \chi^2(\mathbf{p}) e^{-\chi^2(\mathbf{p})/2} d(p_2,\ p_3, ...)}{\int e^{-\chi^2(\mathbf{p})/2} d(p_2,\ p_3, ...)}. \tag{1.109}$$

Similarly, distribution of $\chi^2$ in two dimensional parameter space $(p_i,\ p_j)$ can be estimated by marginalizing $\chi^2(\mathbf{p})$ over rest of the parameters.

Clearly, we can maximize likelihood by minimizing $\chi^2(\mathbf{p})$. A point in the parameter space corresponding to its minimum value, $\chi^2_{min}(\mathbf{p})$, provides values of most

likely parameters. A given confidence region around this point can be estimated using condition $\chi^2 < \chi^2_{min} + \Delta\chi^2$. The value of $\Delta\chi^2$ depends on the number of parameters and required confidence limit. It can be calculated from $\chi^2$-distribution function [97], given by

$$F(z) = \frac{1}{2^{m/2}\Gamma(m/2)} \int_0^z e^{-u/2} u^{(m-2)/2} du. \tag{1.110}$$

Here, $m$ is the number of parameters and $z = \Delta\chi^2$ which is to be added to $\chi^2_{min}$ to get required confidence interval. For two dimensional parameter plane $m = 2$, then equation (1.110) reduces to $z = -2\ ln[1 - F(z)]$. Therefore, in two dimensional parameter space 68%, 95% and 99% confidence intervals correspond to $\Delta\chi^2 =$ 2.28, 5.99 and 9.21.

### 1.6.2 Bayesian Model Comparison

The Bayesian evidence or marginal likelihood, defined in equation (1.107), is a measure of model's performance. Two models $M_0$ and $M_1$ can be compare using ration of their posterior probabilities or posterior odds [94, 95], as

$$\frac{\mathscr{P}(M_0|D)}{\mathscr{P}(M_1|D)} = \frac{\mathscr{P}(D|M_0)}{\mathscr{P}(D|M_1)} \frac{\mathscr{P}(M_0)}{\mathscr{P}(M_1)}. \tag{1.111}$$

Here, first term in right hand side is a ratio of Bayesian evidences of models, and known as 'Bayes factor', given by

$$B_{01} \equiv \frac{E_0}{E_1} = \frac{\mathscr{P}(D|M_0)}{\mathscr{P}(D|M_1)}. \tag{1.112}$$

Bayes factor indicates the change in relative odds between models after arrival of data. If $B_{01} > 1$ then we conclude model that $M_0$ is more favorable by the data, if not then conclusion is otherwise. An empirically calibrated scale for strength of evidence to compare the models is provided by the Jeffrey's scale [98] given in table 1.1.

For a complex model with many parameters, it is difficult to solve integration in the equation (1.107). There are alternate information criteria for model selection, simpler to use, those depends only on maximum likelihood rather than the likelihood over whole parameter space. Example of such information criteria includes the Akaike information criterion (AIC) and the Bayesian information criterion (BIC) [93, 94, 95]. These criteria are derived using some assumptions, e.g., Gaussianity or near-Gaussianity of the posterior distribution [93, 94]. These as-

| $\|ln\ B_{01}\|$ | odds | Probability | Strength of evidence |
|---|---|---|---|
| $< 1.0$ | $\lesssim 3:1$ | $< 0.750$ | Inconclusive |
| 1.0 | $\sim 3:1$ | 0.750 | Weak |
| 2.5 | $\sim 12:1$ | 0.923 | Moderate |
| 5.0 | $\sim 150:1$ | 0.993 | Strong |

Table 1.1: Empirical Jeffrey's scale for the strength of evidence when comparing two models $M_0$ versus $M_1$ [98]. The probabilities (posterior) are calculated assuming non-committal priors on the two competing models, i.e. $\mathscr{P}(M_0) = \mathscr{P}(M_1) = 1/2$ and $\mathscr{P}(M_0) + \mathscr{P}(M_1) = 1$ [96].

sumption may not be valid in real situations. The AIC and BIC for a model are defined as [93, 94, 95]

$$\begin{aligned} AIC &= -2\ ln\ \mathscr{L}_{max} + 2k \\ BIC &= -2\ ln\ \mathscr{L}_{max} + k\ ln\ N \end{aligned} \tag{1.113}$$

where, $\mathscr{L}_{max}$ is the maximum likelihood, $k$ is the number of parameters of model, and $N$ is the number of data points. The best model is one which minimizes AIC and BIC. It is assume that data points are independent and identically distributed [93]. In presence of parameter degeneracy, inclusion of an unconstrained parameters is do not penalized by evidence, but by the AIC and BIC [93]. Therefore, one should consider all these boundaries before selection of information criteria to use it for model selection. A detail discussion on Bayesian model selection can be found in [93, 94, 95, 96, 97]. In next sections, we describe the data sets used in this thesis with the statistical tool described above to find constraints on the model parameters. These include the Baryon acoustic oscillation data, the Hubble parameter data, the Supernova type Ia data, and the redshift space distortion data.

### 1.6.3 Baryon Acoustic Oscillation Data

The oscillation feature in the correlation function of large scale structure (LSS) is known as the Baryon Acoustic Oscillations (BAO) [99, 100, 101, 102, 103, 104, 105]. The opposing forces of gravity and radiation pressure in the pre-recombination baryon - photon plasma resulted in acoustic waves in it. These waves left their imprint on the baryonic clustering and gave rise to the BAO peaks. The characteristic angular scale of these peaks is given by $\theta_A = r_s(z_d)/D_V(z)$, where $D_V$ is effective distance ratio, and it can be calculated using the angular diameter distance $D_A(z)$ as follows

$$D_V(z) = \left[(1+z)^2 D_A(z)^2 \frac{cz}{H(z)}\right]^{1/3}. \tag{1.114}$$

| Measurement | Redshift | BAO data | $C_{ij}$ | | | | | |
|---|---|---|---|---|---|---|---|---|
| $D_M(r_{d,fid}/r_d)$ | 0.38 | 1512 | 624.707 | 23.729 | 325.332 | 8.34963 | 157.386 | 3.57778 |
| $H(r_d/r_{d,fid})$ | 0.38 | 81.2 | 23.729 | 5.60873 | 11.6429 | 2.33996 | 6.39263 | 0.968056 |
| $D_M(r_{d,fid}/r_d)$ | 0.51 | 1975 | 325.332 | 11.6429 | 905.777 | 29.3392 | 515.271 | 14.1013 |
| $H(r_d/r_{d,fid})$ | 0.51 | 90.9 | 8.34963 | 2.33996 | 29.3392 | 5.42327 | 16.1422 | 2.85334 |
| $D_M(r_{d,fid}/r_d)$ | 0.61 | 2307 | 157.386 | 6.39263 | 515.271 | 16.1422 | 1375.12 | 40.4327 |
| $H(r_d/r_{d,fid})$ | 0.61 | 99.0 | 3.57778 | 0.968056 | 14.1013 | 2.85334 | 40.4327 | 6.25936 |

Table 1.2: BAO data from Baryon Oscillation Spectroscopic Survey (BOSS) DR12 [2]. Here, the comoving angular diameter distance $D_M$ is in $Mpc$ and the Hubble parameter $H$ is in $km\ s^{-1}Mpc^{-1}$. The fiducial value of sound horizon $r_{s,fid} = 147.78\ Mpc$. The last six columns show the covariance elements of matrix $C_{ij}$.

| Measurement | Redshift | BAO data | $C_{ij}$ | |
|---|---|---|---|---|
| $D_A(r_{d,fid}/r_d)$ | 0.32 | 956 | 0.77636E+03 | 0.43793E+02 |
| $H(r_d/r_{d,fid})$ | 0.32 | 95.0 | 0.43793E+02 | 0.16253E+02 |
| $D_A(r_{d,fid}/r_d)$ | 0.59 | 1421 | 0.53559E+03 | 0.27875E+02 |
| $H(r_d/r_{d,fid})$ | 0.59 | 96.7 | 0.27875E+02 | 0.74866E+01 |

Table 1.3: BAO data for LOWZ and CMASS at redshift $z = 0.32$ and 0.59 respectively taken from [106]. The fiducial value of sound horizon $r_{s,fid} = 147.66\ Mpc$. Last four columns show the elements of covariance matrix $C_{ij}$ for both the data sets.

and $r_s$ is sound horizon at drag epoch $z_d$, which is given by

$$r_s(z_d) = \int_{z_d}^{\infty} \frac{c_s(z)}{H(z)} dz, \tag{1.115}$$

We use the BAO data from Baryon Oscillation Spectroscopic Survey (BOSS) DR12 [2] which provides 6 data points (see table-7 of Alam et al.) at redshifts $z = 0.38,\ 0.51,\ 0.61$ in terms of $H(z)r_s(z_d)/r_{s,fid}$ and $D_M(z)r_{s,fid}/r_s(z_d)$ where $r_{s,fid} = 147.78\ Mpc$ and $D_M(z) = (1+z)D_A(z)$ is the comoving angular diameter distance. The sound horizon $r_s(z_d)$ given by [107]

$$r_s(z_d) = \frac{55.154 \exp[-72.3(\omega_\nu + 0.0006)^2]}{\omega_b^{0.12807}\omega_{cb}^{0.25351}} \text{Mpc}, \tag{1.116}$$

where $\omega_\nu = \Omega_\nu h^2 = 0.0107(\sum m_\nu/1.0eV)$, $\omega_b = \Omega_b h^2$ and $\omega_{cb} = \Omega_m h^2 - \omega_\nu$. Symbols $\Omega_\nu$, $\Omega_b$ and $\Omega_m$ represent density parameters of neutrinos, baryons and non-relativistic matter (baryonic matter + dark matter). We set mass of neutrinos $\sum m_\nu = 0.06$ eV and $\Omega_b h^2 = 0.02225$ with $h = 0.676$. We have tabulated this data along with the covariance matrix $C_{ij}$ in table 1.2.

We also use BAO data from LOWZ and CMASS at redshift $z = 0.32$ and 0.59 as given in reference [106]. Here $r_{s,fid} = 147.66$ Mpc and the approximation for

| Sample | Redshift | A(z) |
|---|---|---|
| 6dFGS | 0.106 | $0.526 \pm 0.028$ |
| SDSS | 0.2 | $0.488 \pm 0.016$ |
| SDSS | 0.35 | $0.44 \pm 0.016$ |
| WiggleZ | 0.44 | $0.474 \pm 0.034$ |
| WiggleZ | 0.6 | $0.442 \pm 0.020$ |
| WiggleZ | 0.73 | $0.424 \pm 0.021$ |

Table 1.4: BAO data from 6dFGS, SDSS DR7 and WiggleZ in term of the acoustic parameter A(z).

$r_s(z_d)$ is the same as shown in equation (1.116). These data sets are tabulated in table 1.3. We also use older BAO data from 6dFGS, SDSS DR7 and WiggleZ at redshifts $z = 0.106,\ 0.2,\ 0.35,\ 0.44,\ 0.6$ and $0.73$. These are listed in table-3 of [108] in term of the acoustic parameter. The acoustic parameter [109] is

$$A(z) = \frac{100 D_A \sqrt{\Omega_m h^2}}{cz}. \tag{1.117}$$

Here $c$ is the speed of light in vacuum. In table 1.4 we show these older BAO data set in term of the acoustic parameter.

### 1.6.4 Hubble Parameter Data

We also use the measurement of cosmic expansion rate in terms of the Hubble parameter. The Hubble parameter can be computed from the Friedmann equation and is given by

$$H(z) = H_0 \left[\Omega_{m0}(1+z)^3 + \Omega_{r0}(1+z)^4 + \Omega_\phi\right]^{1/2}, \tag{1.118}$$

where $H_0$ is the present value of the Hubble parameter. The Hubble parameter data set [62, 110, 111, 112, 113, 114, 115, 116] consists of values of Hubble parameters $H(z)$ at different redshifts and associated errors in the measurement. In table 1.5 we show the Hubble parameter data set (H(z) data set) up to redshift $z = 2.36$ along with the references. This data set is also compiled and listed in table-1 of [110]. The table contains values of the Hubble parameters at 38 different redshifts. Out of 38 we use only 32 (listed in table 1.5 ) points as we do not consider three data points taken from Alam et. al.(2016) at redshifts $z =$ 0.38, 0.51, 0.61 and three data points taken from Black et. al.(2012) at redshifts $z =$ 0.44, 0.6, 0.73. We do it to make data sets independent because we include these data points in our BAO dataset (see subsection 1.6.3).

| $z$ | $H(z)$ | $\sigma_H$ | Reference | $z$ | $H(z)$ | $\sigma_H$ | Reference |
|---|---|---|---|---|---|---|---|
| 0.070 | 69 | 19.6 | [117] | 0.480 | 97 | 62 | [113] |
| 0.090 | 69 | 12 | [118] | 0.593 | 104 | 13 | [114] |
| 0.120 | 68.6 | 26.2 | [117] | 0.680 | 92 | 8 | [114] |
| 0.170 | 83 | 8 | [118] | 0.781 | 105 | 12 | [114] |
| 0.179 | 75 | 4 | [114] | 0.875 | 125 | 17 | [114] |
| 0.199 | 75 | 5 | [114] | 0.880 | 90 | 40 | [113] |
| 0.200 | 72.9 | 29.6 | [117] | 0.900 | 117 | 23 | [118] |
| 0.270 | 77 | 14 | [118] | 1.037 | 154 | 20 | [114] |
| 0.280 | 88.8 | 36.6 | [117] | 1.300 | 168 | 17 | [118] |
| 0.352 | 83 | 14 | [114] | 1.363 | 160 | 33.6 | [119] |
| 0.3802 | 83 | 13.5 | [120] | 1.430 | 177 | 18 | [118] |
| 0.400 | 95 | 17 | [118] | 1.530 | 140 | 14 | [118] |
| 0.4004 | 77 | 10.2 | [120] | 1.750 | 202 | 40 | [118] |
| 0.4247 | 87.1 | 11.2 | [120] | 1.965 | 186.5 | 50.4 | [119] |
| 0.4497 | 92.8 | 12.9 | [120] | 2.340 | 222 | 7 | [105] |
| 0.4783 | 80.9 | 9 | [120] | 2.360 | 226 | 8 | [121] |

Table 1.5: Hubble parameters $H(z)$ and error in its measurements $\sigma_H$ at different redshift. These quantities are in $km\ s^{-1}Mpc^{-1}$.

### 1.6.5 Supernova Type Ia Data

The supernova type Ia is supernova explosion of a white dwarf star. Supernova are classified by their light curves and supernova type Ia is characterized by the absence of H-line and presence of strong Si absorption lines in the spectra. When a white dwarf star accreting mass from its binary companion crosses the Chandrasekhar limit of $1.4M_\odot$ it explodes [122]. This is a supernova explosion of Type-Ia. Since at the time of explosion its mass is known we can calculate the luminosity of explosion and hence its luminosity distance [4, 5, 63, 123, 124, 125, 126, 127, 128, 129]. The supernova Ia serves is therefore a 'standard candle' [130]. Therefor, observation of the supernova Ia provide us a means to find out distance-redshift relation. The theoretical value of the luminosity distance of Supernova-Ia which occurred at redshift $z$ is given by equation (1.58).

For our analysis, we use the supernova Ia data from Supernova Cosmology Project (SCP) "Union2.1" SN Ia compilation. In SN-Ia data, we have distance moduli of 580 supernovae up to redshifts $z = 1.414$ along with their associated observational error [123]. The theoretical values of distance modulus can be calculated using luminosity distance as

$$\mu = 5log(d_L) - 5, \tag{1.119}$$

here $d_L$ is in the unit of 10 $pc$ and $\mu = m - M$ is the distance modulus, $m$ and $M$ are

| $z$ | $f\sigma_8(z)$ | $\sigma_{f\sigma_8}$ | $\Omega_{m0}^{fed.}$ | Ref. |
|---|---|---|---|---|
| 0.02 | 0.428 | 0.0465 | 0.3 | [132] |
| 0.02 | 0.398 | 0.065 | 0.3 | [133, 134] |
| 0.02 | 0.314 | 0.048 | 0.226 | [134, 135] |
| 0.10 | 0.370 | 0.130 | 0.3 | [136] |
| 0.15 | 0.490 | 0.145 | 0.31 | [137] |
| 0.17 | 0.510 | 0.060 | 0.3 | [131] |
| 0.18 | 0.360 | 0.090 | 0.27 | [138] |
| 0.25 | 0.3512 | 0.0583 | 0.25 | [139] |
| 0.32 | 0.384 | 0.095 | 0.274 | [140] |
| 0.37 | 0.4602 | 0.0378 | 0.25 | [139] |
| 0.38 | 0.440 | 0.060 | 0.27 | [138] |
| 0.44 | 0.413 | 0.080 | 0.27 | [102] |
| 0.59 | 0.488 | 0.060 | 0.307115 | [141] |
| 0.60 | 0.550 | 0.120 | 0.3 | [142] |
| 0.60 | 0.390 | 0.063 | 0.27 | [102] |
| 0.73 | 0.437 | 0.072 | 0.27 | [102] |
| 0.86 | 0.400 | 0.110 | 0.3 | [142] |
| 0.978 | 0.379 | 0.176 | 0.31 | [143] |
| 1.40 | 0.482 | 0.116 | 0.27 | [144] |
| 1.23 | 0.385 | 0.099 | 0.31 | [143] |
| 1.526 | 0.342 | 0.070 | 0.31 | [143] |
| 1.944 | 0.364 | 0.106 | 0.31 | [143] |

Table 1.6: Values of measurements of $f\sigma_8(z)$ at different redshift along with error and values of fiducial $\Omega_{m0}^{fed.}$. Last column shows the references from where values have been taken.

the apparent and absolute magnitude respectively of the supernova.

### 1.6.6 Redshift Space Distortion Data

In section 1.5.5, we discussed how by measuring radshift space distortion we can find out the parameter $\beta$ $(= f/b)$ which is combination of growth rate of matter $f$ and galaxy bias $b$. The parameter $\beta$ is sensitive for bias, which varies in the range $b \in [1, 3]$ for different observations [9]. This makes difficult to combine data from different observations and decreases the reliability of data set. The more reliable quantity is the combination $f(z)\sigma_8(z) = f\sigma_8(z)$, where $\sigma_8(z)$ is rms fluctuations of the linear density field within spheres of radius $R = 8h^{-1}Mpc$. It is independent of bias and can be obtained either by redshift space distortion or weak lensing [9, 92, 131].

In table 1.6, we show the compilation $f\sigma_8(z)$ from different observations based

on redshift space distortion measurement along with corresponding error in measurements, fiducial cosmology and references. In our analysis we use these 22 data points from redshift 0.02 to 1.944, out of which 18 points are compiled in table III of [9] with their fiducial cosmology and references. This compilation is named as 'Gold-2017' data set. We have added four more data points at redshift 0.978, 1.23, 1.526 and 1.944 from [143] for our analysis. All these 22 data points, with the value of $f\sigma_8(z)$, error, fiducial cosmology and corresponding references, are tabulated in table I of [92].

$$C_{WiggleZ} = 10^{-3}\begin{pmatrix} 6.400 & 2.570 & 0.000 \\ 2.570 & 3.969 & 2.540 \\ 0.000 & 2.540 & 5.184 \end{pmatrix} \tag{1.120}$$

$$C_{SDSS-IV} = 10^{-2}\begin{pmatrix} 3.098 & 0.892 & 0.329 & -0.021 \\ 0.892 & 0.980 & 0.436 & 0.076 \\ 0.329 & 0.436 & 0.490 & 0.350 \\ -0.021 & 0.076 & 0.350 & 1.124 \end{pmatrix} \tag{1.121}$$

In this data set, three WiggleZ points [102] are correlated and their covariance matrix is given in equation (1.120). The four high recent high redshift data point from [143] are also correlated and their covariance matrix is given in equation (1.121). All these data are actually depended on fiducial model used to convert redshift ot distance [9]. The fiducial model for data points in table 1.6 is flat-$\Lambda CDM$ with value of $\Omega_{m0}$ given in column-4. To use this data set we first need to correct for this fiducial cosmology. We explain the method, as suggested in [9], to do this in section 3.3.

The aim of this thesis is to explore cosmology in context of the tachyon dark energy model. In first part of this work, we assume tachyon dark energy as a homogeneous field and update constraints on this model as well as on cosmological parameters. For this work, we use low redshift background data (described in section 1.6). Then in light the parameter allowed by observation, we explore the expansion history of the Universe. This work is explained in chapter 2. Effect of perturbations in tachyon dark energy on matter clustering is explained in the chapter 3. We compare the evolution of linear growth function and growth rate of matter for tachyon models with the $\Lambda CDM$ model. Using the 'redshift space distortion'(RSD) data we find constraints on $\Omega_m - w$ plane, and analyze the tension between Plank CMB data and growth rate data. In chapter 4 we present summary of this thesis.

# Chapter 2

# Low Redshift Constraints on Tachyon Dark Energy

**This chapter is adapted from following published article**

Avinash Singh, Archana Sangwan and H. K. Jassal, *Low redshift observational constraints on tachyon models of dark energy*, Journal of Cosmology and Astroparticle Physics **04** (2019)047. arXiv:1811.07513

In this chapter, we discuss the cosmological model in which dark energy is described by a homogeneous tachyon field. We consider two models; one with an inverse power law potential and another with an exponential potential which have been the default potentials used for studying tachyon field cosmology. We revisit the constraints on tachyon dark energy model with new datasets, Baryon Acoustic Oscillations (BAO) [99, 100, 101, 102, 103, 104, 105], Supernova Type Ia (SN-Ia) [4, 5, 63, 123, 124, 125, 126, 127, 128, 129] and direct measurements of Hubble parameter (H(z)) [62, 110, 111, 112, 113, 114, 115, 116]. Our motivation is to compare the constraints on the tachyon models from previous studies using the same datasets and to check if the non-canonical scalar field models prefer a different combination(s) of cosmological parameters. In this analysis, we have restricted ourselves to the low redshift datasets. We obtain stringent constraints on tachyon field parameters, by way of combining these datasets. The structure of this chapter is as follows. In the next section 2.1, we discuss the background cosmology in the presence of a tachyon field and two different scalar potentials. We discuss our results in section 2.2 for both the tachyon models, and summarize as well as conclude the chapter in section 2.3.

## 2.1 Solutions of Cosmological Equations

We consider a universe filled with a minimally coupled system of non-relativistic matter, radiation (relativistic components) and scalar field. The dynamics of the Universe, then, is governed by the Friedman equations, which are given by

$$\begin{aligned} \frac{\dot{a}^2}{a^2} &= \frac{8\pi G}{3}\left(\rho_m + \rho_r + \rho_\phi\right) \\ \frac{\ddot{a}}{a} &= -\frac{4\pi G}{3}(\rho + 3P), \end{aligned} \tag{2.1}$$

where $\rho = \rho_m + \rho_r + \rho_\phi$. The quantities $\rho_m$ and $\rho_r$ are energy densities of non-relativistic matter(baryonic matter + dark matter ) and relativistic matter respectively, whereas $\rho_\phi$ represents energy density of the tachyon field. As explained in section 1.2.3, $\rho_m \propto a^{-3}$ and $\rho_r \propto a^{-4}$, where 'a(t)' is scale factor of the expanding Universe. With an arbitrary potential $V(\phi)$, the energy density $\rho_\phi$ and pressure $P_\phi$ of tachyon field is given by equation (1.51). The equation of state parameter of tachyon scalar field, $w_\phi = \dot{\phi}^2 - 1$, is theoretically bounded between -1 and 0. Therefore, the tachyon field has no phantom like equation of state. The dynamics of this non-canonical field is explained by equation (1.52). In next subsections, we introduce the tachyon field potentials we have used for our analysis, and derive the dimensionless form of the required equations.

### 2.1.1 The Inverse Square Potential

A potential which describes a tachyon scalar field model of dark energy is given as

$$V(\phi) = \frac{n}{4\pi G}\left(1 - \frac{2}{3n}\right)^{1/2} \phi^{-2}, \tag{2.2}$$

where $n$ determines the amplitude of the potential. The inverse power-law potentials are known as the 'Ratra-Peebles potentials' [18, 145, 146], in quintessence. The inverse square potential leads to a cosmological evolution of the form $a = t^n$ [38]. Cosmological dynamics of tachyon scalar field dark energy with this potential have been studied in [37], and the stability analysis of this potential has been done in [39, 147, 148]. The cosmological dynamics depend on the quantity $\lambda = -M_n V^{-3/2} dV/d\phi$, which is a constant. With the slow-rolling condition, this leads to a stable critical fixed point for this potential which can generate a late time

accelerated expansion (with $n > 1$). This fixed point is an attractor which leads to $\Omega_\phi = 1$ and the equation of state parameter $w_\phi = 2/3n{-}1$ asymptotically. There still remains the requirement of a tuning, which is needed for a sufficient acceleration at the present time [39, 147].

To numerically solve the cosmological equations, we transform the above equations by introducing the following dimensionless variables

$$y = \frac{a(t)}{a(t_{in})}, \quad \psi = \frac{\phi(t)}{\phi(t_{in})}, \qquad x = H_{in}t\,, \tag{2.3}$$

here '$t_{in}$' represents the initial time. The equations can then be written as

$$y' = y\left[\Omega_{m,in}y^{-3} + \Omega_{r,in}y^{-4} + \frac{\Omega_{\phi,in}\sqrt{-w_{\phi,in}}}{\psi^2\sqrt{1-\phi_{in}^2H_{in}^2\psi'^2}}\right]^{1/2}, \qquad \psi'' = \left(1-\phi_{in}^2H_{in}^2\psi'^2\right)\left[\frac{2}{\phi_{in}^2H_{in}^2\psi} - 3\psi'\frac{y'}{y}\right], \tag{2.4}$$

The prime on superscript denotes derivative with respect to $x = H_{in}t$, and different $\Omega$'s are dimensionless density parameters defined as the ratio of the density of the relevant component and critical density $\rho_{cr} = \frac{3H_0^2}{8\pi G}$. Here, we have assumed the Universe to be spatially flat and hence $\Omega_{total} = \Omega_{m,in} + \Omega_{r,in} + \Omega_{\phi,in} = 1$.

We integrate the equations numerically from the present time ($t_{in} = t_0$) to early times, and $\Omega_{m0}$, $\phi_0H_0$ and $\dot{\phi}_0$ or $w_{\phi0}$ are the parameters which are varied. The amplitude of the potential can be constrained by using the relation

$$\frac{2n}{3}\left(1-\frac{2}{3n}\right)^{1/2} = \Omega_{\phi0}\phi_0^2H_0^2\sqrt{-w_{\phi0}}. \tag{2.5}$$

To calculate the value of $n$ from the above equation we need to solve the polynomial equation

$$12n^3 - 8n^2 - 27q^2n = 0, \tag{2.6}$$

where $q = \Omega_{\phi0}\phi_0^2H_0^2\sqrt{-w_{\phi0}}$ is a positive number. The solution of equation (2.6) for accelerated expansion ($n > 1$) is

$$n = \frac{1}{3} + \frac{1}{6}\sqrt{4+(9q)^2}, \tag{2.7}$$

with the condition that $q > \frac{2\sqrt{3}}{9}$. The value of the present day radiation density parameter $\Omega_{r0}$ is [149]

$$\Omega_{r0} = \frac{\Omega_{m0}}{1+z_{eq}}, \tag{2.8}$$

where $z_{eq} = 2.5 \times 10^4 \Omega_{m0} h^2 (T_{cmb}/2.7K)^{-4}$, $T_{cmb} = 2.7255K$. The initial conditions for the numerical solutions are

$$y_0 = 1, \ \psi_0 = 1, \tag{2.9}$$

and $\psi_0'$ can be calculated using relation

$$\psi' = \frac{\dot{\phi}}{\phi_0 H_0} = \frac{\sqrt{1+w_\phi}}{\phi_0 H_0}. \tag{2.10}$$

### 2.1.2 The Exponential Potential

The exponential potential for tachyon scalar field dark energy is given by

$$V(\phi) = V_a \exp(-\phi/\phi_a), \tag{2.11}$$

where amplitude $V_a$ and $\phi_a$ are the scalar field parameters. Cosmological dynamics with this potential have also been studied in [37], and the stability analysis of this potential has been done in [39, 147, 148]. For this potential, $\lambda \to \infty$ as $\phi \to \infty$. This is a fixed point for which $\Omega_\phi \simeq 0$ and a dust like equation of state. Since $\lambda$ changes dynamically [147], the Universe goes to a temporary accelerated phase for $\lambda \lesssim 1$ and enters a decelerated phase for $\lambda \gg 1$. In other words, the present day acceleration is temporary, and the Universe enters a phase of decelerated expansion once again. This evolution of the Universe, therefore, avoids the future event horizon problem.

Introducing the same dimensionless variables as introduced in the last subsection, we can transform the required equations as

$$\begin{aligned} y' &= y\left[\Omega_{m,in} y^{-3} + \Omega_{r,in} y^{-4} + \frac{\Omega_{\phi,in}\sqrt{-w_{\phi,in}}\, e^{\frac{\phi_{in}}{\phi_a}(1-\psi)}}{\sqrt{1-\phi_{in}^2 H_{in}^2 \psi'^2}}\right]^{1/2}, \\ \psi'' &= \left(1-\phi_{in}^2 H_{in}^2 \psi'^2\right)\left[\frac{\phi_{in}/\phi_a}{\phi_{in}^2 H_{in}^2} - 3\psi'\frac{y'}{y}\right], \end{aligned} \tag{2.12}$$

We therefore have three model parameters $\phi_0 H_0$ , $\phi_0/\phi_a$ and $\dot{\phi}_0$ or $w_{\phi 0}$ to constrain. Apart from these parameters, there are cosmological parameters $\Omega_{m0}$ and $H_0$. In this case, the amplitude of potential can be calculated by the relation

$$\frac{8\pi G}{3H_0^2} V_a = \Omega_{\phi 0} e^{\phi_0/\phi_a} \sqrt{-w_{\phi 0}}, \tag{2.13}$$

Structure of these equations suggests that $-1 \leq w_{\phi 0} = \phi_0^2 H_0^2 \psi_0'^2 - 1 < 0$. For this potential, we also use the same initial conditions given in equation (2.9) and (2.10).

## 2.2 Results and Discussion

We use low redshift data sets of Baryon Acoustic Oscillations (BAO), Supernova Type Ia (SN-Ia) and direct measurements of Hubble parameter (H(z)) to find out the likelihood of the parameters. These data sets are described in section 1.6 of this thesis. We do the standard $\chi^2$ analysis to constrain parameters for the tachyon dark energy. Value of $\chi^2_{BAO}$ for the Baryon Acoustic Oscillation data is the sum of $\chi^2$ over all redshifts given in subsection 1.6.3. We calculated $\chi^2$ for DR12 data using the expression given in the equation (1.108). We employ the covariance matrix $C_{ij}$ taken from the online files of Alem et al. (2017) and Chi-Hsun et al. (2017). Value of $\chi^2$ for older BAO data (BAO data from 6dFGS, SDSS DR7 and WiggleZ), H(z) data and SN-Ia data is calculated using

$$\chi^2_{olderBAO/Hz/SN} = \sum_{i=1}^{N} \left( \frac{O_D(z_i) - O_M(z_i, \mathbf{p})}{\sigma_i} \right)^2, \tag{2.14}$$

Here $O_D(z_i)$ is the theoretical value of the observable at redshift $z_i$, and $O_M(z_i, \mathbf{p})$ is its value for model at redshift $z_i$ with the set of parameters $\mathbf{p}$. The quantity $\sigma_i$ is the error in the measurement of the observable $O_D(z_i)$. Here observable '$O$' is the acoustic parameter $A(z)$ for the older BAO data, Hubble parameter for the H(z) data and distance modulus $\mu(z)$ for the SN-Ia data. We then find the maximum of likelihood ($e^{-\chi^2_{tot}}$) of the parameter space by minimizing $\chi^2_{tot} = \chi^2_{BAO} + \chi^2_{Hz} + \chi^2_{SN}$.

### 2.2.1 Constraints on the Inverse Square Potential

As mentioned in section 2.1.1, we constrain three parameters, $\Omega_{m0}$, $w_{\phi 0}$ and $\phi_0 H_0$ for this potential. Since only the square of the quantity $\phi_0 H_0$ appears in the equa-

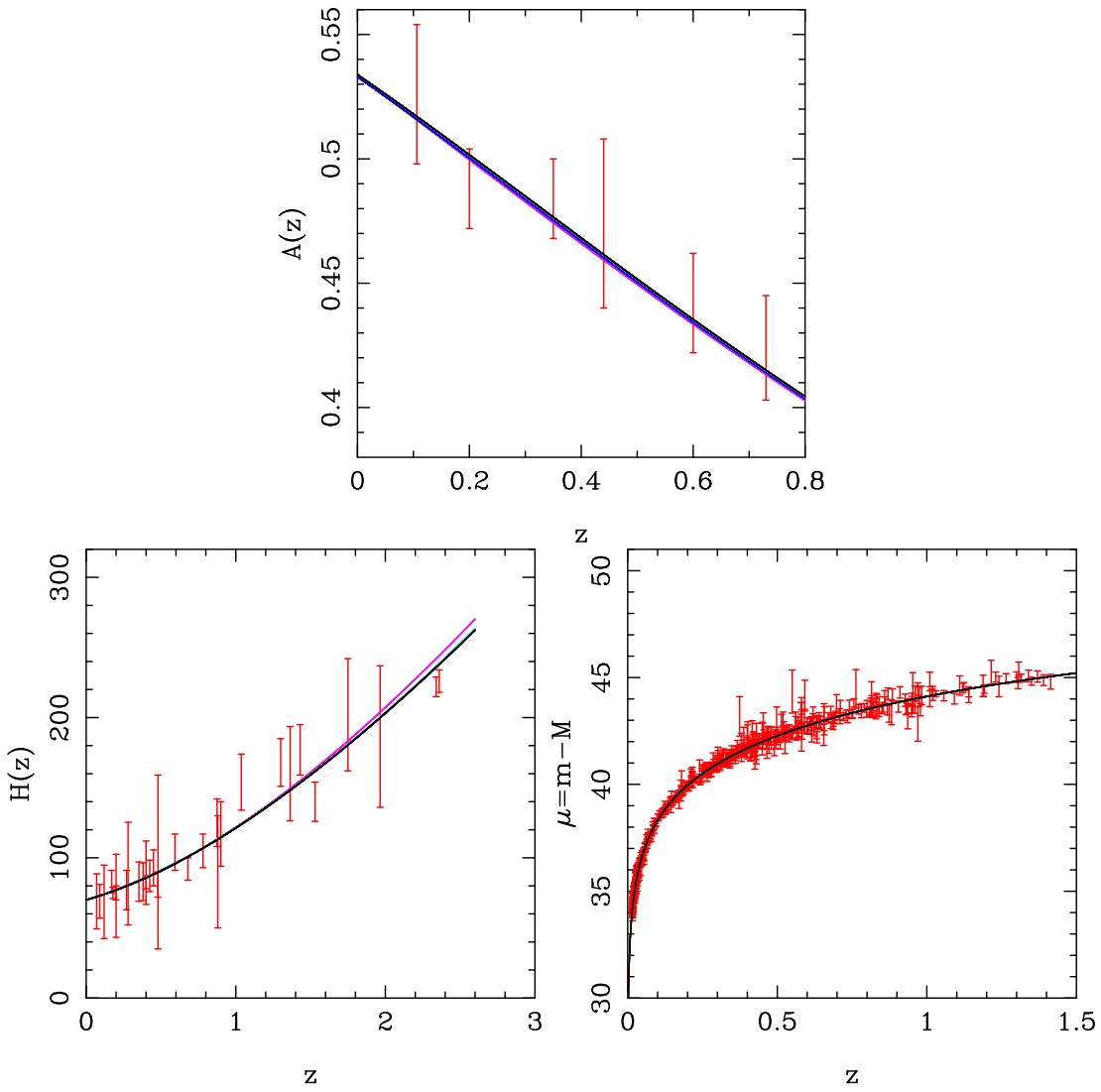


Figure 2.1: In this figure, the acoustic parameter $A(z)$, the Hubble parameter $H(z)$ and the distance modulus $\mu(z)$ are shown as functions of redshift $z$ for inverse square potential (2.2). The data points and error bars are taken from [108, 110, 123]. There are six very closely separated solid lines representing the model with inverse square potential in each plot for the values of the parameter $\phi_0 H_0 =$ 2.0, 3.0, 4.0, 5.0, 6.0 and 7.0. The values of other parameters $\Omega_{m0}$ and $w_{\phi 0}$ are the corresponding best fit values taken from each row of the table 2.1. There is a good agreement of the theoretical quantities with their observed values.

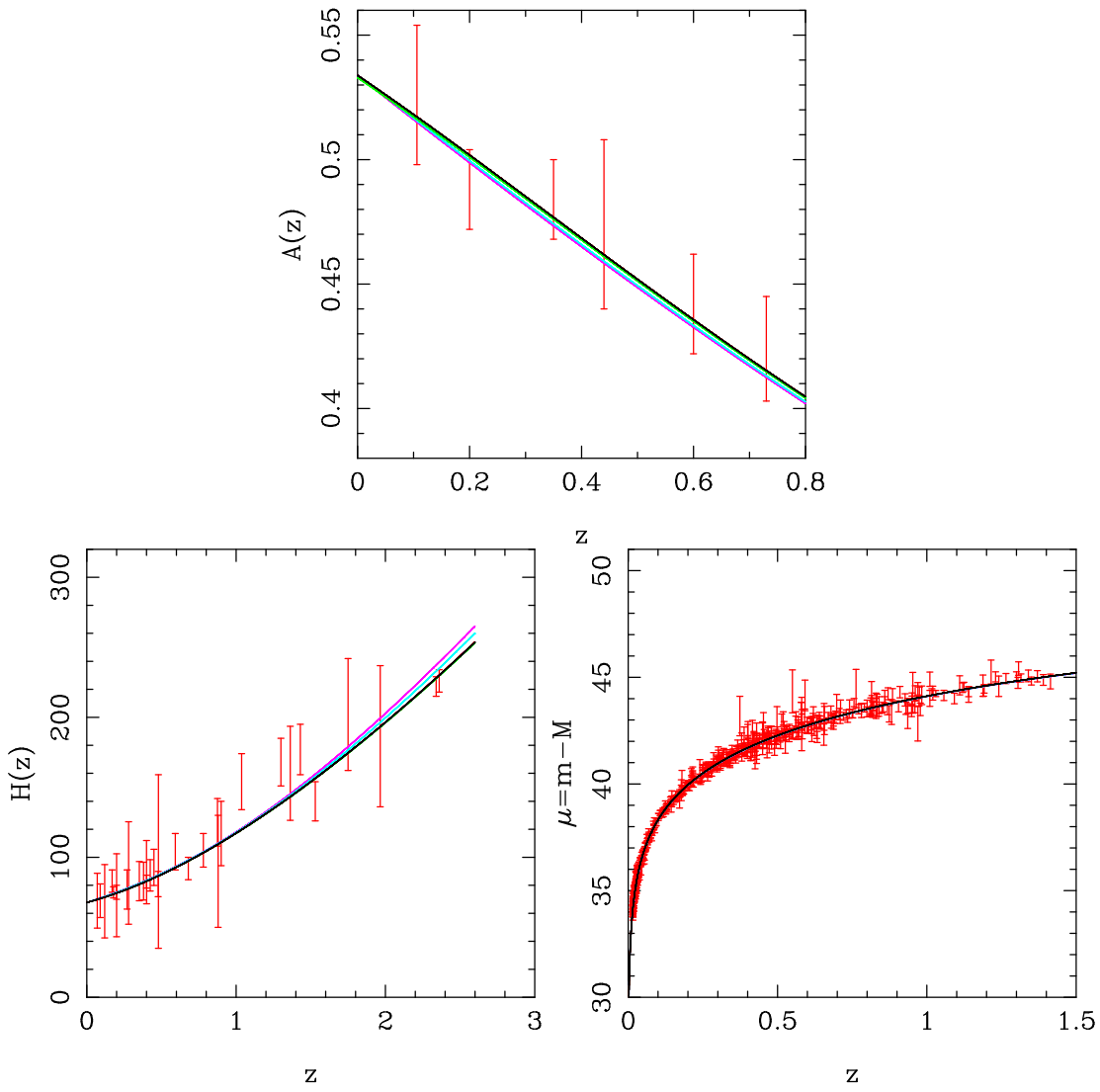


Figure 2.2: The figure shows plots of the acoustic parameter $A(z)$, the Hubble parameter $H(z)$ and the distance modulus $\mu(z)$ as a function of redshift $z$ for the exponential potential (2.11). The data points and error bars are taken from [108, 110, 123]. In each panel this figure too, there are six (theoretical) solid lines representing tachyon dark energy model with exponential potential for $\phi_0 H_0 =$ 0.08, 0.09, 0.1, 0.3, 0.5 and 0.7. We have fixed the parameter $\phi_0/\phi_a = 0.1$ and the values of other parameters $\Omega_{m0}$ and $w_{\phi 0}$ are the corresponding best fit values taken from each row of the table 2.2.

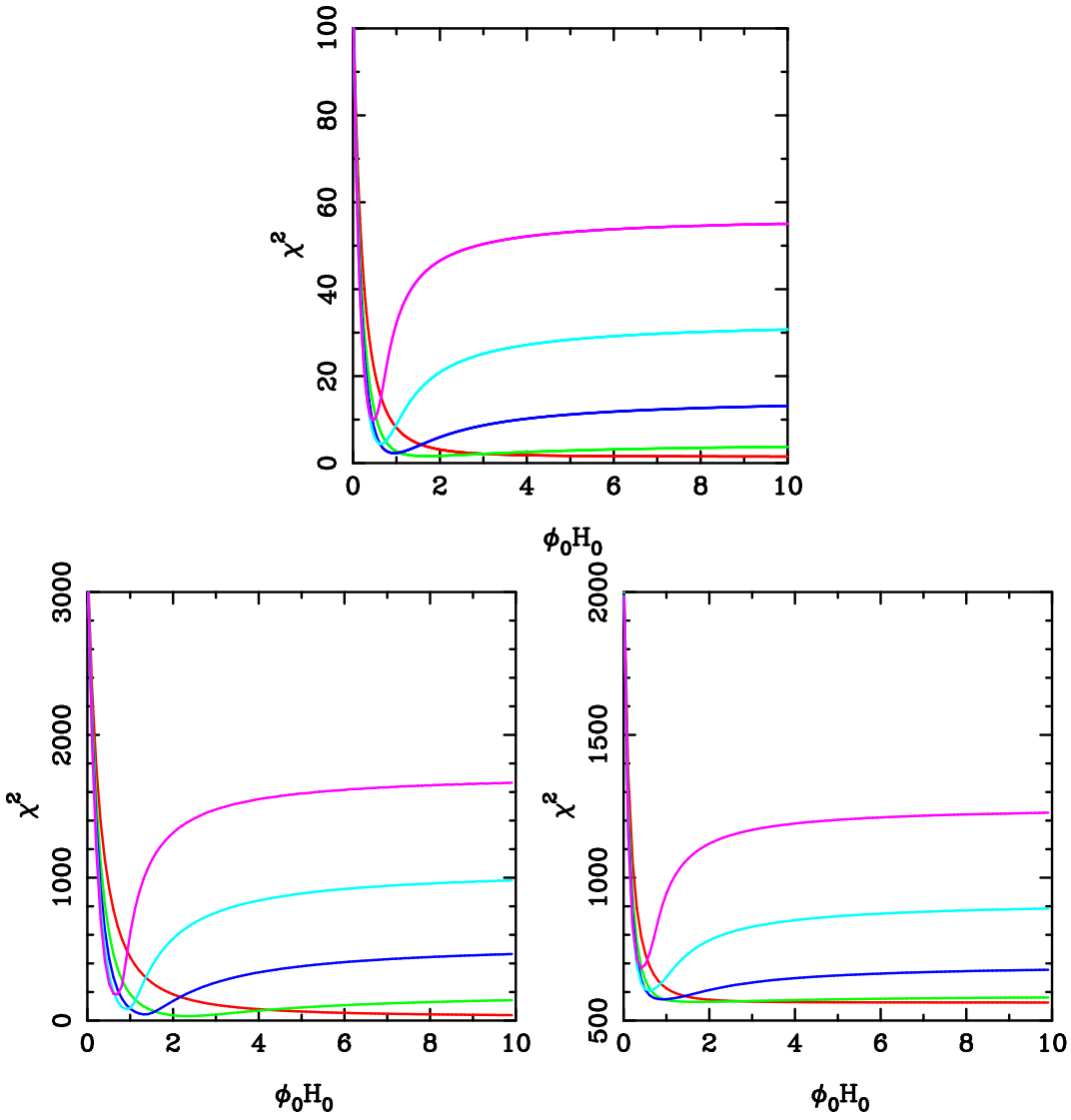


Figure 2.3: In this figure, we show $\chi^2$ as a function of the parameter $\phi_0 H_0$ for BAO data (top panel), $H(z)$ data (bottom left) and SN-Ia data (bottom right) respectively. Here, we have fixed $\Omega_{m0} = 0.285$, whereas the red, green, blue, sky-blue and pink lines represent the value of $w_{\phi 0}$ to be $-1.0$, $-0.95$, $-0.90$, $-0.85$ and $-0.80$ respectively.

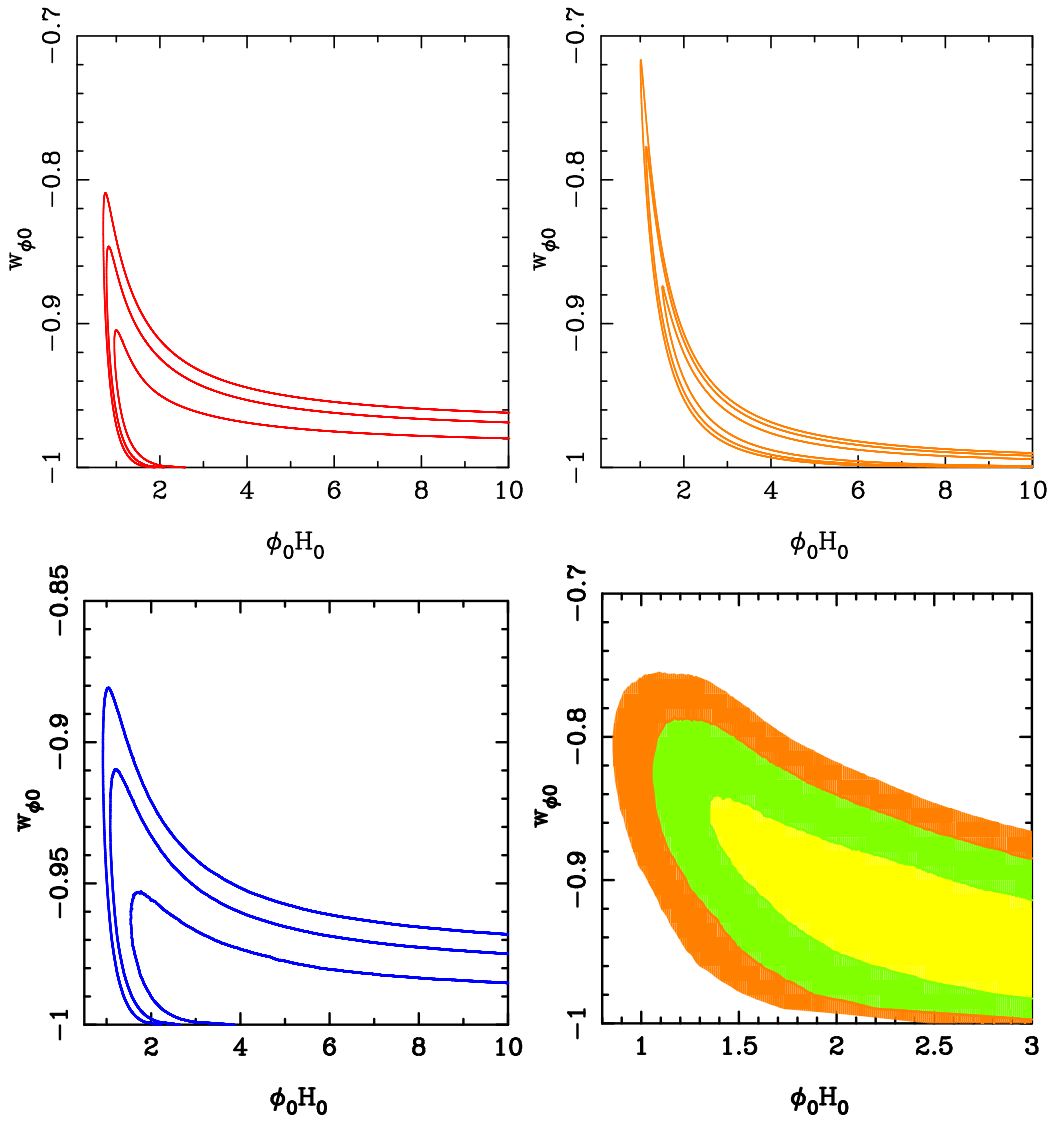


Figure 2.4: The figure shows $1\sigma$, $2\sigma$ and $3\sigma$ confidence contours between $w_{\phi 0}$ and $\phi_0 H_0$ for tachyon model with inverse square potential. Top left and right panels correspond to BAO data and $H(z)$ data, whereas bottom left panel corresponds to SN-Ia data for fixed value of present matter density parameter $\Omega_{m0} = 0.285$. In the bottom right panel, we show the marginalized confidence contours in the $w_{\phi 0}-\phi_0 H_0$ plane for combined data (BAO + H(z) + SN-Ia).

tions, we need to consider only one of the two, positive or negative branches. There is a degeneracy between parameters $w_{\phi 0}$ and $\phi_0 H_0$; these parameters are correlated.

In top panel of figure 2.1, we plot the acoustic parameter $A(z)$ obtained from the BAO data from 6dFGS, SDSS DR7 and WiggleZ [108]. In bottom left and right panels we have shown the Hubble parameter $H(z)$ and the distance modulus $\mu(z)$ as a function of $z$ respectively. Data points and error bars are as in [110, 123]. There are six (overlapping) theoretical solid lines in each of these plots representing inverse square potential (2.2). To draw these curves we have taken the best fit value of parameters $\phi_0 H_0$, $\Omega_{m0}$ and $w_{\phi 0}$ from each row of table 2.1. We can see that there is a good agreement of the theoretical curves with data.

The values of $\chi^2$ vs $\phi_0 H_0$ for $\Omega_{m0} = 0.285$ are plotted in figure 2.3. The five different colours represent different values of $w_{\phi 0}$ from $-1.0$ to $-0.80$ in the steps of 0.05. We can see that if $w_{\phi 0}$ is close to $-1.0$ (red and green curves) all larger value of $\phi_0 H_0$ are allowed. If we fix $w_{\phi 0}$ to a value away from $-1.0$, we can get a minimum in $\chi^2$ curves and fixing this parameter is equivalent to fixing $\dot{\phi}_0$ as $w_\phi = \dot{\phi}^2 - 1$. Since we are interested in constraining $\Omega_{m0}$ and $w_{\phi 0}$, we choose to fix $\phi_0 H_0$. Degeneracy between these parameters can also be seen in figure 2.4, where we have shown $1\sigma$, $2\sigma$ and $3\sigma$ contours in the $w_{\phi 0}$ - $\phi_0 H_0$ plane for the three datasets. After marginalizing over $\Omega_{m0}$, we find that $\phi_0 H_0 \geq 0.775$ at $3\sigma$ confidence level using combined data. The marginalized contours for combine data (BAO + Hz + SN-Ia) are shown in the bottom right panel of figure 2.4. It can be clearly seen that there is a bound on the lower value of $\phi_0 H_0$ but not on its upper value. We constrain the parameter space of $\Omega_{m0} - w_{\phi 0}$ and shown its variation with $\phi_0 H_0$ in figure 2.5.

For each of these contours, we have fixed the value of $\phi_0 H_0$. The most stringent constraints come from the BAO data, and combined constraints limit the parameter space to a very small range. Value of $\Omega_{m0}$ is well constrained by combined dataset at $0.285^{+0.023}_{-0.022}$ with $3\sigma$ confidence, and this remains at almost the same value with variation in parameter $\phi_0 H_0$. However, the constraint on $w_{\phi_0}$ depends on the value of $\phi_0 H_0$. As we increase the value of $\phi_0 H_0$, all the three datasets prefer a value of $w_{\phi 0}$ close to $-1$. In table 2.1 we have shown, the minimum value of $\chi^2$ for a fixed value of $\phi_0 H_0$ and the best fit value of parameters $\Omega_{m0}$ and $w_{\phi 0}$ with the $3\sigma$ confidence limit for combined data. We started with $\phi_0 H_0 = 2.0$ and increased its value in unit step. Here we can see that minimum value of $\chi^2$ saturates for a larger value of $\phi_0 H_0$, and so does the parameter $\Omega_{m0}$. In this background cosmological model, we can tune the parameter $\phi_0 H_0$ to be very close to $w_\phi = -1.0$. In the strict sense, it is not possible to constrain $\phi_0 H_0$ using these background data. A large

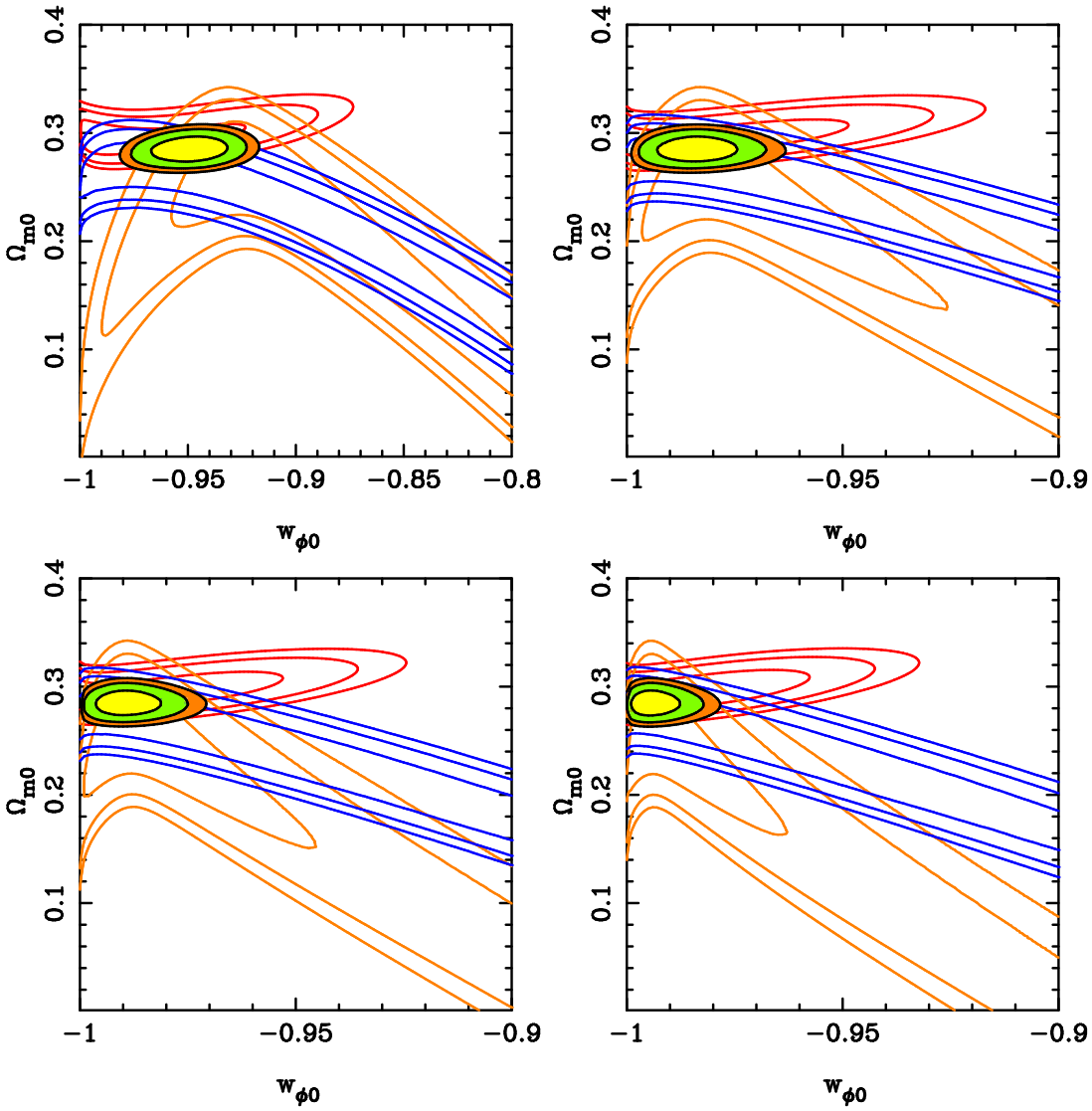


Figure 2.5: The plots show contours in the $\Omega_m - w_\phi$ plane, for constant $\phi_0 H_0$ for all the three and combined datasets for the inverse square potential. Contours in red, orange and blue are for BAO, $H(z)$ and SN-Ia data respectively. Black contours filled with colours represent combined constraints. The value of parameter $\phi_0 H_0 =$ 2.0, 4.0, 5.0 and 7.0 in the top left, top right, bottom left and bottom right panels respectively.

| $\phi_0 H_0$ | $\chi^2_{min}$ | $\Omega_{m0}$ | $w_{\phi 0}$ | $n$ |
|---|---|---|---|---|
| 2.0 | 596.145 | $0.285^{+0.023}_{-0.022}$ | $-0.950^{+0.033}_{-0.031}$ | [4.323,4.726] |
| 3.0 | 592.045 | $0.285^{+0.023}_{-0.021}$ | $-0.973^{+0.023}_{-0.022}$ | [9.445,10.250] |
| 4.0 | 590.944 | $0.284^{+0.024}_{-0.021}$ | $-0.984^{+0.021}_{-0.015}$ | [16.635,18.016] |
| 5.0 | 590.515 | $0.285^{+0.023}_{-0.022}$ | $-0.990^{+0.019}_{-0.009}$ | [25.906,27.959] |
| 6.0 | 590.335 | $0.285^{+0.023}_{-0.022}$ | $-0.993^{+0.017}_{-0.007}$ | [37.252,40.133] |
| 7.0 | 590.285 | $0.285^{+0.023}_{-0.022}$ | $-0.995^{+0.016}_{-0.005}$ | [50.659,54.504] |

Table 2.1: The table lists the best fit values of $\Omega_{m0}$ and $w_{\phi 0}$ along with their $3\sigma$ confidence range for different values of $\phi_0 H_0$ for inverse square potent for combined data (BAO + H(z) + SN-Ia). In the second column minimum value of corresponding $\chi^2_{min}$ have been shown. In the last column, we have shown the $3\sigma$ allowed range of '$n$', calculated from equation (2.7) considering $3\sigma$ confidence range of $\Omega_{m0}$ and $w_{\phi 0}$.

range of values of $\phi_0 H_0$ are acceptable as the background data only put a lower bound on its value. In the last column of table 2.1, we have shown the $3\sigma$ allowed range of '$n$' computed from the equation (2.7) considering the $3\sigma$ confidence range of $\Omega_{m0}$ and $w_{\phi 0}$. From equation (2.5), it is clear that the amplitude of the tachyon potential and constant '$q$' are proportional to the value of $\phi_0^2 H_0^2$, as can be seen in the equation (2.5). This is the reason, the allowed value of '$n$' also increases with it. Since the Universe expands like $a \propto t^n$ for a given '$n$', for a larger value of $\phi_0 H_0$ the accelerated expansion is faster in dark energy dominated era. We find that for this model, the transition redshift is between $0.61 \lesssim z_{acc} \lesssim 0.80$.

The evolution of the matter density parameter $\Omega_m(z)$(red curves) and the dark energy density parameter $\Omega_\phi(z)$(blue curves) are shown in the bottom panel of figure 2.9. We can see that even in the matter dominated era, dark energy contributes significantly to the energy budget. For smaller values of $\phi_0 H_0$, the contribution of dark energy, in the matter dominated era, is larger than it is for larger value of this

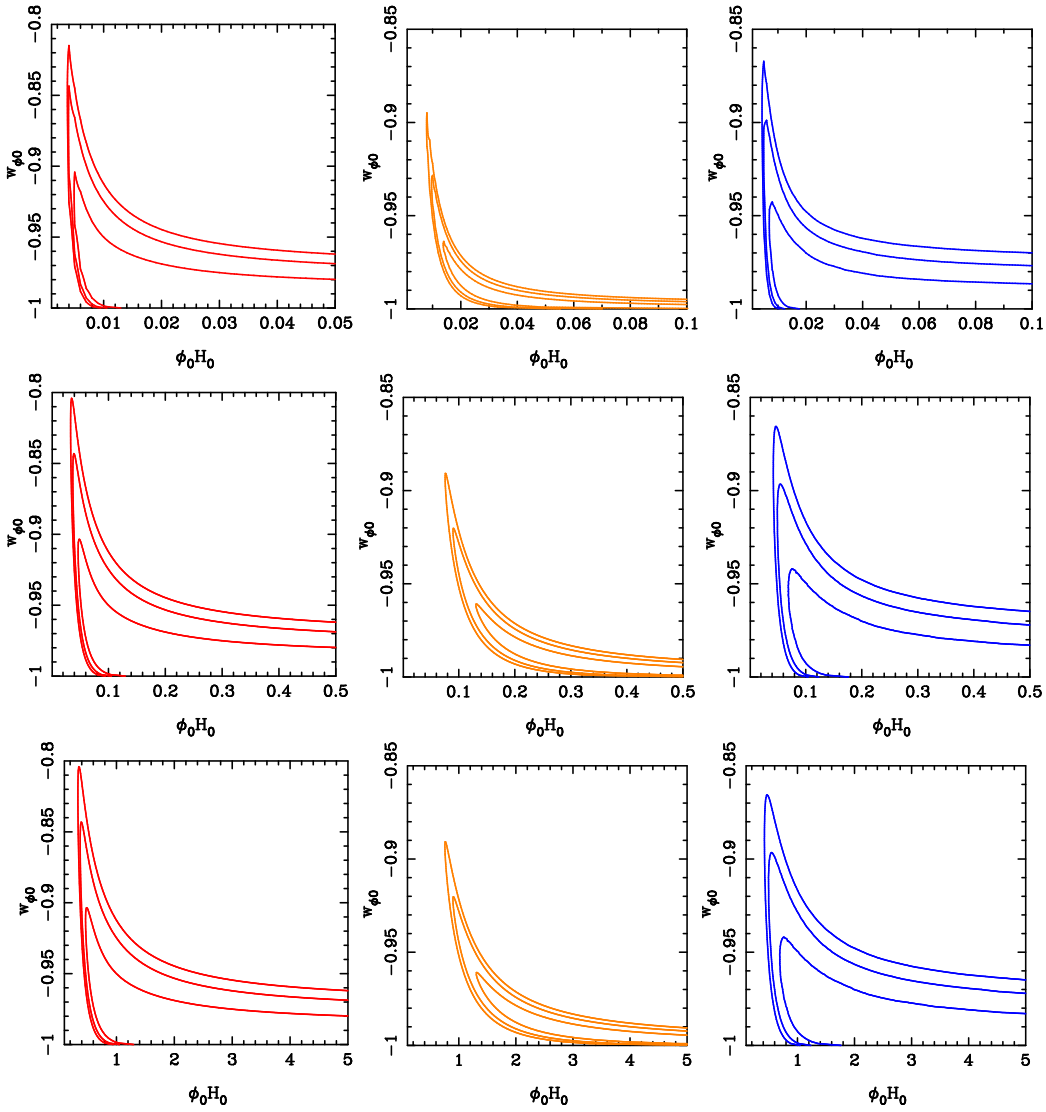


Figure 2.6: The figure shows $1\sigma$, $2\sigma$ and $3\sigma$ confidence contours on $w_{\phi 0} - \phi_0 H_0$ plane for exponential potential. Red, orange and blue colours represent BAO, Hz and SN-Ia data respectively. First, second and third rows are for $\phi_0/\phi_a = 0.01,\ 0.1$ and 1.0. For all these plots we have set $\Omega_{m0} = 0.285$.

parameter. Here it should be noted that parameter $\phi_0 H_0$ and $w_{\phi 0}$ are correlated. As we increase the value of $\phi_0 H_0$, matter approaches complete domination on the expansion dynamics at large redshift.

The evolution of the equation of state of the dark energy $w_\phi$ is shown in the top panel of the figure 2.9. In the matter dominated era and before it, the equation of state of tachyon dark energy is like that of dust. After that, it starts evolving and make a sharp transition towards smaller value than its present value $w_{\phi 0}$ then rises again. For a given value of $\phi_0 H_0$ it maintains a constant value in the future. For the larger values of $\phi_0 H_0$, this constant value for future evolution is closer to -1.0 as a larger value of $\phi_0 H_0$ prefers a cosmological constant like behaviour.

### 2.2.2 Constraints on the Exponential Potential

For the exponential potential, we need to constrain parameters $\phi_0 H_0, \phi_0/\phi_a, w_{\phi 0}$ and $\Omega_{m0}$. Rewriting the potential as $V = e^{ln(V_a)-\frac{\phi}{\phi_a}}$, we see that there is an explicit degeneracy between $V_a$ and $\phi_{in}$, i.e., a change in $V_a$ and the corresponding change in $\phi_{in}$ leads to the same $V_{in}$. Since we have replaced $V_a$ by the other parameters shown in equation (2.13), this degeneracy reflects in degeneracy between $\phi_0/\phi_a$ and $\phi_0 H_0$.

In figure 2.2 we show the agreement between data and theory with exponential potential (2.11). We plot the acoustic parameter $A(z)$, the Hubble parameter $H(z)$ and the distance modulus $\mu(z)$ as a function of redshift $z$ along with the data points and the error bars, taken from [108, 110, 123]. There are six overlapping theoretical curves in each of these plots representing the exponential potential. To draw these theoretical curves, we have taken the best fit values of the parameters $\phi_0 H_0$, $\Omega_{m0}$ and $w_{\phi 0}$ from each row of table 2.2.

To show the degeneracy mentioned above, we first plot the $1\sigma$, $2\sigma$ and $3\sigma$ contours in $w_{\phi 0} - \phi_0 H_0$ plane in figure 2.6. In these plots, we have fixed $\Omega_{m0} = 0.285$ and first, second and third row are for $\phi_0/\phi_a = 0.01,\ 0.1$ and $1.0$. We can see that all datasets (BAO, Hz and SN-Ia) have lower bound on $\phi_0 H_0$. In figure 2.7 we show marginalized confidence contours for combination of all the three data sets. We can see that the lower bound on the parameter $\phi_0 H_0$ depends on the value of $\phi_0/\phi_a$; for $\phi_0/\phi_a = 0.01$ we have $\phi_0 H_0 \gtrsim 4 \times 10^{-3}$, for $\phi_0/\phi_a = 0.1$ we have $\phi_0 H_0 \gtrsim 0.04$ and $\phi_0/\phi_a = 1.0$ we have $\phi_0 H_0 \gtrsim 0.41$. The lower bound on $\phi_0 H_0$ increases with $\phi_0/\phi_a$. We fix the parameter $\phi_0/\phi_a = 0.1$, and we do our analysis by keeping other parameters free. The analysis below is equally valid for any other value of this parameter if $\phi_0 H_0$ is adjusted accordingly or properly scaled.

We have shown constraints on $\Omega_{m0}$–$w_{\phi 0}$ plane in figure 2.8 for $\phi_0 H_0 = 0.08,\ 0.3,\ 0.5,$ and 0.9. Here we have fixed $\phi_0/\phi_a = 0.1$. The contours filled with three different colours represent result for the combination of datasets. The $3\sigma$ results for this model are shown in table 2.2. We started from $\phi_0 H_0 = 0.08$ as for smaller values, the value of $\chi^2_{min}$ increases sharply. We can see that for a smaller value of $\phi_0 H_0$ the three datasets are not in good agreement with each other and hence a large value of $\chi^2_{min}$. As we increase the value of this parameter, the value of $\chi^2_{min}$ decreases and the combined contours become smaller. The BAO data provides the tightest constraint on $\Omega_{m0}$ among all; this is consistent with previous studies [13, 14]. The value of this parameter is $\Omega_{m0} = 0.285^{+0.023}_{-0.022}$ with $3\sigma$ confidence for the combination of all three

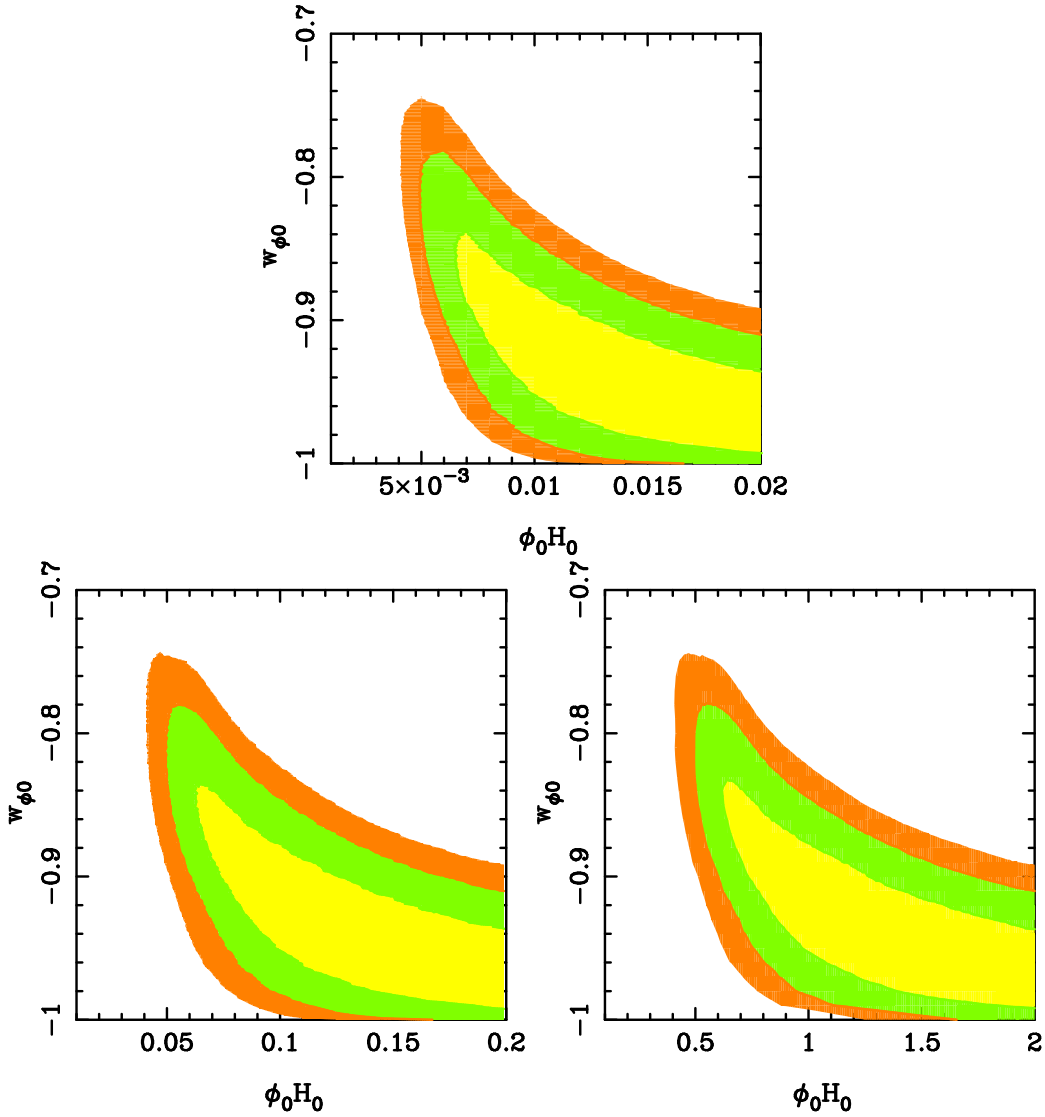


Figure 2.7: The figure shows the marginalized confidence contours on $w_{\phi 0} - \phi_0 H_0$ plane for combine data (BAO + Hz + SN-Ia) for exponential potential. The value of parameter $\phi_0/\phi_a =$ 0.01, 0.1 and 1.0 in the top, bottom left and bottom right panels respectively.

datasets, and it is almost a constant with variation in $\phi_0 H_0$. On the other hand, the value of $w_{\phi 0}$ depends on $\phi_0 H_0$. In the last column of table 2.2, we have shown the $3\sigma$ allowed range of the amplitude of the potential normalized to the present day value of the critical density $\rho_{cr} = \frac{3H_0^2}{8\pi G}$ using equation (2.13), considering $3\sigma$ confidence interval of $\Omega_{m0}$ and $w_{\phi 0}$. From equation (2.13) it is clear that the amplitude of the potential is not explicitly dependent on $\phi_0 H_0$ and as we have fixed $\phi_0/\phi_a = 0.1$; its value only depends on other parameters $\Omega_{m0}$ and $w_{\phi 0}$. Since the values of these parameters saturates with an increase in $\phi_0 H_0$, the amplitude of potential also approaches a fixed value unlike the case of tachyon model with inverse square potential.

The evolution of the equation of state parameter at different epochs in the expansion history of the Universe is shown in the top panel of figure 2.10. For a tachyon field with an exponential potential, the accelerating phase is sandwiched between two decelerating phases. In future, the Universe goes back to a decelerating phase and duration of the accelerating phase depends on the value of $\phi_0 H_0$ and $w_{\phi 0}$. In this plot, we can see that for a smaller value of $\phi_0 H_0$, this duration is small and the Universe goes to decelerating phase once again in relatively near future than it is for larger values of this parameter. The notable thing here is that parameters $\phi_0 H_0$ and $w_{\phi 0}$ are correlated and for small $\phi_0 H_0$ the best fit value of $w_{\phi 0}$ is large or away from -1.

We can see that in the matter dominated era, the dark energy behaves like a fluid and in the near past, it starts to deviate from $w_\phi = 0$ sharply. For a larger value of $\phi_0 H_0$, its deviation begins earlier. At first, it goes close to $-1$ depending on its present day value $w_{\phi 0}$ and then it rises away from $-1$. For a smaller value of $\phi_0 H_0$ it faster approach to a fluid like equation of state $w_\phi = 0$ and as it crosses the condition $w_\phi \leq -1/3$ for an accelerated expansion and the Universe goes to a decelerating phase once again. We have shown the evolution of density parameters $\Omega_m$(red curves) and $\Omega_\phi$(blue curves) with redshift in the panel at bottom of figure 2.10. In the matter dominated era, matter does not fully dominate the energy budget. Part of sub-dominated dark energy density parameter is large (solid line) for a smaller value of $\phi_0 H_0$ and as we increase the value of this parameter non-relativistic matter dominates the energy of the Universe completely.

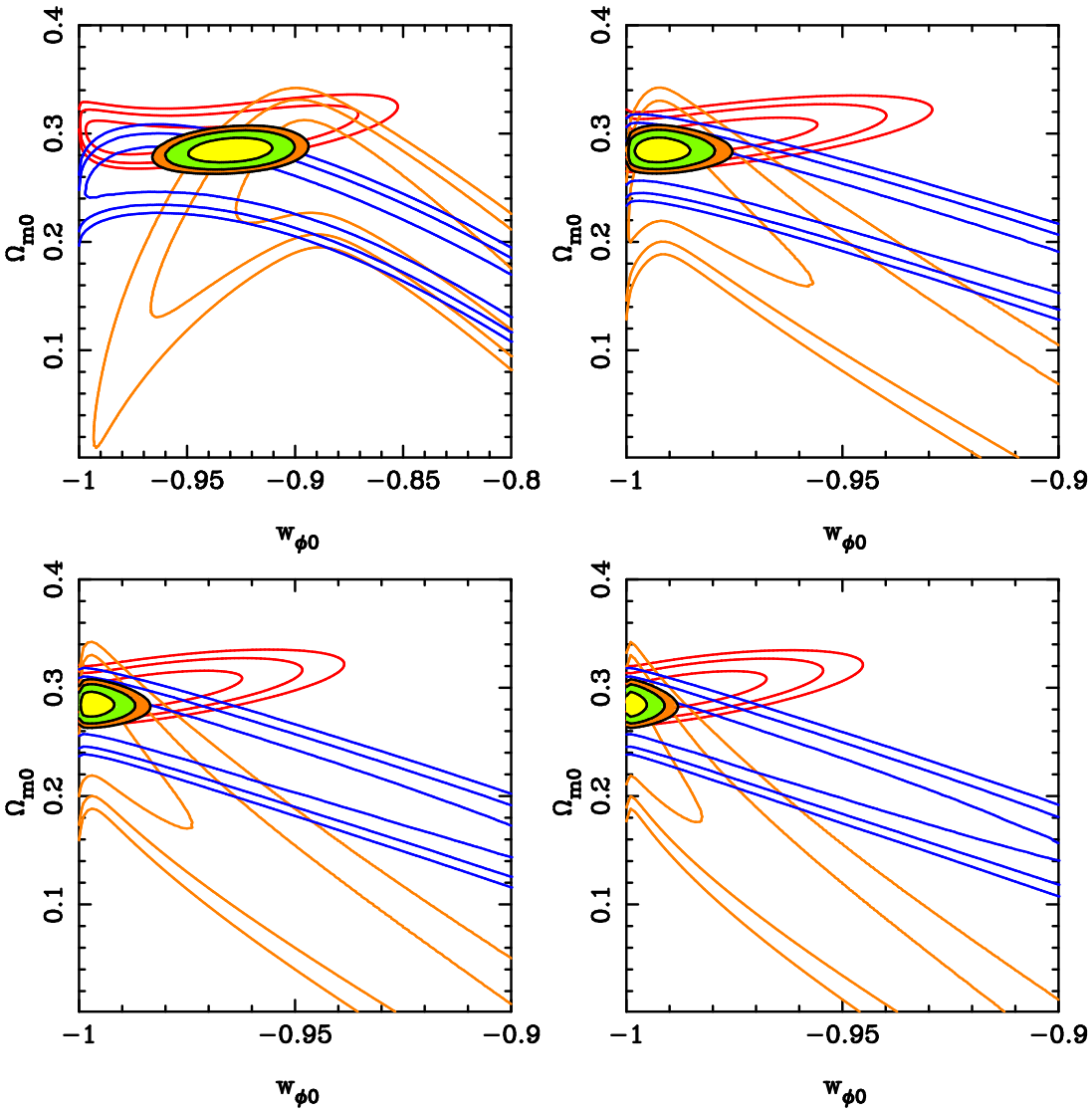


Figure 2.8: Contours in the $\Omega_{m0}$ - $w_{\phi 0}$ plane for a fixed value of $\phi_0/\phi_a = 0.1$ for the exponential potential. Top left and right panels correspond to $\phi_0 H_0 =$ 0.08 and 0.3 respectively, whereas bottom left and right panels are for $\phi_0 H_0 =$ 0.5 and 0.9 respectively. The red, orange and blue colours represent BAO, H(z) and SN-Ia data respectively. Black contours filled with colours represent combined constraints.

| $\phi_0 H_0$ | $\chi^2_{min}$ | $\Omega_{m0}$ | $w_{\phi 0}$ | $\frac{V_a}{\rho_{cr}}$ |
|---|---|---|---|---|
| 0.08 | 600.125 | $0.285^{+0.022}_{-0.022}$ | $-0.928^{+0.034}_{-0.038}$ | [0.724,0.801] |
| 0.10 | 595.862 | $0.285^{+0.023}_{-0.022}$ | $-0.949^{+0.030}_{-0.032}$ | [0.733,0.806] |
| 0.30 | 590.327 | $0.285^{+0.023}_{-0.022}$ | $-0.993^{+0.017}_{-0.007}$ | [0.756,0.815] |
| 0.50 | 590.136 | $0.284^{+0.024}_{-0.021}$ | $-0.997^{+0.013}_{-0.003}$ | [0.759,0.815] |
| 0.70 | 590.132 | $0.285^{+0.023}_{-0.022}$ | $-0.999^{+0.012}_{-0.001}$ | [0.760,0.815] |
| 0.90 | 590.061 | $0.285^{+0.023}_{-0.022}$ | $-0.999^{+0.011}_{-0.001}$ | [0.760,0.815] |

Table 2.2: Best fit values for $\Omega_{m0}$ and $w_{\phi 0}$ with $3\sigma$ confidence interval for the exponential potential for different values of $\phi_0 H_0$ for combine data (BAO + H(z) + SN-Ia) set. Here we have fixed the value of $\phi_0/\phi_a = 0.1$. In the last column, we have shown the range of amplitude of potential $V_a$ normalized by present critical density $\rho_{cr}$. It is calculated from equation (2.13) considering $3\sigma$ confidence range of $\Omega_{m0}$ and $w_{\phi 0}$.

## 2.3 Summary and Conclusions

In this work, we have constrained parameters of the tachyon dark energy model with an inverse square potential and an exponential potential. For this purpose, we have used the Baryon acoustic Oscillation data (from SDSS DR12, 6dFGS, SDSS DR7, WingleZ surveys), direct measurement of Hubble parameter (H(z)) data and Supernova-Ia Union 2.1 data. For the inverse square potential, we have three parameters $\phi_0 H_0$, $w_{\phi 0}$ and $\Omega_{m0}$. For the exponential potential, apart from these three, there is an extra parameter $\phi_0/\phi_a$. There is a lower bound on the parameter $\phi_0 H_0$, and all larger values are allowed. For the inverse square potential, $\phi_0 H_0 \geq 0.775$ at the $3\sigma$ confidence level. For the exponential potential, this value depends on $\phi_0/\phi_a$, and the lower bound on $\phi_0 H_0$ increases with increase in $\phi_0/\phi_a$. Using combined data of all three measurements, we find that the present day matter density parameter is constrained to the values $\Omega_{m0} = 0.285^{+0.023}_{-0.022}$ at the $3\sigma$ confidence

for both the potentials and it remains almost same with variation in $\phi_0 H_0$. This value of $\Omega_{m0}$ for the tachyon model is less than the value of this parameter for a flat $\Lambda CDM$ model as determined by current observations, e.g., $\Omega_{m0} = 0.295 \pm 0.034$ ( at 68% confidence using JLA data [150]), $\Omega_{m0} = 0.3089 \pm 0.0062$ (at 68% confidence obtained from CMB-TT,TE,EE+ low-P + lensing+ BAO+JLA+ $H_0$ data [66]), $\Omega_{m0} = 0.311 \pm 0.0056$ (at 68% confidence obtained from CMB-TT,TE,EE+ low-P + lensing+ BAO data [60]) and $\Omega_{m0} = 0.310 \pm 0.005$ (at 95% confidence using BAO DR12 + SN-Ia data [2]). The value of $\Omega_{m0}$ for tachyon model is in agreement with its value for flat $\Lambda CDM$ model constrained by the JLA data within $1\sigma$. There is a tension with constraints from Planck and BAO DR12 data.

The value of $w_{\phi 0}$ depends on $\phi_0 H_0$. For a smaller value of $\phi_0 H_0$, the equation of state parameter $w_{\phi 0}$ has a larger value and as its value increases, $w_{\phi 0}$ approaches $-1$. A large range of $\phi_0 H_0$ is allowed by the background data. The parameter $\phi_0 H_0$ need to be tuned to obtain the value of the equation of state parameter $w_{\phi 0}$ which is supported by observations ($w_{\phi 0} = -1.006 \pm 0.045$ [66] and $w_{\phi 0} = -1.03 \pm 0.03$ [60] ). This tuning is not as severe as the fine-tuning problem in $\Lambda CDM$ model. This parameter is constrained from below to a value closer to unity, and there is no upper bound. Therefore the tuning of this parameter is not severe. The potentials, we have used in this paper, have also been extensively used for canonical scalar field (quintessence field) model of dark energy and similar results have been found [18, 19, 151, 152, 153, 154]. Specially, tracker solutions of quintessence model are able to solve the fine-tuning problem, and thawing or freezing model ameliorate this problem [18, 19, 152, 154]. In [151], it has been shown that for the potential $V(\phi) \propto \phi^{-n}$, with $n < 5$, the solutions do not have a fine-tuning problem and a large range of initial conditions provide acceptable solutions. Similar results have also been shown in [18, 19, 152, 155] for inverse power law potentials. Exponential potential have been studied in [18, 155, 156, 157] for quintessence model and it is found to ameliorate the fine-tuning problem. In our study, tachyon models with both the potentials generate acceptable solution for large range of parameters. On the other hand, for larger value of $\phi_0 H_0$, it is able to mimic the cosmological constant like equation of state at present. Hence, in the light of current observational data, tachyon model is an interesting and important alternate model of dark energy.

We have also studied the evolution of the phases of expansion, the density parameters and the equation of state of dark energy with redshift. We find the transition redshift to be in the range $0.61 \lesssim z_{ac} \lesssim 0.80$. For the exponential potential, the duration of the acceleration phase depends on $\phi_0 H_0$ and $w_{\phi 0}$ (as these parameters are correlated). For a smaller value of $\phi_0 H_0$ this duration is small. The equation of

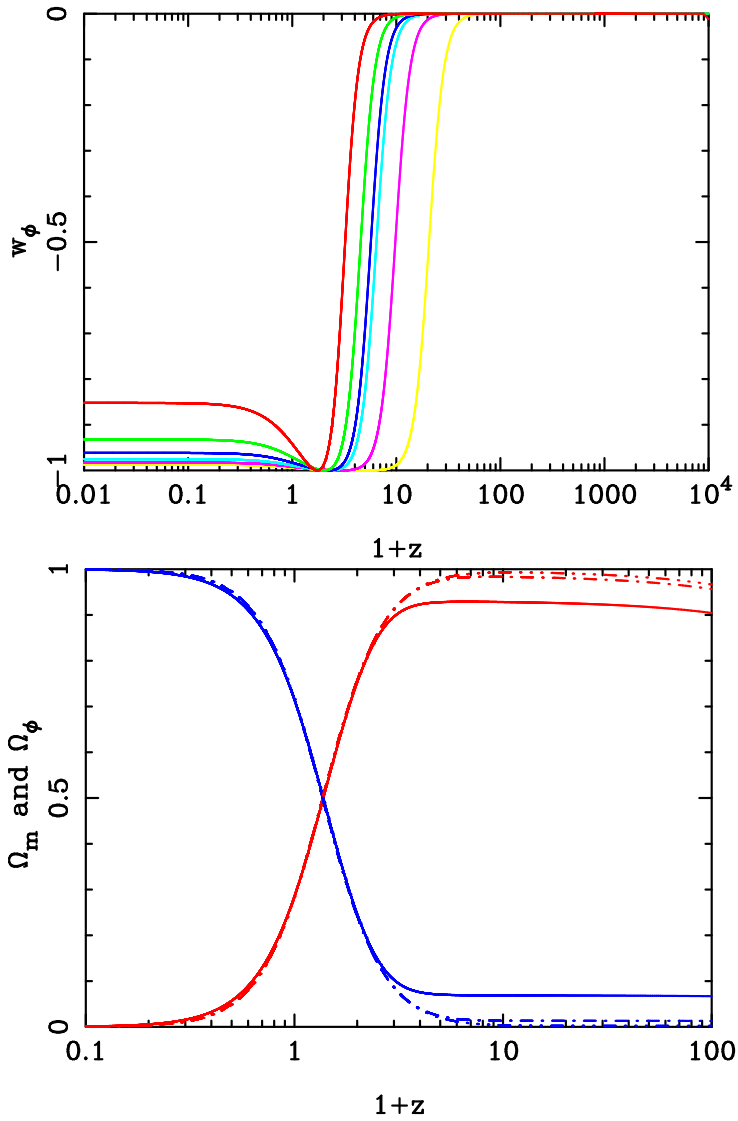


Figure 2.9: The plot on the top shows the evolution of equation of state $w_\phi$ with redshift for inverse square potential. Red, green, blue, sky-blue, yellow and pink colours represent value of $\phi_0 H_0 =$ 2.0, 3.0, 4.0, 5.0, 6.0 and 7.0. The plot on the bottom shows the evolution of $\Omega_m$ (red curves) and $\Omega_\phi$ (blue curves) with redshift. The solid, dash-dot and dashed-dot-dot-dot lines represent the value of $\phi_0 H_0 =$ 2.0, 4.0 and 6.0 respectively. The value of parameter $w_{\phi 0}$ and $\Omega_{m0}$ are the best fit values taken from table 2.1 for the corresponding value of $\phi_0 H_0$.

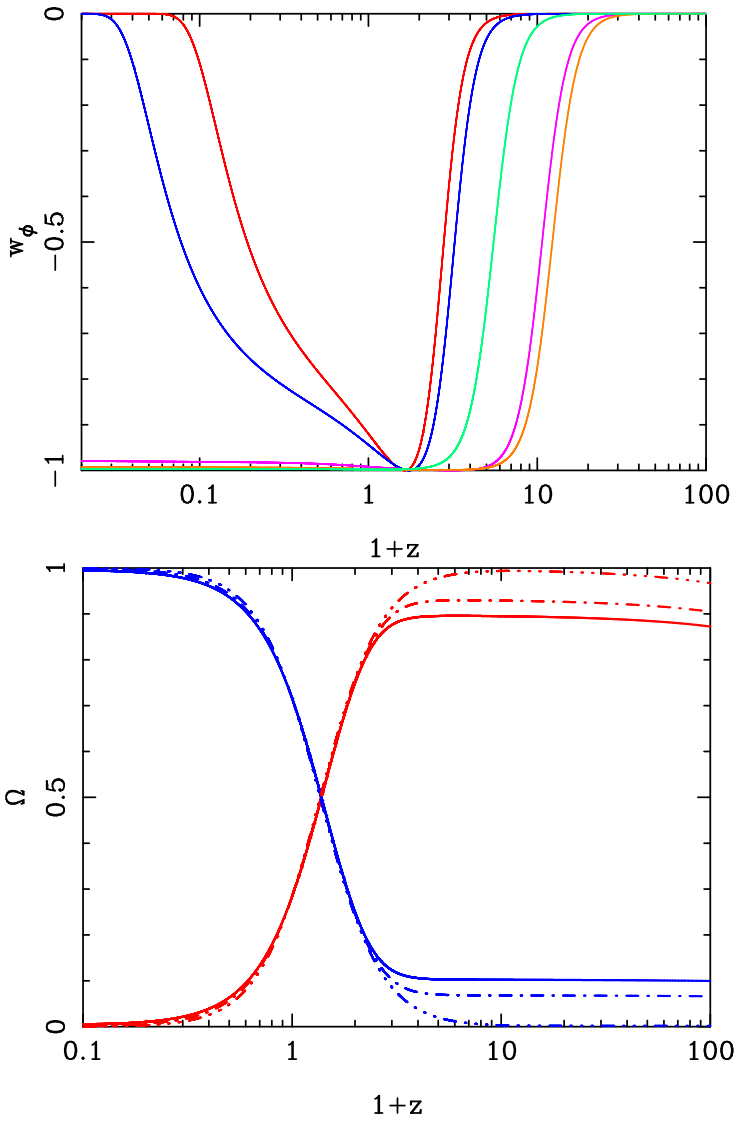


Figure 2.10: The plot on the top shows the evolution of equation of state $w_\phi$ with redshift for exponential potential. Red, blue, sky blue, orange and gray lines represent $\phi_0 H_0 =$ 0.08, 0.1, 0.3, 0.5 and 0.7. The plot on the bottom shows evolution of $\Omega_m$ (red curves) and $\Omega_\phi$ (blue curves) with redshift are shown. Solid, dash-dot and dashed-dot-dot-dot lines represent $\phi_0 H_0 =$ 0.08, 0.1 and 0.3. Parameter $\Omega_{m0}$ and $w_{\phi 0}$ are the best fit values taken from table 2.2 for the corresponding value of $\phi_0 H_0$. Parameter $\phi_0/\phi_a = 0.1$.

state of the tachyon dark energy, in the matter dominated and earlier phases, is dust like ($w_\phi = 0$). It then makes a sharp transition to that of a cosmological constant as dark energy domination begins. The value of the equation of state parameter rises again to match its present day value $w_{\phi 0}$. For the inverse square potential, it approached a constant value depending on the values of $\phi_0 H_0$ and $w_{\phi 0}$. For exponential potential, it rises towards $w_\phi = 0$, and as it becomes greater than $-1/3$, the Universe once again goes to a decelerating expansion phase. For tachyon dark energy, matter does not fully dominate the energy budget. However, as we increase the value of parameter $\phi_0 H_0$, it approaches full domination as the equation of state approaches like that of a cosmological constant.

The constraints obtained here are stringent, and there is a clear preference for models which are close to the cosmological constant model. A specific set of parameters can be ruled out in a given set of models whereas current data cannot completely distinguish between different models and does not fully rule out any. The range of the combined constraints on the matter density parameter and the equation of state parameter are determined largely by the BAO data and by the supernova data respectively. While the Hubble parameter data constrains the parameters well, the allowed range is larger than that allowed by other observations. This is possibly due to the fact that the Hubble parameter measurement data is a compilation of measurements with different methods and accompanies measurements of different cosmological quantities. The constraints on the parameters are stringent and more data, and further studies in perturbations in tachyon dark energy are likely to break the degeneracy between different models which are allowed by pure distance measurements.

# Chapter 3

# Perturbations in Tachyon Dark Energy

**This chapter is adapted from following published article**

Avinash Singh, H. K. Jassal, Manabendra Sharma, *Perturbations in tachyon dark energy and their effect on matter clustering*, Journal of Cosmology and Astroparticle Physics **05** (2020)008. arXiv:1907.13309

In this chapter, we analyze the dynamics and nature of tachyon perturbations and their effect on the evolution of matter perturbations. We begin with a homogeneous tachyon scalar field and allow allow perturbations in it, as the matter clustering grows with time. In this analysis, we the consider same two tachyon potentials, an inverse square potential and an exponential potential (which are introduced in chapter 2) for study of background cosmology. We solve linearized Einstein's equations in 'the Newtonian conformal gauge' to study the formation of linear oder structure in the Universe. The clustering of dark energy is a scale dependent phenomena, it is higher at larger scales, opposite to the matter clustering which is higher at smaller scales. Dark energy perturbations are insignificant with respect to matter clustering at sub-Hubble scales, and dark energy can be considered homogeneous. At Hubble and super-Hubble scales, dark energy perturbations are significant when compared with the matter perturbation. However, as the present value of the equation of state $w_{\phi 0} \to -1$, it can be considered homogeneous and this model coincides with the $\Lambda CDM$ model.

We also study the linear growth rate $f(z)$ of matter clustering for these models

and compare our theoretical computation with the redshift space distortion (RSD) data. We find that initially, in matter dominated era, the growth rate is higher for tachyon model than it is for $\Lambda CDM$ model, but in dark energy dominated era the situation is opposite to this. This makes tachyon model a better alternate to fit growth rate data. We use the 'Gold-2017' RSD data compiled and tabulated in [9] with some additional data from [143]. The growth rate measurements from RSD provide the value of $f\sigma_8(z)$, where $\sigma_8(z)$ is the root mean square fluctuation in the matter power spectrum in a sphere of radius 8 $h^{-1}Mpc$. In [9], it has been shown that there is a tension of $> 3\sigma$ between Gold-2017 and Planck-2015 data for $\Lambda CDM$ model. We find that this tension continues to exist between the RSD data we use and Planck-2018 data for $\Lambda CDM$ model. We show that, for tachyon models, this tension is reduced when equation of state parameter $w_{\phi 0}$ is larger than -1 and dark energy is allowed to get perturbed.

Perturbations in the tachyon scalar field and the matter part are introduced in section 3.1. We derive the required sets of dynamical equations here using the Newtonian conformal gauge. We discus our numerical approach in section 3.2 and transform the required set of equations into dimensionless form. The results of our analysis are discussed in section 3.3. Finally, we summarize our results in section 3.4.

## 3.1 Perturbation in the Tachyon Scalar Field

We consider the perturbed FLRW metric to study the perturbations in matter and in the scalar field. If there are no anisotropic components in the spatial part of energy-momentum tensor, i.e., $T^i_j = 0$ for $i \neq j$, then in longitudinal gauge the perturbations can be described by a line element of the form

$$ds^2 = -(1+2\Phi)dt^2 + a^2(t)(1-2\Phi)[dx^2 + dy^2 + dz^2], \tag{3.1}$$

where $\Phi$ is the scalar perturbation. In the Newtonian limit, the metric perturbation $\Phi$ represents the effective gravitational potential. The dynamical equation for this scalar perturbation $\Phi$ can be derived by solving perturbed Einstein's equation $\delta G^\mu_\nu = 8\pi G \delta T^\mu_\nu$. Here, the perturbed energy-momentum tensor $\delta T^\mu_\nu$ consists of two parts, one for the matter component $\delta T^\mu_{\nu_{(matter)}}$ and other for the scalar field $\delta T^\mu_{\nu_{(\phi)}}$. We consider matter as a perfect fluid with energy-momentum tensor

$$T^\mu_{\nu_{(matter)}} = (\rho + p)u^\mu u_\nu + p g^\mu_\nu. \tag{3.2}$$

Here $\rho$, $p$ and $u^\mu$ are energy density, pressure and four velocity respectively. The perturbations in the matter field are defined by

$$\begin{aligned} \rho(t,\vec{x}) &= \bar{\rho}(t) + \delta\rho(t,\vec{x}), \\ p(t,\vec{x}) &= \bar{p}(t) + \delta p(t,\vec{x}), \\ u^\mu &= \bar{u}^\mu + \delta u^\mu, \end{aligned} \tag{3.3}$$

where $\bar{u}^\mu = \{1,0,0,0\}$, $\bar{\rho}(t)$ and $\bar{p}(t)$ are the average values of their respective quantities and $\delta u^\mu$ is the peculiar velocity. Substituting these values in equation (3.2), the components of the perturbed energy-momentum tensor of matter are

$$\begin{aligned} \delta T^0_0 &= -\delta\rho, \\ \delta T^i_0 &= (\bar{\rho} + \bar{p})\delta u^i, \\ \delta T^i_j &= \delta p \delta^i_j. \end{aligned} \tag{3.4}$$

The energy-momentum tensor for the tachyon field can be derived from

$$T^\mu_{\nu(\phi)} = \frac{V(\phi)\partial^\mu\phi\,\partial_\nu\phi}{\sqrt{1+g^{\alpha\beta}\partial_\alpha\phi\,\partial_\beta\phi}} + L_\phi g^\mu_\nu, \tag{3.5}$$

where for tachyon scalar field the Lagrangian $L_\phi$ is given by equation (1.50). We define the perturbation in the scalar field as

$$\phi(t,\vec{x}) = \bar{\phi}(t) + \delta\phi(t,\vec{x}). \tag{3.6}$$

Here $\bar{\phi}(t)$ is the average background field. Using equation (3.5) with the metric element of longitudinal gauge from equation (3.1), components of perturbed energy-momentum tensor for tachyon scalar field can be calculated:

$$\begin{aligned} \delta T^0_0 &= -\delta\rho_\phi = -\frac{\left(\frac{\partial V}{\partial\phi}\right)_{\bar{\phi}}\delta\phi}{\sqrt{1-\dot{\bar{\phi}}^2}} + \frac{1}{2}\frac{V(\bar{\phi})}{\sqrt{1-\dot{\bar{\phi}}^2}}\left(\frac{2\Phi\dot{\bar{\phi}}^2 - 2\dot{\bar{\phi}}\dot{\delta\phi}}{1-\dot{\bar{\phi}}^2}\right), \\ \delta T^i_j &= \delta p_\phi \delta^i_j = -V(\bar{\phi})\sqrt{1-\dot{\bar{\phi}}^2}\left(\frac{\Phi\dot{\bar{\phi}}^2 - \dot{\delta\phi}\dot{\bar{\phi}}}{1-\dot{\bar{\phi}}^2}\right)\delta^i_j - \left(\frac{\partial V}{\partial\phi}\right)_{\bar{\phi}}\delta\phi\sqrt{1-\dot{\bar{\phi}}^2}\,\delta^i_j, \\ \delta T^0_i &= (\rho_\phi + p_\phi)\delta u_i = \frac{V(\bar{\phi})}{\sqrt{1-\dot{\bar{\phi}}^2}}\dot{\bar{\phi}}\delta\phi_{,i}. \end{aligned} \tag{3.7}$$

We can now solve perturbed Einstein's equation $\delta G^{\mu}_{\nu} = 8\pi G \delta T^{\mu}_{\nu}$; where the perturbed energy-momentum tensor are given by equations (3.2) and (3.5). Components of the perturbed Einstein tensor $\delta G^{\mu}_{\nu}$ can be calculated using line element (3.1). We retain the terms in the solution of perturbed Einstein's equations up to first (or linear) order in all perturbed quantities. We then transform these linearized Einstein equations into the Fourier space or the $k-$ space, where the perturbed quantities of both the spaces are related by the equation

$$A(\vec{x}, t) = \int d^3k A(\vec{k}, t) e^{i\vec{k}.\vec{x}}. \tag{3.8}$$

Here, $\vec{k}$ is the wave vector.

In longitudinal gauge, the Fourier transformed Einstein's equations are given by

$$3\frac{\dot{a}^2}{a^2}\Phi + 3\frac{\dot{a}}{a}\dot{\Phi} + \frac{k^2\Phi}{a^2} = -4\pi G\left[\delta\rho_m + \delta\rho_\phi\right], \tag{3.9}$$

$$\ddot{\Phi} + 4\frac{\dot{a}}{a}\dot{\Phi} + \left(2\frac{\ddot{a}}{a} + \frac{\dot{a}^2}{a^2}\right)\Phi = 4\pi G\left[-V(\bar{\phi})\sqrt{1-\dot{\bar{\phi}}^2}\left(\frac{\Phi\dot{\bar{\phi}}^2 - \dot{\delta\phi}\dot{\bar{\phi}}}{1-\dot{\bar{\phi}}^2}\right) - \left(\frac{\partial V}{\partial\phi}\right)_{\bar{\phi}}\delta\phi\sqrt{1-\dot{\bar{\phi}}^2}\right], \tag{3.10}$$

$$\dot{\Phi} + \frac{\dot{a}}{a}\Phi = 4\pi G\left(\bar{\rho}a^{-3}v_m + \frac{V(\bar{\phi})}{\sqrt{1-\dot{\bar{\phi}}^2}}\dot{\bar{\phi}}\delta\phi_{,i}\right), \tag{3.11}$$

where $v_m$ represents the potential for the matter peculiar velocity, i.e., $\delta u_i = \nabla_i v_m$. Here although we have used the same symbol for quantities $\Phi, \delta\phi, \delta\rho_m$ and $v_m$, as they are in real physical space, they represent the Fourier components of respective quantities in $k^{th}$ mode of perturbation. The wave number is given by $k = 2\pi/\lambda_p$, where $\lambda_p$ is the comoving length of the perturbation. Therefore, the Einstein's equations given above represent the evolution of the $k^{th}$ mode of perturbations. Equation (3.10) is the dynamical equation for metric perturbation $\Phi$. Since matter is pressureless, the dynamics of metric perturbation $\Phi$ is driven only by perturbation in the scalar field. Here, in these equations, there are two unknown perturbed quantities, $\Phi$ and $\delta\phi$. Once these two are determined, then other perturbed quantities like $\delta\rho_m$ and $v_m$ can be calculated from equation (3.9) and (3.11). The dynamical equation for the perturbed tachyon scalar field $\delta\phi$ can be derived by solving the Euler-Lagrangian equation using the Lagrangian function (1.50) for the perturbed

scalar field, and in the Fourier space for $k^{th}$ mode, it is given by

$$\frac{\ddot{\delta\phi}}{(1-\dot{\bar{\phi}}^2)}+\left[3H+\frac{2\dot{\bar{\phi}}\ddot{\bar{\phi}}}{(1-\dot{\bar{\phi}}^2)^2}\right]\dot{\delta\phi}+\left[3H\dot{\bar{\phi}}\frac{V'}{V}+\frac{k^2}{a^2}+\frac{\ddot{\bar{\phi}}}{(1-\dot{\bar{\phi}}^2)}\left(\frac{V'}{V}\right)+\frac{V''}{V}\right]\delta\phi$$

$$-\left[12H\dot{\bar{\phi}}+\frac{2(2+\dot{\bar{\phi}}^2)\ddot{\bar{\phi}}}{(1-\dot{\bar{\phi}}^2)}+\frac{2V'}{V}+\frac{2\dot{\bar{\phi}}^4\ddot{\bar{\phi}}}{(1-\dot{\bar{\phi}}^2)^2}\right]\Phi+\frac{3\dot{\bar{\phi}}^3-4\dot{\bar{\phi}}}{(1-\dot{\bar{\phi}}^2)}\dot{\Phi}=0, \tag{3.12}$$

where the prime represents the derivative with respect to the background scalar field $\bar{\phi}$. The coupled equations (3.10) and (3.12) form a closed system of equations. Solving these equations together with the background equations, we can find the quantities $\Phi$ and $\delta\phi$ and then the respective fractional density contrasts $\delta=\delta\rho/\bar{\rho}$ of $k^{th}$ mode for matter and tachyon scalar field can be computed from the following equations

$$\delta_\phi=\frac{V'(\bar{\phi})}{V(\bar{\phi})}\delta\phi-\left(\frac{\Phi\dot{\bar{\phi}}^2-\dot{\bar{\phi}}\dot{\delta\phi}}{1-\dot{\phi}^2}\right),$$

$$\delta_m=-\frac{1}{4\pi G\rho_m a^{-3}}\left[3\frac{\dot{a}^2}{a^2}\Phi+3\frac{\dot{a}}{a}\dot{\Phi}+\frac{k^2\Phi}{a^2}\right]-\frac{1}{\rho_m a^{-3}}\left[\frac{V'(\bar{\phi})\delta\phi}{\sqrt{1-\dot{\bar{\phi}}^2}}-\frac{V(\bar{\phi})}{\sqrt{1-\dot{\bar{\phi}}^2}}\left(\frac{\Phi\dot{\bar{\phi}}^2-\dot{\bar{\phi}}\dot{\delta\phi}}{1-\dot{\phi}^2}\right)\right]$$

$$=-\frac{1}{4\pi G\rho_m a^{-3}}\left[3\frac{\dot{a}^2}{a^2}\Phi+3\frac{\dot{a}}{a}\dot{\Phi}+\frac{k^2\Phi}{a^2}\right]-\frac{\delta_\phi}{\rho_m a^{-3}}\frac{V(\bar{\phi})}{\sqrt{1-\dot{\bar{\phi}}^2}}. \tag{3.13}$$

To calculate matter density contrast $\delta_m=\delta\rho_m/\rho_m$ we have used equation (3.9). We can see from the above equations that the density contrasts of matter and dark energy are coupled with each other.

The growth of structure, quantified by the linear growth function $D_m^+$, defined as

$$D_m^+=\frac{\delta_m}{\delta_{m0}}, \tag{3.14}$$

The quantity $\delta_{m0}$ is the present value of matter density contrast, and the growth rate, defined as

$$f=\frac{d\ ln\ \delta}{d\ ln\ a}. \tag{3.15}$$

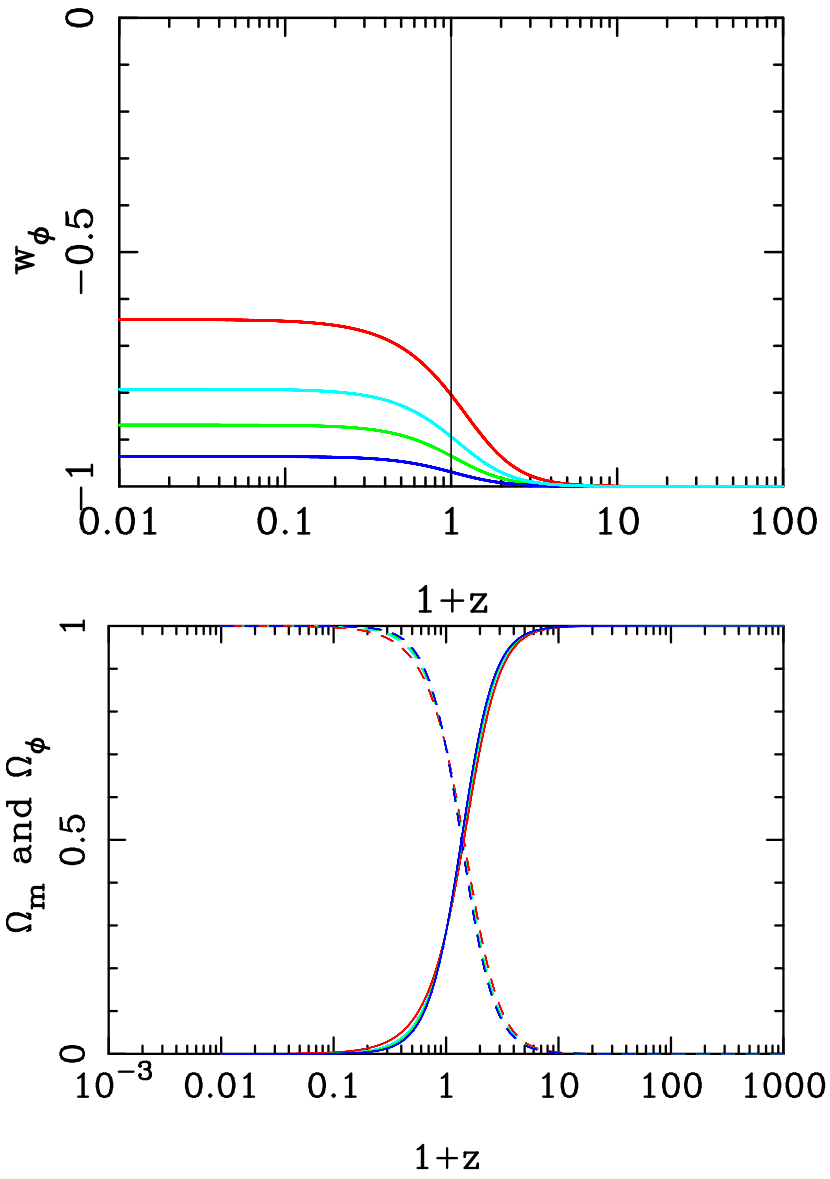


Figure 3.1: The plots on the top shows the evolution of the equation of state parameter of dark energy and the plot on the bottom shows the evolution of the density parameters for inverse square potential. Red, sky-blue, green and blue colours represent $\phi_{in}H_0 =$ 1.0, 1.5, 2.0 and 3.0. In the bottom panel, the solid line is for $\Omega_m$ and the dashed line is for $\Omega_\phi$. Parameters $C_n$ and $V_a/\rho_{cr}$ are tuned for each value of $\phi_{in}H_0$ to get $\Omega_{m0} = 0.285$.

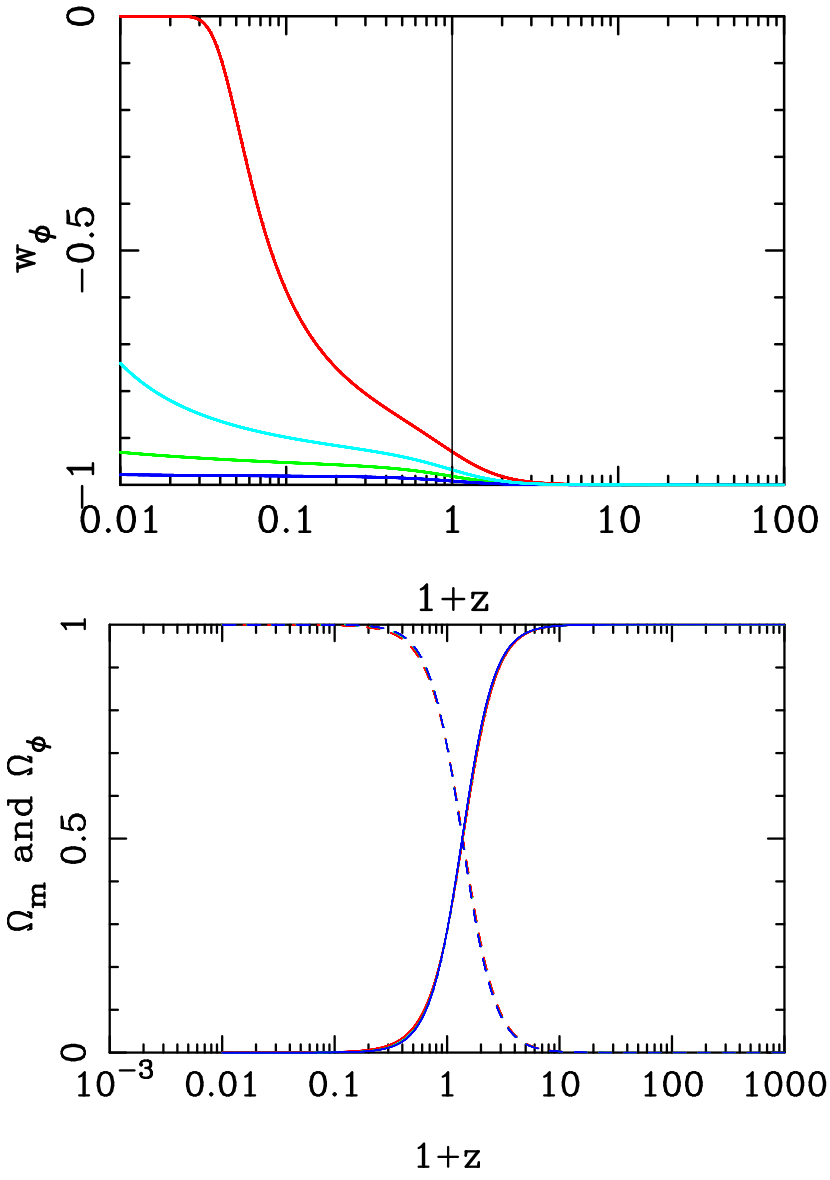


Figure 3.2: The plots on the top shows the evolution of the equation of state parameter of dark energy and the plot on the bottom shows the evolution of the density parameters for exponential potential. Colour and line scheme as well as the values of parameters are same as described in figurer 3.1.

## 3.2 Numerical Approach and Methodology

To solve for $a$, $\phi$, $\Phi$ and $\delta\phi$, we need four equations. We choose two background equations, first of the Friedmann equations (2.1) and the dynamical equation of scalar field (1.52). The third equation is the dynamical equation of the perturbed scalar field, equation (3.12) and the fourth one is the dynamical equation for the metric perturbation, the second equation of Einstein's equations (3.10). We rewrite these equations in the dimensionless form by introducing the following variables

$$x = tH_0,\ \ y = \frac{a}{a_{in}},\ \ \psi = \frac{\phi}{\phi_{in}},\ \ \Phi_N = \frac{\Phi}{\Phi_{in}},\ \ \delta\psi = \frac{\delta\phi}{\Phi_{in}\phi_{in}}, \tag{3.16}$$

to above equations to solve them. Derivatives are defined with respect to x as

$$y' = \frac{dy}{dx},\ \ \psi' = \frac{d\psi}{dx},\ \ \Phi_N' = \frac{d\Phi_N}{dx}. \tag{3.17}$$

### 3.2.1 Dimensionless Equations for the Inverse Square Potential

In terms of the above dimensionless variables (3.16), the background equations (2.1) and (1.52) with inverse square potential (2.2), take the form

$$y' = y\left[\Omega_{m_{in}} y^{-3} + \frac{\frac{2n}{3}(1-\frac{2}{3n})^{1/2}\psi^{-2}}{\phi_{in}^2 H_0^2\sqrt{1-\phi_{in}^2 H_0^2\psi'^2}}\right]^{1/2}, \tag{3.18}$$

$$\psi'' = \left(1-\phi_{in}^2 H_0^2\psi'^2\right)\left[\frac{2}{\phi_{in}^2 H_0^2\psi} - 3\frac{y'}{y}\psi'\right], \tag{3.19}$$

where $\Omega_{m_{in}}$ can be linked to the present matter density parameter $\Omega_{m0}$ using the relation

$$\Omega_m = \frac{\Omega_{m0}}{(H/H_0)^2}\left(\frac{a}{a_0}\right)^{-3}. \tag{3.20}$$

Here, $a_0$ is the present day value of the scale factor. To solve the above background equations, we need values of the parameters $\Omega_{m_{in}}$, $C_n$, and $\phi_{in}H_0$. Here $C_n = \frac{2n}{3}(1-\frac{2}{3n})^{1/2}$ is the amplitude of the potential.

Using the variables defined in equation (3.16), with inverse square potential (2.2), the dynamical equation for metric perturbation $\Phi$, equation (3.10), and the dynam-

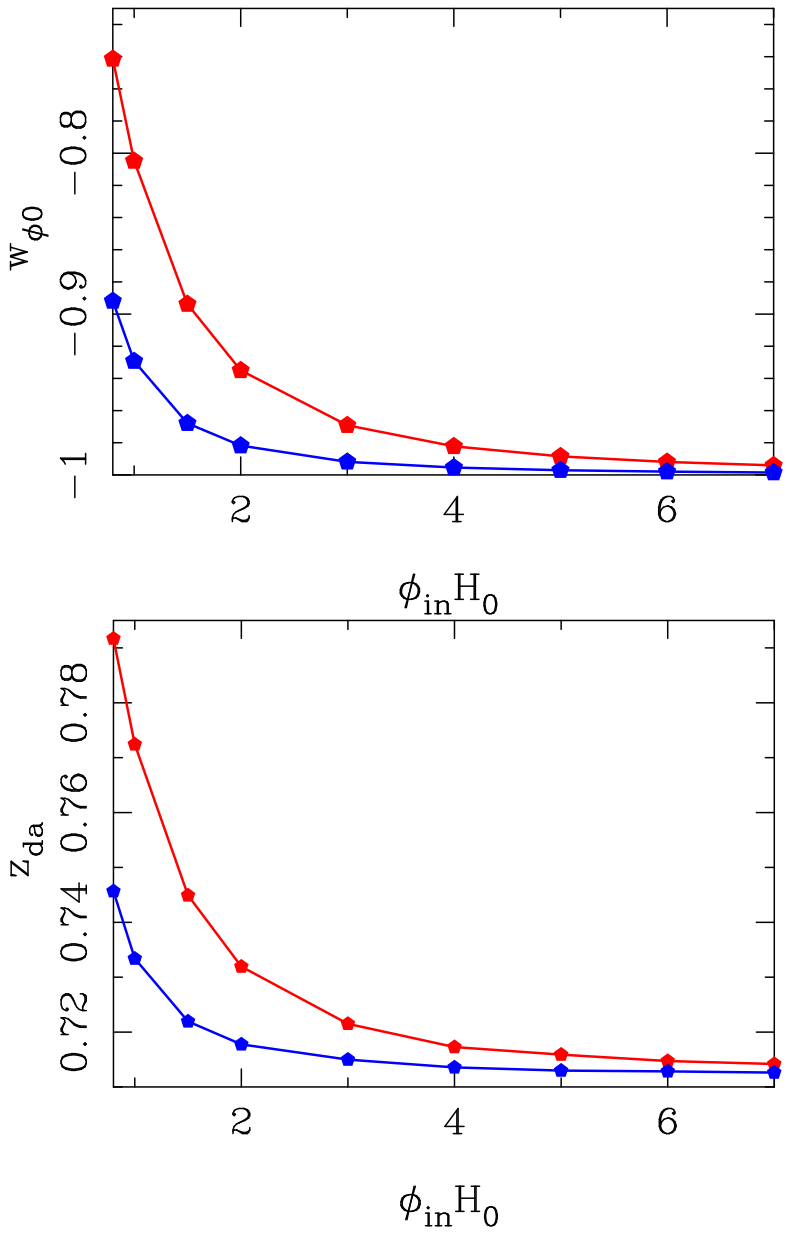


Figure 3.3: In this figure we show the dependence of the present day value of the equation of state parameter, $w_{\phi 0}$ (plot on the top), and the deceleration to acceleration transition redshift, $z_{dz}$ (in the bottom panel) on $\phi_{in}H_0$. The red curve is for inverse square potential and blue cure is for the exponential potential. The values of $C_n$ and $V_a/\rho_{cr}$ are the same as in 3.1.

ical equation of perturbed scalar field $\delta\phi$, equation (3.12) takes the form

$$\Phi_N'' + 4\frac{y'}{y}\Phi_N' + \left\{2\frac{y''}{y} + \left(\frac{y'}{y}\right)^2\right\}\Phi_N$$

$$= n\left(1-\frac{2}{3n}\right)^{1/2}\left[\frac{2\delta\psi}{\phi_{in}^2 H_0^2\psi^3}\sqrt{1-\phi_{in}^2H_0^2\psi'^2} - \frac{\Phi_N\psi'^2 - \psi'\delta\psi'}{\psi^2\sqrt{1-\phi_{in}^2H_0^2\psi'^2}}\right], \tag{3.21}$$

$$\frac{\delta\psi''}{\left(1-\phi_{in}^2H_0^2\psi'^2\right)} + \left[3\frac{y'}{y} + \frac{2\phi_{in}^2H_0^2\psi'\psi''}{\left(1-\phi_{in}^2H_0^2\psi'^2\right)^2}\right]\delta\psi'$$

$$+\left[-6\frac{y'}{y}\frac{\psi'}{\psi} + \frac{k^2}{a_{in}^2H_0^2y^2} - \frac{2\psi''}{\psi\left(1-\phi_{in}^2H_0^2\psi'^2\right)} + \frac{6}{\phi_{in}^2H_0^2\psi^2}\right]\delta\psi$$

$$-\left[12\frac{y'}{y}\psi' + \frac{2\left(2+\phi_{in}^2H_0^2\psi'^2\right)\psi''}{\left(1-\phi_{in}^2H_0^2\psi'^2\right)} - \frac{4}{\phi_{in}^2H_0^2\psi} + \frac{2\phi_{in}^4H_0^4\psi'^4\psi''}{\left(1-\phi_{in}^2H_0^2\psi'^2\right)^2}\right]\Phi_N$$

$$+\left[\frac{3\phi_{in}^2H_0^2\psi'^3 - 4\psi'}{\left(1-\phi_{in}^2H_0^2\psi'^2\right)}\right]\Phi_N' = 0. \tag{3.22}$$

On solving the perturbation equations along with the background using the above initial conditions, we can find the values of $\Phi_N$ and $\delta\psi$ as a functions of redshift or scale factor. Subsequently, the values of density parameters can be calculated using equations

$$\frac{\delta_\phi}{\Phi_{in}} = -2\frac{\delta\psi}{\psi} - \phi_{in}^2H_0^2\left(\frac{\psi'^2\Phi_N - \psi'\delta\psi'}{1-\phi_{in}^2H_0^2\psi'^2}\right),$$

$$\frac{\delta_m}{\Phi_{in}} = \frac{-2}{\Omega_{m_{in}}y^{-3}}\left[\frac{y'^2}{y^2}\Phi_N + \frac{y'}{y}\Phi_N' + \frac{k^2/H_0^2}{2a_{in}^2y^2}\Phi_N\right] - \frac{\delta_\phi/\Phi_{in}}{\Omega_{m_{in}}y^{-3}}\frac{\frac{2n}{3}(1-2/3n)^{1/2}\psi^{-2}}{\phi_{in}^2H_0^2\sqrt{1-\phi_{in}^2H_0^2\psi'^2}}. \tag{3.23}$$

To derive the above equations we have substituted dimensionless variables defined in equation (3.16) to equation (3.13).

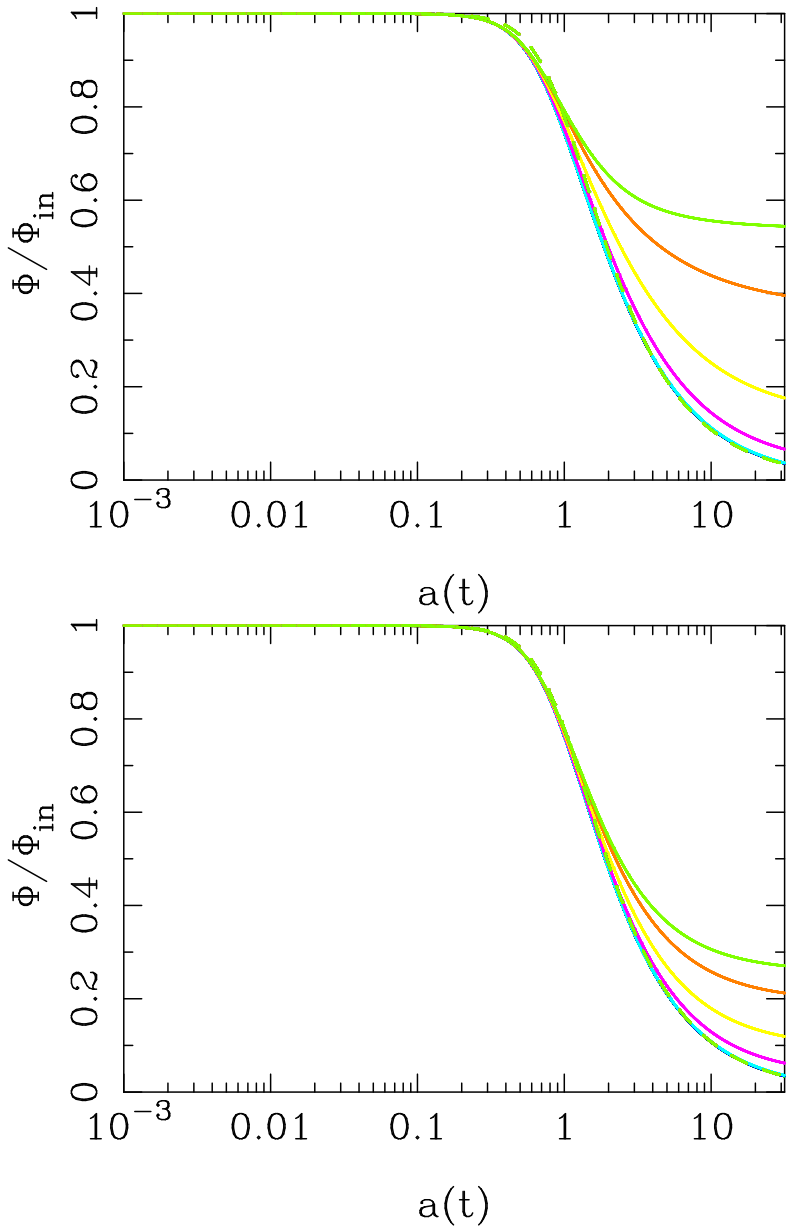


Figure 3.4: The evolution of gravitational potential with scale factor. Solid lines correspond to tachyon with inverse square potential whereas the dashed lines are for $\Lambda CDM$ model. The plots on the top and the bottom correspond to $\phi_{in}H_0 = 1.0$ and $\phi_{in}H_0 = 2.0$ respectively. We set the value of present day matter density parameter $\Omega_{m0} = 0.285$. The red, green, blue, sky-blue, pink, yellow, orange and light-green colours represents the scales of perturbation $\lambda_p =$ 50, 100, 500, 1000, 5000, 10000, 20000 and 50000 $Mpc$ respectively.

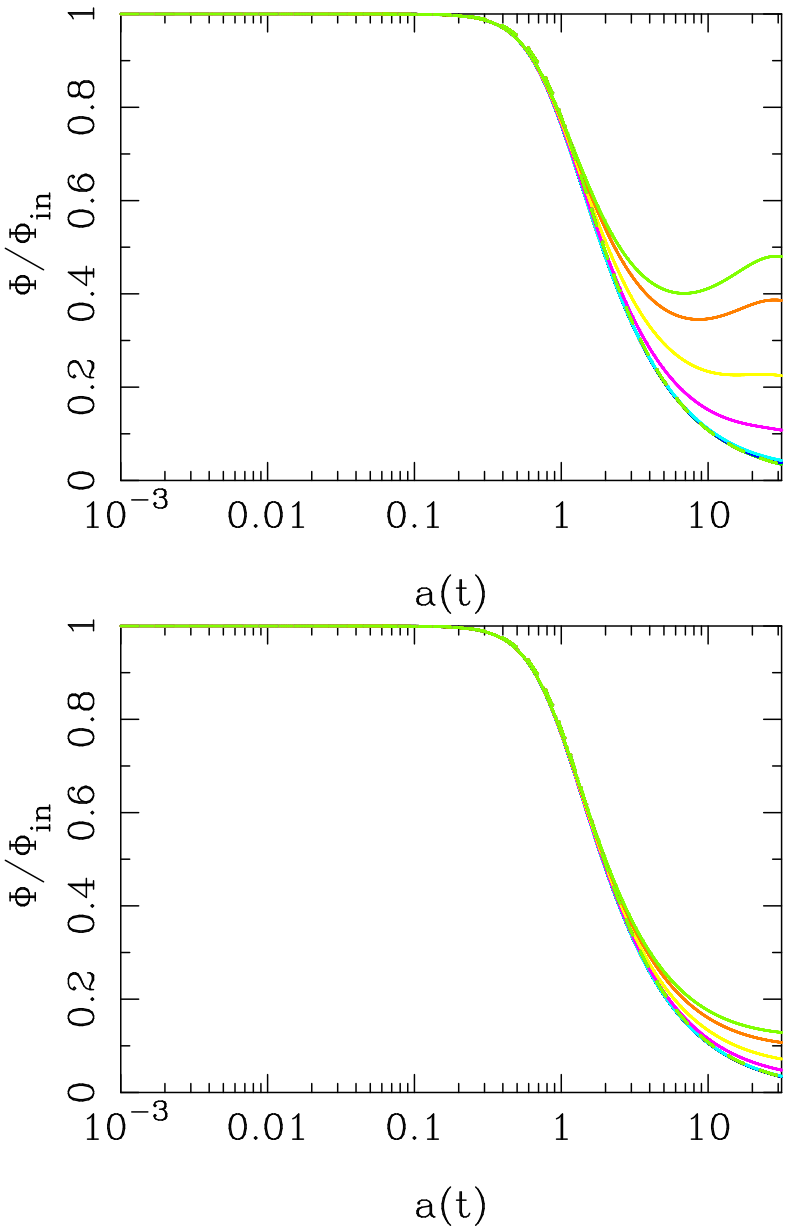


Figure 3.5: The evolution of gravitational potential with scale factor. Here, solid lines correspond to tachyon model with exponential potential, whereas dashed lines are for $\Lambda CDM$ model. The plots on the top and the bottom correspond to $\phi_{in}H_0 =$ 1.0 and 2.0 respectively. The value of other parameter and colour scheme is same as in the figure 3.4.

### 3.2.2 Dimensionless Equations for the Exponential Potential

In terms of the variables defined in equation (3.16), the background equations for exponential potential (2.11) can be written as

$$y' = y\left[\Omega_{m_{in}} y^{-3} + \frac{\frac{V_a}{\rho_{cr}} e^{-\frac{\phi_{in}}{\phi_a}\psi}}{\sqrt{1-\phi_{in}^2 H_0^2 \psi'^2}}\right]^{1/2}, \tag{3.24}$$

$$\psi'' = \left(1-\phi_{in}^2 H_0^2 \psi'^2\right)\left[\frac{\phi_{in}/\phi_a}{\phi_{in}^2 H_0^2} - 3\frac{y'}{y}\psi'\right]. \tag{3.25}$$

To solve these background equations, we need value of parameters $\Omega_{m_{in}}$, $V_a/\rho_{cr}$, $\phi_{in}H_0$ and $\phi_{in}/\phi_a$. On introducing variables defined in equation (3.16), with exponential potential, equations (3.10) and (3.12) for perturbed quantities $\Phi$ and $\delta\phi$ are

$$\begin{aligned}
&\Phi_N'' + 4\frac{y'}{y}\Phi_N' + \left\{2\frac{y''}{y} + \left(\frac{y'}{y}\right)^2\right\}\Phi_N \\
&\qquad = \frac{3}{2}\frac{V_a e^{-\frac{\phi_{in}}{a}\psi}}{\rho_{cr}}\sqrt{1-\phi_{in}^2 H_0^2\psi'^2}\left[\frac{\phi_{in}}{\phi_a}\delta\psi - \frac{\phi_{in}^2 H_0^2(\Phi_N\psi'^2 - \psi'\delta\psi')}{1-\phi_{in}^2 H_0^2\psi'^2}\right],
\end{aligned} \tag{3.26}$$

$$\begin{aligned}
&\frac{\delta\psi''}{\left(1-\phi_{in}^2 H_0^2\psi'^2\right)} + \left[3\frac{y'}{y} + \frac{2\phi_{in}^2 H_0^2\psi'\psi''}{\left(1-\phi_{in}^2 H_0^2\psi'^2\right)^2}\right]\delta\psi' \\
&\qquad + \left[-3\frac{\phi_{in}}{\phi_a}\frac{y'}{y}\psi' + \frac{K^2}{a_{in}^2 H_0^2 y^2} - \frac{\frac{\phi_{in}}{\phi_a}\psi''}{\left(1-\phi_{in}^2 H_0^2\psi'^2\right)} + \frac{\left(\frac{\phi_{in}}{\phi_a}\right)^2}{\phi_{in}^2 H_0^2}\right]\delta\psi \\
&\qquad - \left[12\frac{y'}{y}\frac{\psi'}{\psi} + \frac{2\left(2+\phi_{in}^2 H_0^2\psi'^2\right)\psi''}{\left(1-\phi_{in}^2 H_0^2\psi'^2\right)} - \frac{2\frac{\phi_{in}}{\phi_a}}{\phi_{in}^2 H_0^2} + \frac{2\phi_{in}^4 H_0^4\psi'^4\psi''}{\left(1-\phi_{in}^2 H_0^2\psi'^2\right)^2}\right]\Phi_N \\
&\qquad + \left[\frac{3\phi_{in}^2 H_0^2\psi'^3 - 4\psi'}{\left(1-\phi_{in}^2 H_0^2\psi'^2\right)}\right]\Phi_N' = 0.
\end{aligned} \tag{3.27}$$

In terms of the dimensionless variables, defined in equation (3.16), the equation for density parameters (3.13) for exponential potential takes the form

$$\frac{\delta_\phi}{\Phi_{in}} = -\frac{\phi_{in}}{\phi_a}\delta\psi - \phi_{in}^2 H_0^2\left(\frac{\psi'^2\Phi_N - \psi'\delta\psi'}{1-\phi_{in}^2H_0^2\psi'^2}\right),$$

$$\frac{\delta_m}{\Phi_{in}} = \frac{-2}{\Omega_{m_{in}}y^{-3}}\left[\frac{y'^2}{y^2}\Phi_N + \frac{y'}{y}\Phi_N' + \frac{k^2/H_0^2}{2a_{in}^2y^2}\Phi_N\right] - \left[\frac{\delta_\phi/\Phi_{in}}{\Omega_{m_{in}}y^{-3}}\frac{\frac{V_a}{\rho_{cr}}e^{-\frac{\phi_{in}}{\phi_a}\psi}}{\sqrt{1-\phi_{in}^2H_0^2\psi'^2}}\right]. \tag{3.28}$$

## 3.3 Results and Discussion

We evolve the perturbation equations from redshift $z = 1000$ to the present day. The main assumption we have made is that the dark energy field is initially homogeneous. Equation (3.13) suggests that for this assumption to be valid we need not only to consider $\delta\phi_{in} = 0$, but also $\dot{\bar{\phi}}_{in} = 0$ or equivalently an initial equation of state parameter of dark energy $w_{\phi_{in}} = -1$. Therefore the analysis, along with constraints on the free parameters we are providing, are subject to this assumption. For background equations, our initial conditions are

$$y_{in} = 1, \;\; \psi_{in} = 1, \tag{3.29}$$

and $\psi'_{in}$ can be calculated using relation

$$\psi' = \frac{\dot{\phi}}{\phi_{in}H_0} = \frac{\sqrt{1+w_\phi}}{\phi_{in}H_0}. \tag{3.30}$$

In [158], it has been shown that with the potentials mentioned in section 2.1, the constraint on matter density contrast is $\Omega_{m0} = 0.285^{+0.023}_{-0.022}$ at $3\sigma$ confidence. On the other hand, background data puts only a lower bound $\phi_0H_0 \gtrsim 0.775$ and all larger values are allowed. Here, $\phi_0$ is the value of the scalar field at present, i.e., $(\bar{\phi})_0$. Constraint on $w_{\phi 0}$ depends on the value of $\phi_0H_0$, as they are correlated quantities. The tachyon scalar field starts evolution only in the near past, this allow us to assume $\phi_{in}H_0 \approx \phi_0H_0$ [37]. In this chapter, we have done our analysis for the best fit value of $\Omega_{m0}$ and other parameters have been varied. In the case of the exponential potential, differences due to the change in the parameter $\phi_{in}/\phi_a$ can

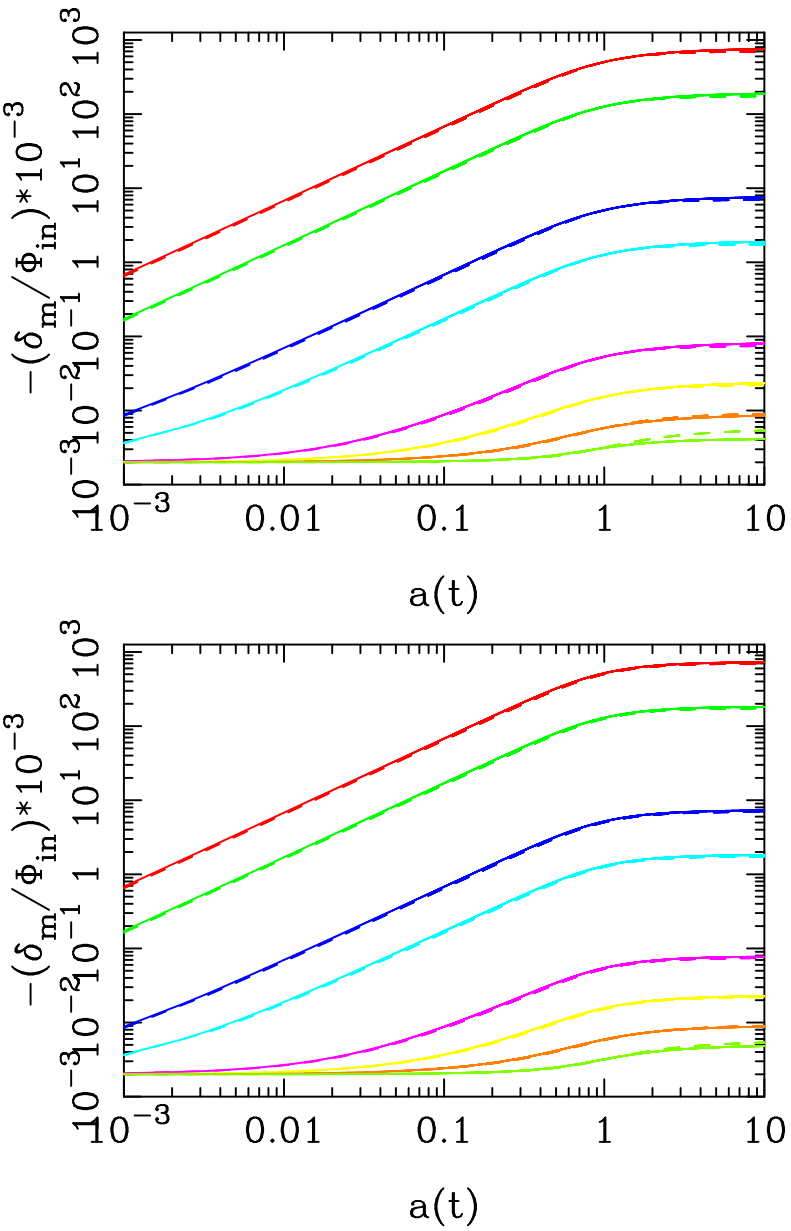


Figure 3.6: Evolution of matter density contrast with the scale factor. Solid lines correspond to tachyon dark energy with inverse square potential and the dashed lines are for $\Lambda CDM$ model. The plots on the top and the bottom correspond to $\phi_{in}H_0 =$ 1.0 and 2.0 respectively. The value of other parameter and colour scheme is same as in the figure 3.4.

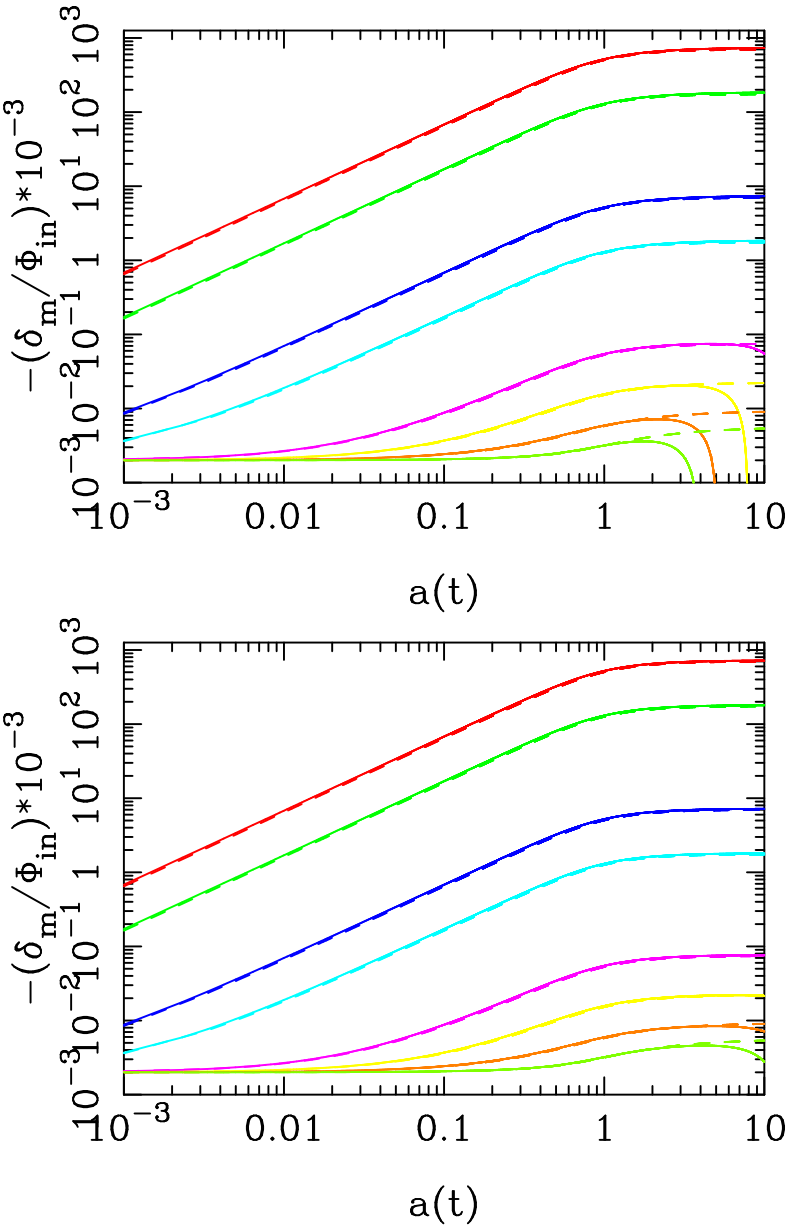


Figure 3.7: Evolution of matter density contrast with the scale factor is shown in the above figure. Solid lines correspond to tachyon dark energy model with exponential potential and the dashed lines are for $\Lambda CDM$ model. The plots on the top and the bottom correspond to $\phi_{in}H_0 =$ 1.0 and 2.0 respectively. The value of other parameter and colour scheme is same as in the figure 3.4.

be restored by scaling $\phi_{in}H_0$ appropriately [158]. We have fixed the value of this parameter at $\phi_{in}/\phi_a = 1$.

The evolution of the equation of state of dark energy and the density parameters are shown in figure 3.1 for inverse square potential and in figure 3.2 for exponential potential. Red, sky-blue, green and blue colours represent $\phi_{in}H_0 =$ 1.0, 1.5, 2.0 and 3.0. For each value of $\phi_{in}H_0$, we need to tune the amplitude of potential, $C_n = \frac{2n}{3}(1-2/3n)^{1/2}$ for the inverse square potential and $V_a/\rho_{cr}$ for the exponential potential, such that the present value of the matter density parameter matches $\Omega_{m0} = 0.285$. We can see that the equation of state parameter for both the potentials remains at $-1$ in the matter dominated era, and starts evolving as the dark energy begins to dominate. In the bottom panel of figure 3.3, we see that the deceleration to acceleration transition redshift, $z_{da}$, is higher for smaller value of $\phi_{in}H_0$ and gradually decreases as we increase this parameter. Hence for smaller values of $\phi_{in}H_0$, the value of equation of state parameter begin to deviate, or start increasing, from -1 earlier. That is the reason why $w_{\phi 0}$ is larger for these values than it is for the larger value of $\phi_{in}H_0$. For larger $\phi_{in}H_0$, the value of $w_{\phi 0}$ is closer to $-1$. This correlation can be seen in the top panel of the same figure. We find that for a given value of $\phi_{in}H_0$, $w_{\phi 0}$ relatively closer to $-1$ for the exponential potential than it is for the inverse square potential. The reason for this is that the transition from decelerated to accelerated expansion, for a fixed value of $\phi_{in}H_0$, occurs earlier for the inverse square potential than for the exponential potential. For example, for $\phi_{in}H_0 = 2.0$ the value of the transition redshift $z_{da} = 0.732$ for the inverse square potential and $z_{da} = 0.717$ for the exponential potential. Comparing both the panels of figure 3.3, we can conclude that there is a linear relation between $w_{\phi 0}$ and $z_{da}$.

The future evolution of $w_\phi$ can be seen in figure 3.1 and 3.1, and it is clear that the $w_\phi$ for the inverse square potential becomes constant in future, as for this potential, the equation of state asymptotically approaches $w_\phi = 2/3n - 1$ [37, 38, 39]. Whereas for the exponential potential, the equation of state increases to $w_\phi = 0$ (dust like). For smaller values of $\phi_{in}H_0$, it evolves faster and approaches $w_\phi = 0$ relatively earlier than for larger values of $\phi_{in}H_0$. Since in future the dominating component is dark energy, the effective equation of state of the Universe depends only on $w_\phi$. For the exponential potential, when $w_\phi$ becomes larger than $-1/3$, the Universe once again goes to a decelerating phase. Hence, for the exponential potential, there is no future horizon problem for tachyon model of dark energy [37, 38, 39].

The perturbation in the scalar field at initial (at $z = 1000$) is assumed to be

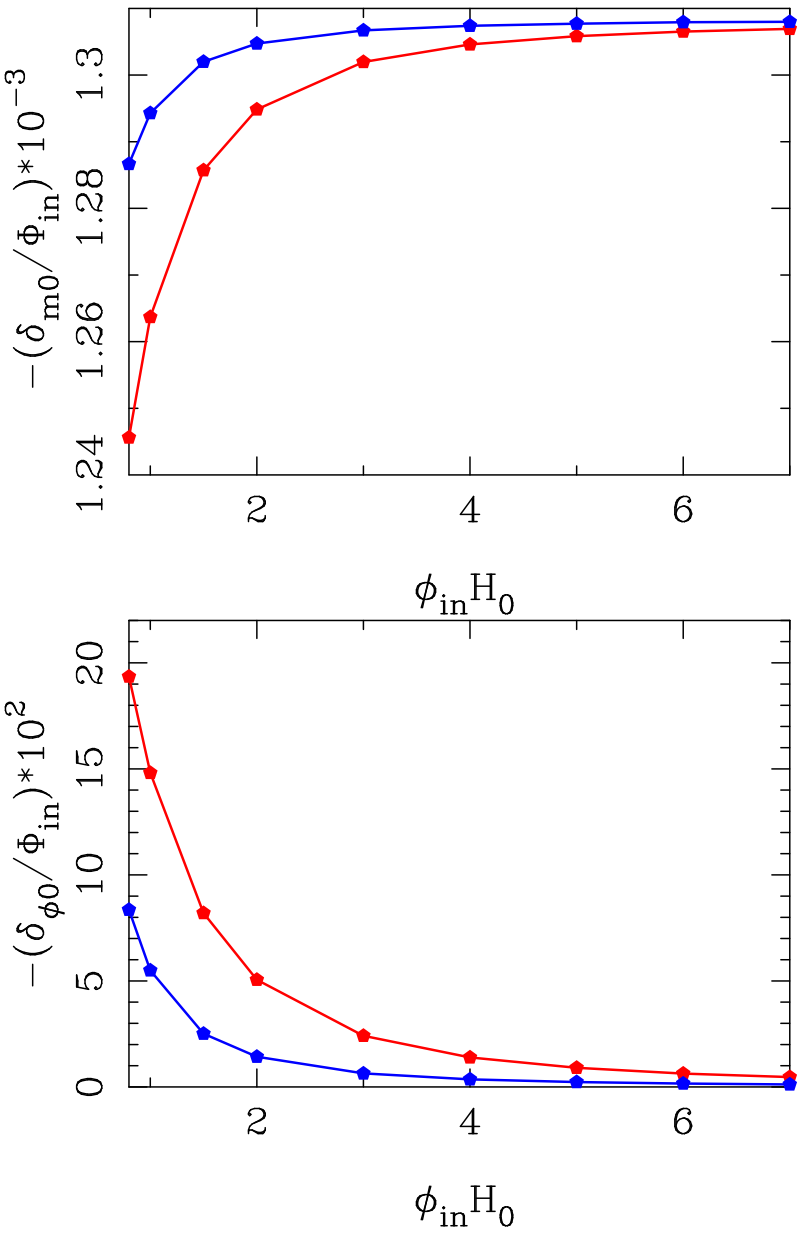


Figure 3.8: This figure shows the matter density contrast (in the top panel) and the dark energy density density contrast (in the bottom panel) normalized to initial gravitational potential, at present epoch ($z = 0$), as a function of $\phi_{in}H_0$ at the scale of $\lambda_p = 1000\,Mpc$. Red and blue colours represent the inverse square and exponential potentials respectively.

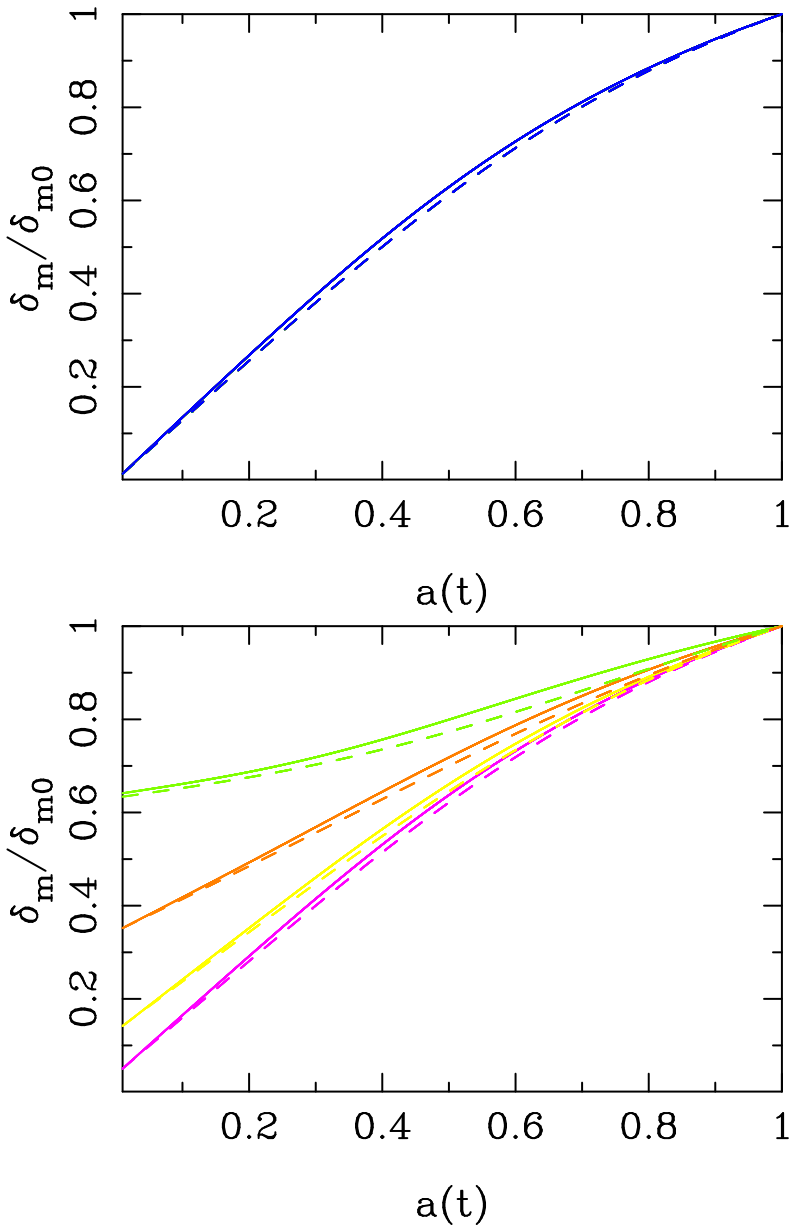


Figure 3.9: In this figure we show the evolution of linear growth function of matter $D_m^+ = \frac{\delta_m}{\delta_{m0}}$ as a function of the scale factor. Solid lines correspond to tachyon dark energy model with inverse square potential and the dashed lines are for $\Lambda CDM$ model. The colour scheme for scales of perturbation is the same as in 3.4. Plot on the top is for sub-Hubble scales and that on the bottom is for Hubble and super-Hubble scales.

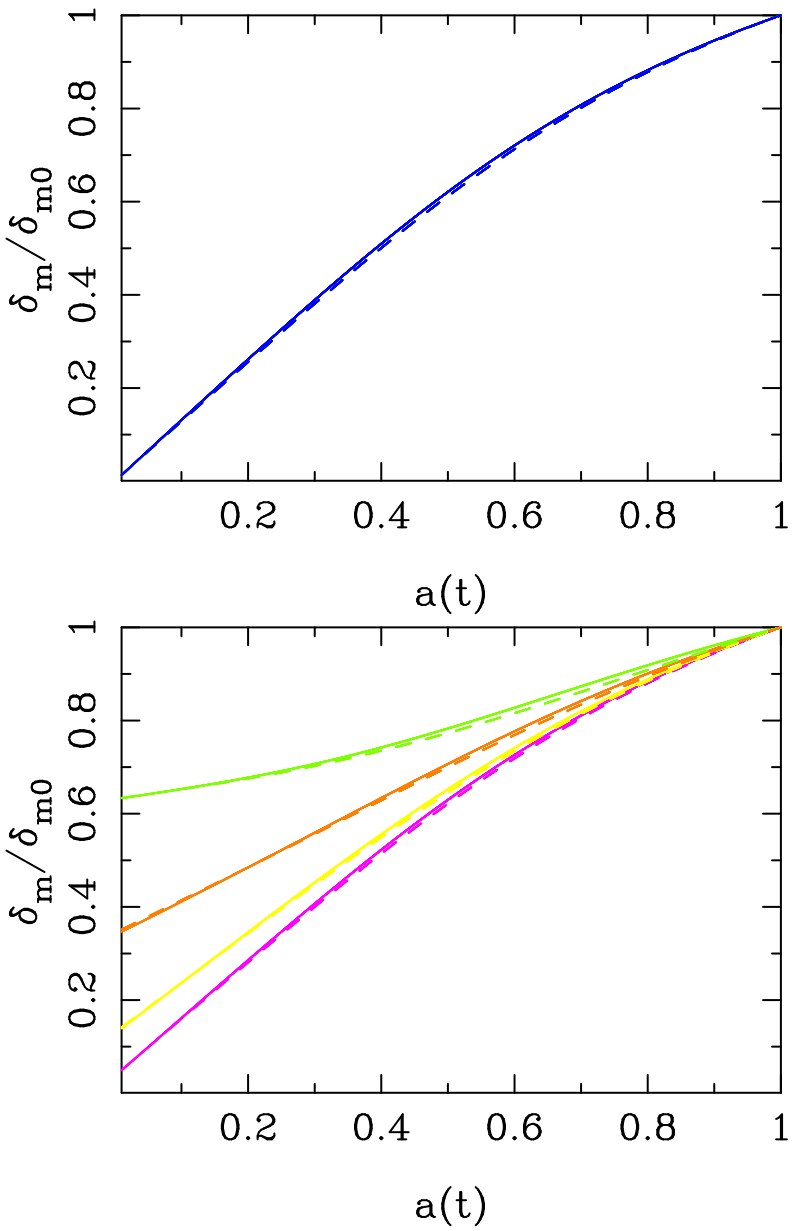


Figure 3.10: In this figure we show the evolution of linear growth function of matter $D_m^+ = \frac{\delta_m}{\delta_{m0}}$ as a function of the scale factor. Solid lines correspond to tachyon dark energy model with exponential potential and the dashed lines are for $\Lambda CDM$ model. The colour scheme for scales of perturbation is the same as in 3.4. Plot on the top is for sub-Hubble scales and that on the bottom is for Hubble and super-Hubble scales.

negligibly small, compared to $\Phi$ and $\delta_m$. The scalar field can initially be assumed to be homogeneous, and our initial conditions for perturbation are

$$\Phi_{N_{in}} = 1,\ \delta\psi_{in} = 0,\ \delta\psi'_{in} = 0. \tag{3.31}$$

In [26], it was shown that the gravitational potential does not evolve in the matter dominated era, and starts to decay when dark energy begins to dominate. This fact allows us to assume $\Phi'_{N_{in}}(k) = 0$, for all scales. In figures 3.4 and 3.5, we show the evolution of the gravitational potential with the scale factor. The gravitational potential is normalized to its initial value; solid lines are for tachyon models and dashed lines are for $\Lambda CDM$ model. Different colours represent different length scales of the perturbation, $\lambda_p$, from 50 $Mpc$ to $5 \times 10^4$ $Mpc$. We solve the set of required equations for each of these fixed scales, introduced using the dimensionless ratio $\bar{k} = kc/H_0$, where $k = 2\pi/\lambda_p$; with $H_0 = 70\, Kms^{-1}Mpc^{-1}$ and $c = 2.99\times10^5\, Kms^{-1}$. The gravitational potential remains a constant during the matter dominated era. As dark energy starts to dominate the energy budget, gravitational potential decays at all length scales. We can see that for $\Lambda CDM$ model, the gravitational potential falls more rapidly and at the same rate at all scales. For tachyon models, the gravitational potential decays more rapidly at a smaller scales than the larger scales. At super-Hubble scales, its decay slows down in future. In the top panel of figure 3.5, we see that for the exponential potential, the gravitational potential at super-Hubble scales in future first rises and then become constant. However, as we increase the value of parameter $\phi_{in}H_0$ (because $w_{\phi 0} \to -1$), this effect of scale dependence decreases, and the difference with respect to the $\Lambda CDM$ model also decreases. The model with exponential potential is more sensitive to the value of the parameter $\phi_{in}H_0$, as we can see that increasing this parameter from 1 to 2 decreases the scale dependence effect more significantly.

The evolution of matter density contrast, normalized by the initial value of the gravitational potential is shown in figures 3.6 and 3.7, for $\phi_{in}H_0 =$ 1.0 and 2.0. Since the gravitational potential remains constant during the matter-dominated era, at sub-Hubble scales the matter density contrast grows linearly with the scale factor i.e. $\delta_m \propto a$, whereas at Hubble and super-Hubble scale it evolves at a slower rate. In the matter dominated era, there is a very small difference between tachyon model (for both the potentials) and $\Lambda CDM$ model (dashed lines). In the dark energy dominated era, the evolution of matter density contrast is suppressed. At Hubble and super-Hubble scales with the exponential potential it decays in future. This difference in the behavior of the matter density contrast in future is due to the difference in the evolution of the equation of state parameter and the gravitational potential.

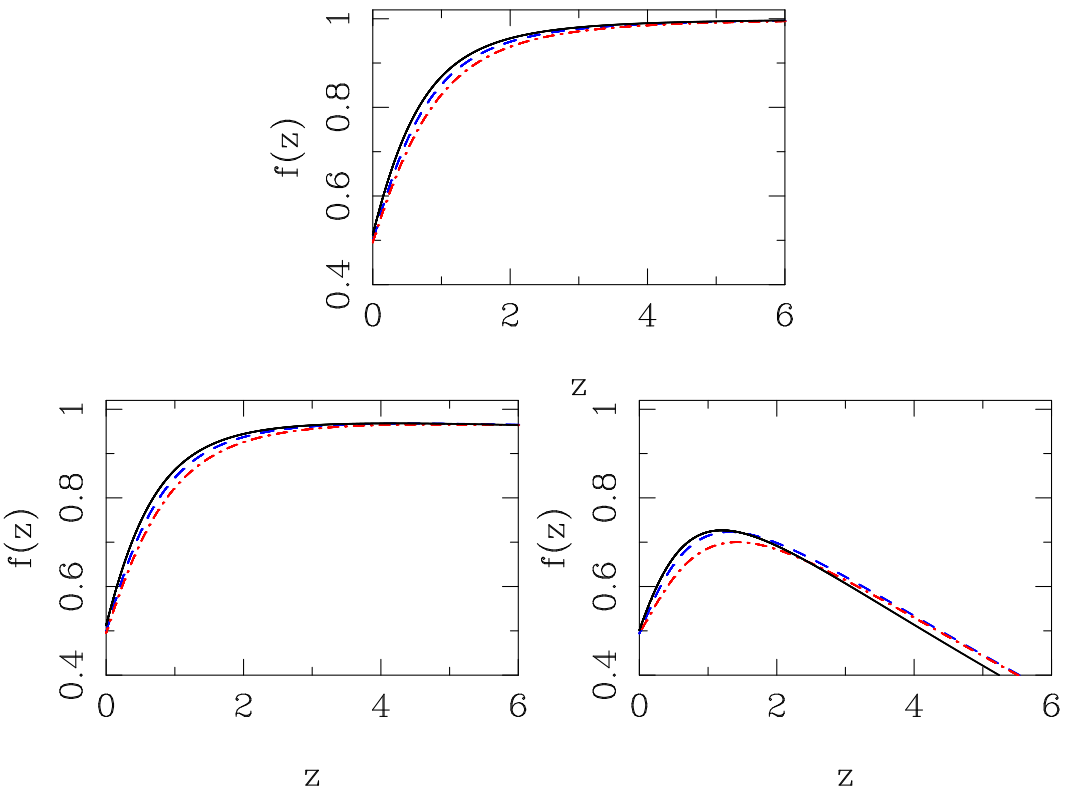


Figure 3.11: The evolution of the logarithmic growth rate $f = \frac{d\ ln\ \delta_m}{d\ ln\ a}$ with redshift is shown here. Solid black, dashed blue and dashed-dot red curves are for $\Lambda CDM$ model, tachyon model with exponential potential and with inverse square potential respectively. Top panel is for scale of perturbation $\lambda_p = 50\ Mpc$, whereas bottom left and right panels are for $\lambda_p = 1000\ Mpc$ and $5000\ Mpc$ respectively. For these plots, the value of parameters $\phi_{in}H_0 = 1.0$ and $\Omega_{m0} = 0.285$.

Whereas in the $\Lambda CDM$ model, the evolution of the matter density contrast remains suppressed in the $\Lambda$ dominated era. The evolution of $\delta_m$ depends on the parameter $\phi_{in}H_0$ (or on $w_{\phi 0}$). In the top panel of figure 3.8, we show the dependence of $\delta_m/\Phi_{in}$ at $z = 0$ at the scale of $\lambda_p = 1000\ Mpc$ on $\phi_{in}H_0$. For smaller value of $\phi_{in}H_0$ (or larger $w_{\phi 0}$), the present day value of $\delta_m(z = 0)$ is small, and as we increase $\phi_{in}H_0$ and $w_{\phi 0}$ decreases, the value of $\delta_m(z = 0)$ increases. For larger values of $\phi_{in}H_0$, its value approaches a constant as decrease in $w_{\phi 0}$ saturates. For a fixed value of $\phi_{in}H_0$, the value of $\delta_m(z = 0)$ is large for the exponential potential than it for the inverse square potential. For a fixed $\phi_{in}H_0$, the value of $w_{\phi 0}$ is smaller for the exponential potential than it is for the inverse square potential. As we increase the value of the parameter $\phi_{in}H_0$ and $w_{\phi 0}$ approaches $-1$, the difference between the two potentials decreases.

In top panels of figures 3.9 and 3.10, we show the evolution of linear growth function $D_m^+ = \frac{\delta_m}{\delta_{m0}}$ at sub-Hubble scales for the inverse square and exponential potentials respectively. Here, we have taken the value of parameters $\phi_{in}H_0 = 1.0$ and

$\Omega_{m0} = 0.285$. We can see that at sub-Hubble scales linear growth is scale independent, as all lines overlap. The bottom panels of these figures are for Hubble and super-Hubble scales. At these scales, the evolution of $D_m^+$ is scale dependent. In matter dominated era, the linear growth $D_m^+$ is large for tachyon models than the $\Lambda CDM$ model at all scales. That is why as dark energy dominates it has to slow down, even more than $\Lambda CDM$ model to match the present value. This becomes more clear in figure 3.11, where we show the evolution of growth rate $f = \frac{d\ ln\ \delta_m}{d\ ln\ a}$ with redshift, at the scale of perturbation $\lambda_p = 50,\ 1000$ and $5000\ Mpc$, for $\phi_{in}H_0 = 1.0$. We can see that the growth rate is higher at shorter scales, and as we increase the scale of perturbation growth rate decreases. We can also see that in matter-dominated era, the growth rate remains a constant for smaller scales (sub-Hubble scales), whereas at Hubble and super-Hubble scale it grows linearly and reaches a maximum value. In the dark energy dominated era the growth rate falls at all scales, for all the three models. In the matter-dominated era, the growth rate is larger for tachyon models than the $\Lambda CDM$ model. As the dark energy starts to dominate, it comes below the $\Lambda CDM$ model. As we increase the value of $\phi_{in}H_0$, the tachyon model approaches the $\Lambda CDM$ model (because $w_{\phi 0} \to -1$) and this difference decreases.

We show the evolution of dark energy perturbations as function of the scale factor in figure 3.13 for both the potentials. The dark energy density contrast is normalized to the initial gravitational potential. The magnitude of the dark energy density contrast is higher at larger scales. This behavior is opposite to that of the matter density contrast, which is higher in magnitude at smaller scales. As the dark energy dominates and gravitational potential decreases, the growth of the dark energy contrast ceases and becomes constant at Hubble and super-Hubble scale; this is true for the inverse square potential. For the exponential potential, if the value of parameter $\phi_{in}H_0$ is small, $\delta_\phi$ keeps on growing (with smaller rate) in the future. If we increase the value of this parameter, the growth of $\delta_\phi$ is suppressed for the exponential potential as well. At sub-Hubble scale, the dark energy density contrast reaches its maximum at near present epoch and then decreases in future.

The evolution of dark energy density contrast can be understood from the equation of $\delta_\phi$ in (3.13). At sub-Hubble scales, initially the second of three terms, term $\Phi\dot{\phi}^2$, dominates. Since in matter dominated era the gravitational potential remains a constant, $-\delta_\phi/\Phi_{in}$ rises as $\dot{\phi}^2$ or $w_\phi$ increases as a function of the scale factor. In dark energy dominated phase, due to decrease in gravitational potential, $-\delta_\phi/\Phi_{in}$ decreases. In future, the first term (term with scalar field perturbation $\delta\phi$) dominates, and as it rises $-\delta_\phi/\Phi_{in}$ rises once again. At super-Hubble scale the $\delta\phi$ rises, but other two terms fall. This results in a net suppression of evolution of $-\delta_\phi/\Phi_{in}$.

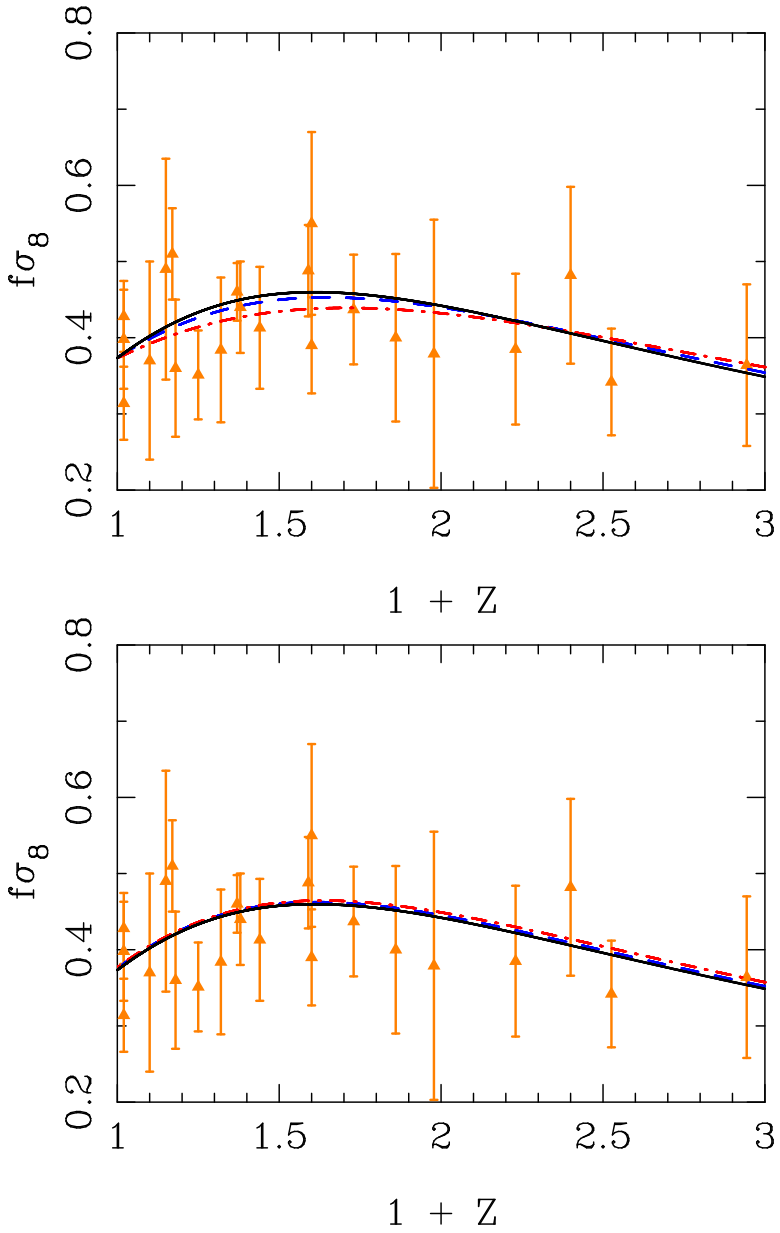


Figure 3.12: A comparison of theory with Redshift Space Distortion (RSD) data. Solid black, dashed blue and dashed-dot red curves are for $\Lambda CDM$ model, tachyon model with exponential potential and tachyon with inverse square potential respectively. The top and the bottom panels represent $\phi_{in}H_0 = 0.8$ and 3.0 respectively. Other parameters $\Omega_{m0}$ and $\sigma_8(z = 0)$ are fixed to the corresponding best fit values taken from table 3.2. Data points are taken from table I of [92].

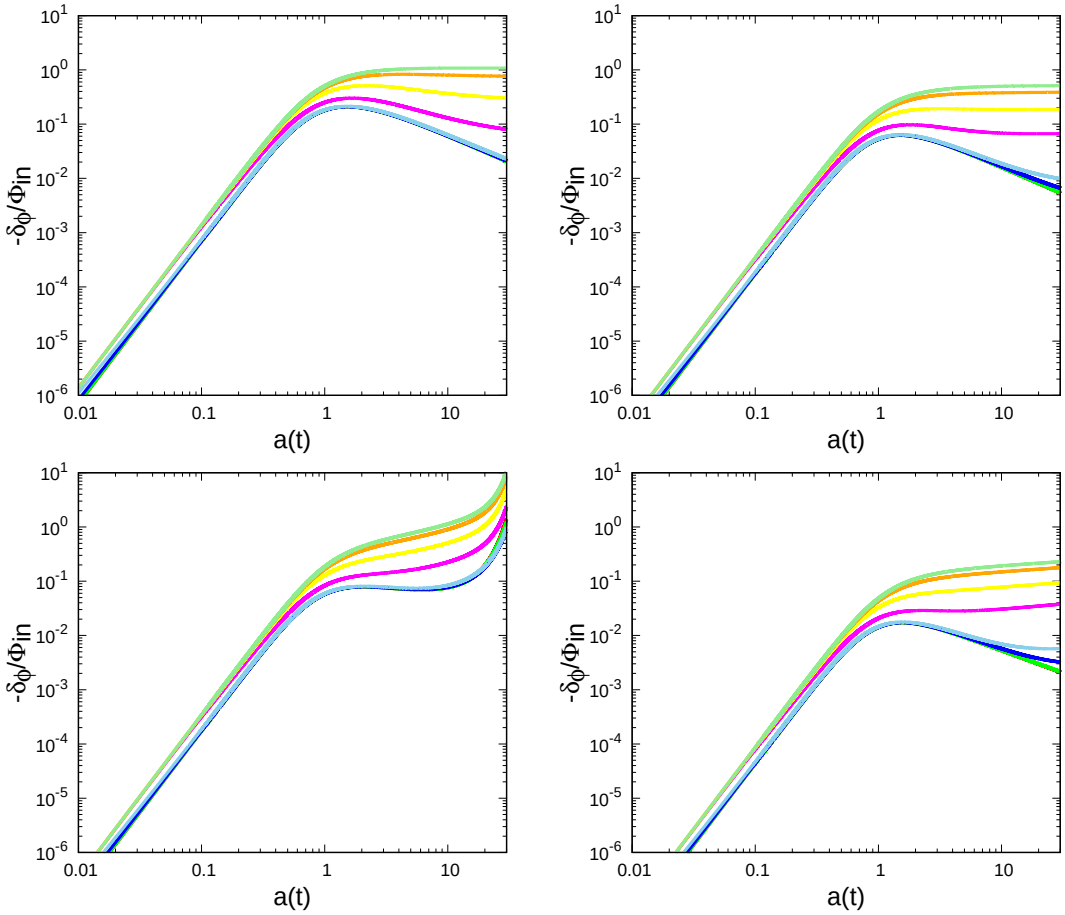


Figure 3.13: Evolution of dark energy density contrasts with the scale factor for tachyon model with inverse square potential (in row-1) and exponential potential (in row-2). Plots on the left and the right in each row correspond to $\phi_{in}H_0 = 1.0$ and 2.0 respectively. Amplitude of potentials $C_n$ and $A_n$ are tuned to get $\Omega_{m0} = 0.285$ at present. Red, green, blue, sky-blue, pink, yellow, orange and light-green lines represents the scale of perturbation $\lambda_p =$ 50, 100, 500, 1000, 5000, 10000, 20000 and 50000 $Mpc$ respectively.

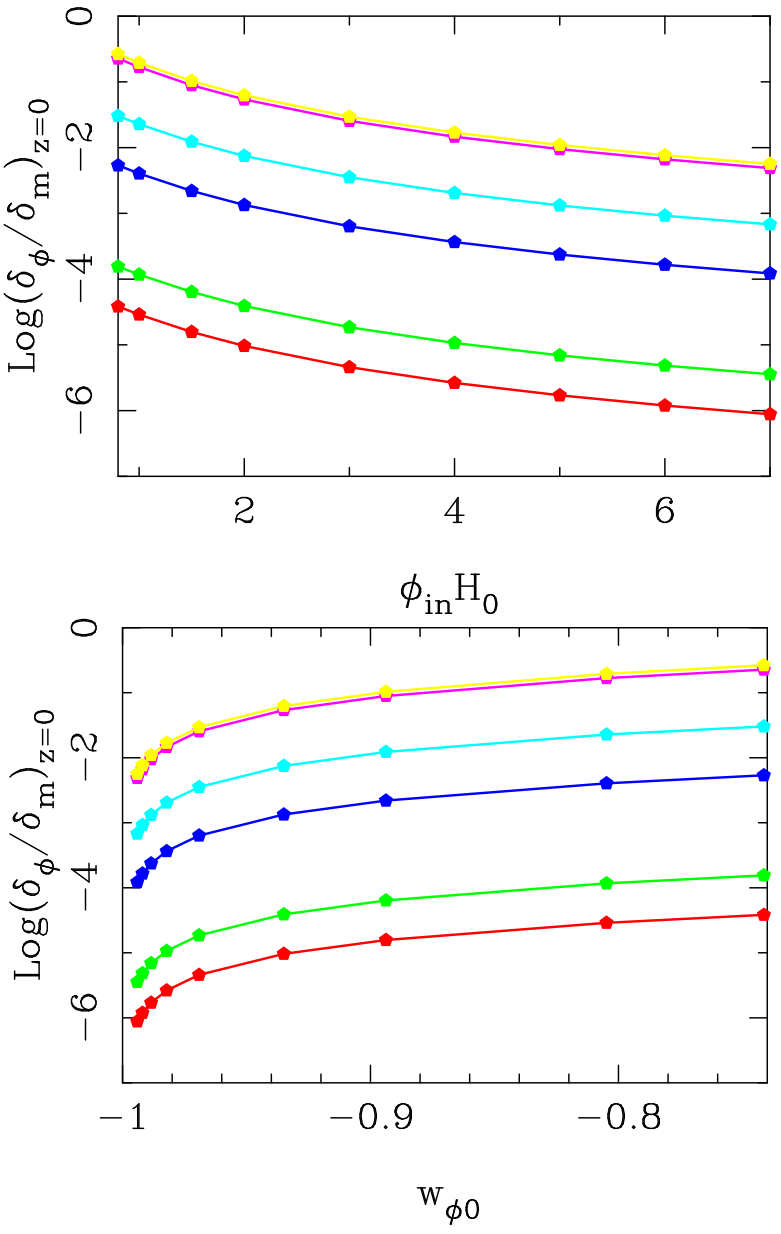


Figure 3.14: The plots shows the dependence of ratio $\delta_\phi/\delta_m$ on $\phi_{in}H_0$ and $w_{\phi 0}$ for the inverse square potential. Lines from bottom to top represent the scale of perturbation $\lambda_p =$ 500, $10^3$, $5\times10^3$, $10^4$, $5\times10^4$ and $10^5$ $Mpc$. Amplitude of potentials $C_n$ is fixed to get the present day $\Omega_{m0} = 0.285$.

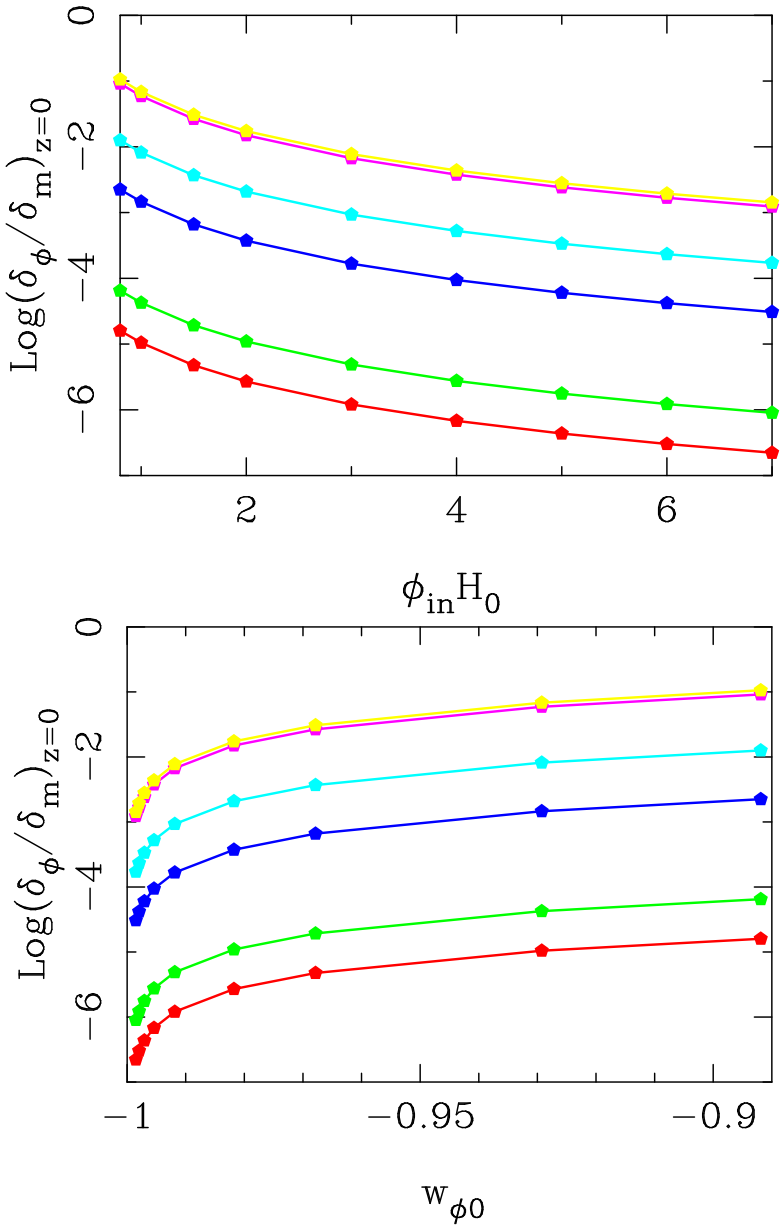


Figure 3.15: The plots shows the dependence of ratio $\delta_\phi/\delta_m$ on $\phi_{in}H_0$ and $w_{\phi 0}$ for the exponential potential. Colour scheme is same as in the figure 3.14. Amplitude of potentials $V_a/\rho_{cr}$ is fixed to get the present day $\Omega_{m0} = 0.285$.

For the exponential potential, with smaller value of $\phi_{in}H_0$, the $\delta\phi$ term dominates in future, and $-\delta_\phi/\Phi_{in}$ keeps on rising although with a smaller rate of growth. The density contrast $\delta_\phi/\Phi_{in}$ as a function of $\phi_{in}H_0$ is shown in the bottom panel of figure 3.8. We can see that for smaller value of this parameter (or larger $w_{\phi 0}$), dark energy perturbation is larger. As we increase $\phi_{in}H_0$ and $w_{\phi 0}$ approaches $-1$, the factor $\delta_\phi/\Phi_{in}$ becomes negligible, and we can consider dark energy as homogeneous. Although, the magnitude of $\delta_m$ is higher than that of $\delta_\phi$, we can see in figure 3.13 that in matter dominated era the slopes of $-\delta_\phi/\Phi_{in}$ curves, at all scales, are greater than that of $-\delta_m/\Phi_{in}$ (in figure 3.6). This implies that in matter dominated era the evolution of the dark energy density contrast is faster than that of the matter density contrast.

In figures 3.14 and 3.15, we show the ratio of density contrasts $\delta_\phi/\delta_m$ at present epoch $z = 0$ as a function of $\phi_{in}H_0$ and $w_{\phi 0}$. For a fixed scale, if the value of the parameter $\phi_{in}H_0$ is small, say of the order of unity (or the value of $w_{\phi 0}$ is away from -1), the value of $\delta_\phi/\delta_m$ is large. As we increase the value of $\phi_{in}H_0$ it decreases monotonically. For example, at $\lambda_p = 1000\ Mpc$ the value of $(\delta_\phi/\delta_m)_{z=0}$ is $1.172 \times 10^{-4}$ for $\phi_{in}H_0 = 1.0$, and it is $1.069 \times 10^{-5}$ for $\phi_{in}H_0 = 4.0$, for the inverse square potential. Near $w_{\phi 0} = -1$ the ratio $\delta_\phi/\delta_m$ decreases sharply. So $\delta_\phi/\delta_m \to 0$ as $w_{\phi 0} \to -1$.

In figures 3.16, we show the variation of $\delta_\phi/\delta_m$ with the scale of perturbation $\lambda_p$. We find that for smaller value of the field, say $\phi_{in}H_0 = 0.8$, at scale of $\lambda_p = 10^5 Mpc$, the ratio $(\delta_\phi/\delta_m)_{z=0} = 0.2645$ and 0.1060, for the inverse square and the exponential potential respectively. At these scales, the value of $\delta_m$ is very small, hence the value of $\delta_\phi$ is a considerable fraction of the energy density. This ratio decreases monotonically at smaller scales. For example, at $\lambda_p = 10^2 Mpc$ the ratio $(\delta_\phi/\delta_m)_{z=0}$ is in the range $10^{-6}$ to $10^{-8}$. While the dark energy density contrast is negligible at smaller scales (sub-Hubble scales), it is significant at Hubble and super-Hubble scales.

### 3.3.1 Effect of Inhomogeneities in the Dark Energy at Early Universe

We also study the effect of deviation of initial equation of state parameter from $-1$ at early epoch. For this, we vary the value of $w_{\phi_{in}}$ at $z = 1000$ from $-1$ assuming perturbation in scalar field $\delta\phi$ and its derivative $\delta\dot{\phi}$ negligibly small. In figure 3.17, we show the evolution of the equation of state parameter in this scenario for both the

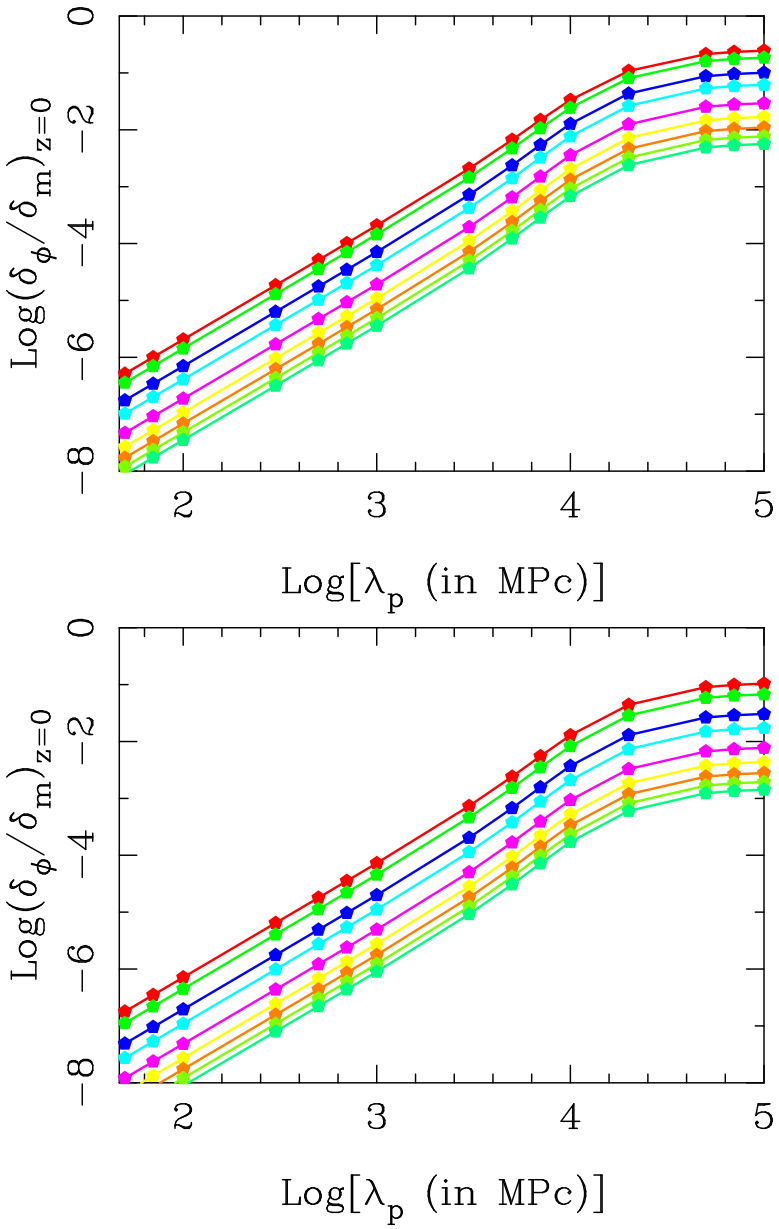


Figure 3.16: In this figure, we have plotted the ratio $\delta_\phi/\delta_m$ with respect to the scale for the inverse square potential (in the top panel) and for the exponential potential (in the bottom panel). For curves from top to bottom, in each panel, values of the the parameter $\phi_{in}H_0 =$ 0.8, 1.0, 1.5, 2.0, 3.0, 4.0, 5.0, 6.0 and 7.0.

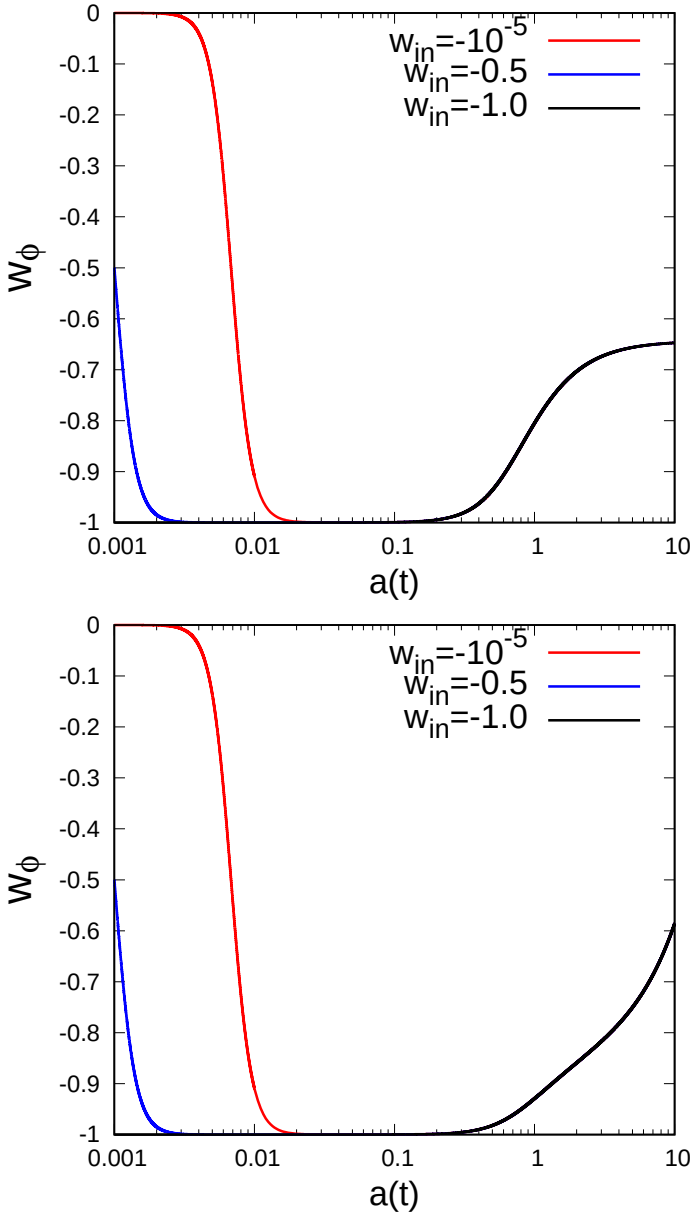


Figure 3.17: Evolution of the equation of state parameter $w_\phi$ for $V(\phi) \propto \phi^{-2}$ (top panel) and for $V(\phi) \propto exp(-\phi/\phi_a)$ (bottom panel). Red and blue colours represent initial equation of state parameter of dark energy $w_{\phi_{in}}$ to be $-10^{-5}$ and $-0.5$ respectively. The black curves are for initially homogeneous dark energy with $w_{\phi_{in}} = -1$. We have fixed the value of parameter $\phi_{in}H_0 = 1.0$ and $\Omega_{m0} = 0.285$ for these plots.

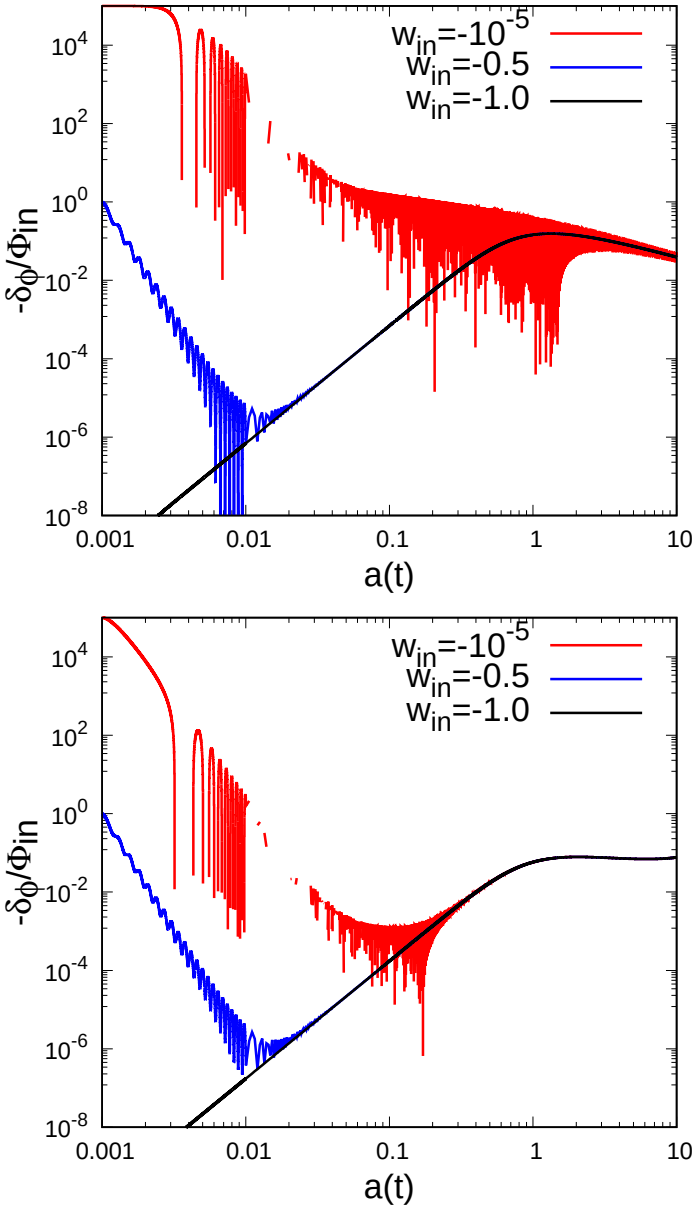


Figure 3.18: Evolution of $\delta_\phi/\Phi_{in}$ at scale of 50 $Mpc$. Plot on the top is for $V(\phi) \propto \phi^{-2}$ and on the bottom is for $V(\phi) \propto exp(-\phi/\phi_a)$. Colour scheme and the values of parameters $\phi_{in}H_0$ and $\Omega_{m0}$ are same as in figure 3.17.

| $\phi_{in}H_0$ | $\Omega_{m0}$ | $\sigma_8(0)$ | $w_{\phi_{in}}$ |
|---|---|---|---|
| $[0.001, 10.0]$ | $[0.01, 0.9]$ | $[0.1, 3.0]$ | $[-10^{-10}, -1]$ |

Table 3.1: Priors ranges for the parameters $\Omega_{m0}$, $\phi_{in}H_0$, $\sigma_8(0)$ and $w_{\phi_{in}}$

potentials. We can see, even if $w_{\phi_{in}}$ deviate from $-1$, the equation of state parameter $w_\phi$ sharply approaches to it with the Hubble expansion of the Universe. We find that only for the cases where $w_{\phi_{in}} \approx 0$ (a fluid like equation of state), $w_\phi$ survives deep into the matter dominated era. There is no effect of the parameter $w_{\phi_{in}}$ on the evolution of $w_\phi$ in later epoch. Equation 3.13 suggest that deviation of $w_\phi$ from $-1$ (hence $\dot{\phi} \neq 0$) introduce contrast in dark energy through gravitational potential. Larger the value of $w_{\phi_{in}}$ larger the dark energy contrast $\delta_\phi$ in early epoch. We show results for sub-Hubble scale in figure 3.18. In this figure, we can see that the early perturbations in dark energy go throw a damped oscillation as the equation of state parameter approaches $-1$. The dark energy contrast $\delta_\phi$ decreases in amplitude until it approach to evolution track of $w_{\phi_{in}} = -1$ case. After that, $\delta_\phi$ for all values of $w_{\phi_{in}}$ follow same track. In figure 3.19, we can see that at sub-Hubble scales there is no effect of deviation of $w_{\phi_{in}}$ or early dark energy perturbations on the matter density contrast $\delta_m$ or on the linear growth function $D_m^+ = \delta_m/\delta_{m0}$ for both the potentials. Reason for this behavior can be understood from the Equation 3.13. In matter dominated era, the ratio of dark energy density to matter density ($\rho_\phi/\rho_m$) is vary small. Therefore, at early epoch it does not affect $\delta_m$. At present epoch $\delta_\phi$ itself very small for all the $w_{\phi_{in}}$ in comparison to $\delta_m$ at sub-Hubble scales. Even if we vary $\delta\phi_{in}$, it does not affect the evolution of linear growth function $D_m^+$ at sub-Hubble scales. The effect of perturbation in dark energy (and deviation of $w_{\phi_{in}}$ from $-1$) is considerable only at the Hubble and super-Hubble scales, where the ratio $\delta_\phi/\delta_m$ become significant.

### 3.3.2 Constraints on the Parameters

Observations do not provide a direct measurement of $\delta_m$. Instead, the observational data on the growth of structure measures the product $f\sigma_8(z)$, where,

$$\sigma_R^2(z) = \frac{1}{2\pi^2}\int_0^\infty P(k,z)W_R^2(k)k^2dk \propto \delta^2(z), \tag{3.32}$$

is the root mean square fluctuation in linear density field or power spectrum $P(k,z)$ within a sphere of radius $R$ [159]. Taking $R = 8\ h^{-1}Mpc$, it can be written as,

$$\sigma_8(z) = \sigma_8(0)\frac{\delta_m(z)}{\delta_m(0)}. \tag{3.33}$$

Here, $\sigma_8(0)$ is the present value of $\sigma_8(z)$ and it is a parameter. In figure 3.12, we show the comparison between data and theory. The data points are values of $f\sigma_8(z)$ extracted from redshift space distortion (RSD) measurements. We have used 22 RSD data points from redshift 0.02 to 1.944, which includes data from 'Gold-2017' compilation [9] and some new measurements [92]. This data set is described and listed in section 1.6.6. In figure 3.12, solid black, dashed blue and dashed-dot red curves are for $\Lambda CDM$ model, tachyon model with exponential potential and with inverse square potential respectively. Left and right panels are for $\phi_{in}H_0 =$ 0.8 and 3.0 respectively. We set the parameters $\Omega_{m0}$ and $\sigma_8(0)$ to their corresponding best fit values given in table 3.2. We can see that the tachyon models (with both the potentials) are in good agreement with the data. There is significant difference between tachyon models and the $\Lambda CDM$ model if the parameter $\phi_{in}H_0$ is small (about order of unity) or large $w_{\phi 0}$ (because these two parameters are correlated). As we increase $\phi_{in}H_0$ and $w_{\phi 0}$ approaches $-1$, tachyon models then coincide with the $\Lambda CDM$ model.

We now constrain the free parameters of the tachyon field model using Redshift Space Distortion (RSD) data. We find out the maximum likelihood by minimizing $\chi^2$ given by equation (1.108). The quantities $\mathbf{X_{th}}$ and $\mathbf{X_{obs}}$ are the vectors of theoretical and observed values of the observable $f\sigma_8$ respectively. As suggested in [9], to remove the fiducial cosmology, we scale the theoretical value of $f\sigma_8$ by the ratio

$$r(z) = \frac{H(z)d_A(z)}{H^{fid}(z)d_A^{fid}(z)}, \tag{3.34}$$

where $H(z)$ and $d_A(z)$ are the Hubble parameter and the angular diameter distance at redshift $z$ respectively. The observable $X_{th,i} = r(z_i)f\sigma_8(z_i,\mathbf{p})$, where $\mathbf{p}$ is the set of parameters. We constrain the parameters $\Omega_{m0}$, $\phi_{in}H_0$ and $\sigma_8(0)$. The prior used for these parameters are shown in table 3.1. Since, the parameter $w_{\phi_{in}}$ does not affect the evolution of $D_m^+ = \delta_m/\delta_{m0}$ at sub-Hubble scale, we do not see any change in the theoretical value of $f\sigma_8$ by varying this parameter. The RSD data set, we have used, does not constrain $w_{\phi_{in}}$. We have checked it by varying $w_{\phi_{in}}$ in the prior range $[-10^{-10},-1]$ for this parameter. Therefore, we need not include this parameter in our analysis. For the exponential potential, we have fixed $\phi_{in}/\phi_a = 1.0$, since changes due to variation in this parameter can be compensated by scaling $\phi_{in}H_0$

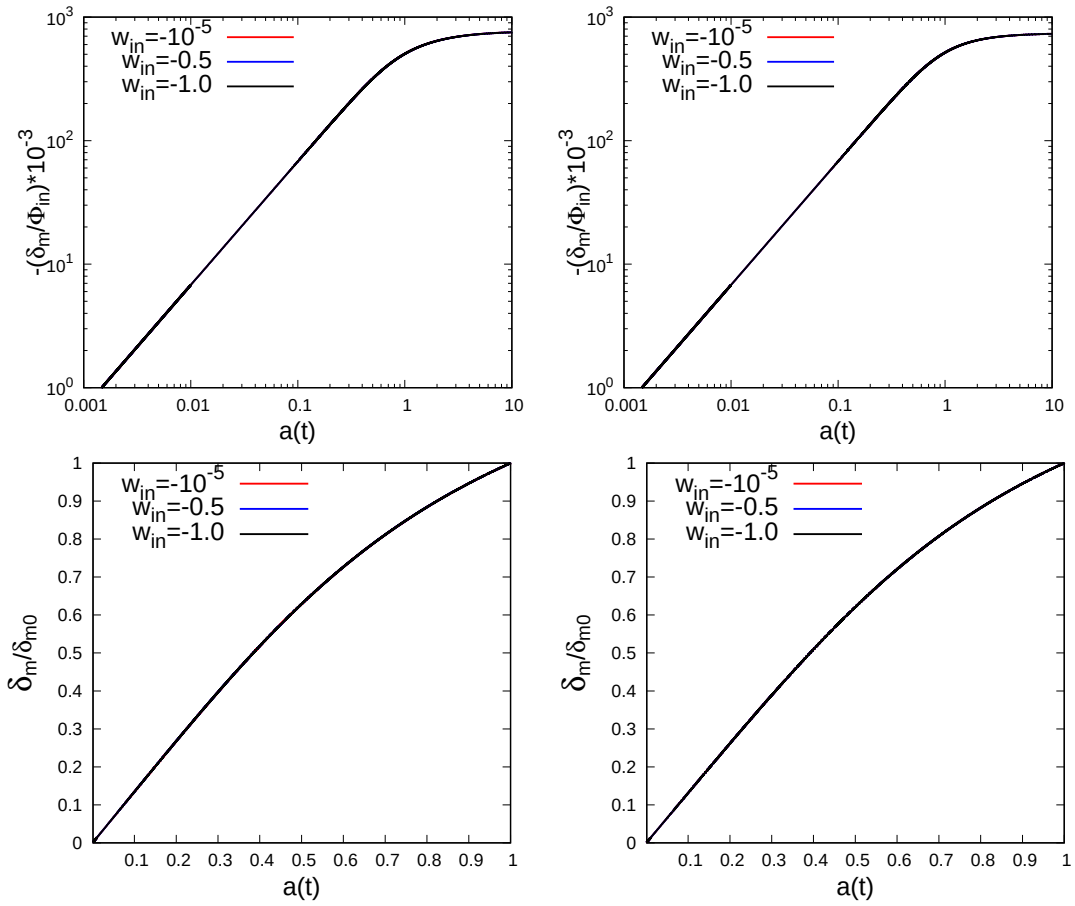


Figure 3.19: Evolution of $\delta_m/\Phi_{in}$ and$\delta_m/\delta_{m0}$ at scale of 50 $Mpc$. Column-1 and 2 are for $V(\phi) \propto \phi^{-2}$ and $V(\phi) \propto exp(-\phi/\phi_a)$ respectively. Colour scheme and the values of parameters $\phi_{in}H_0$ and $\Omega_{m0}$ are same as in figure 3.17.

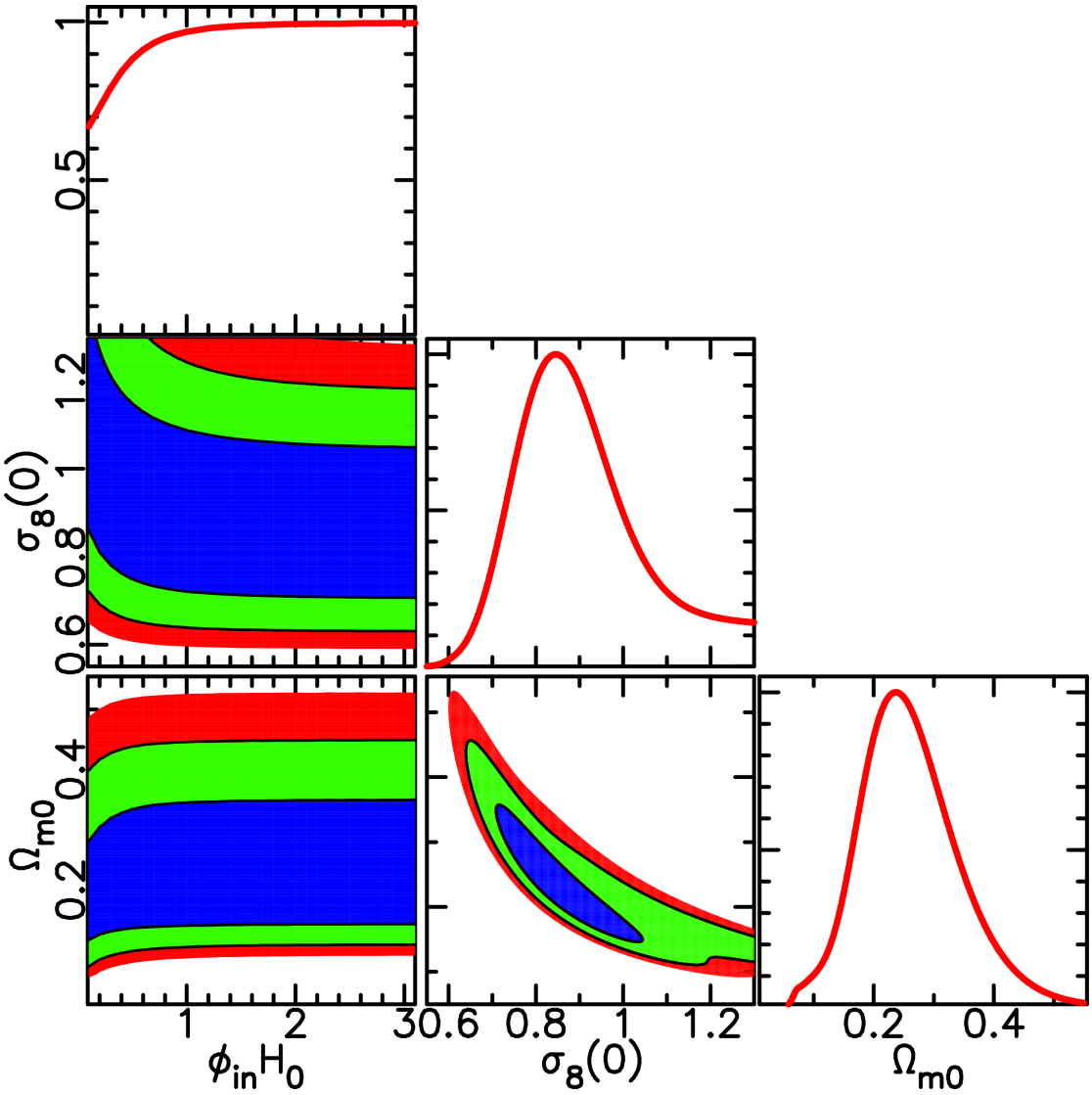


Figure 3.20: Marginalized Constraints and the likelihood for the parameters $\Omega_{m0}$, $\phi_{in}H_0$ and $\sigma_8(0)$ of the tachyon model with inverse square potential. The 2D-contours filled with blue, green and red colours show 68%, 95% and 99% confidence region respectively. We do not include results for the parameter $w_{\phi_{in}}$ because it is not constrained by the data we use (see sections 3.3.1 and 3.3.2 for details)

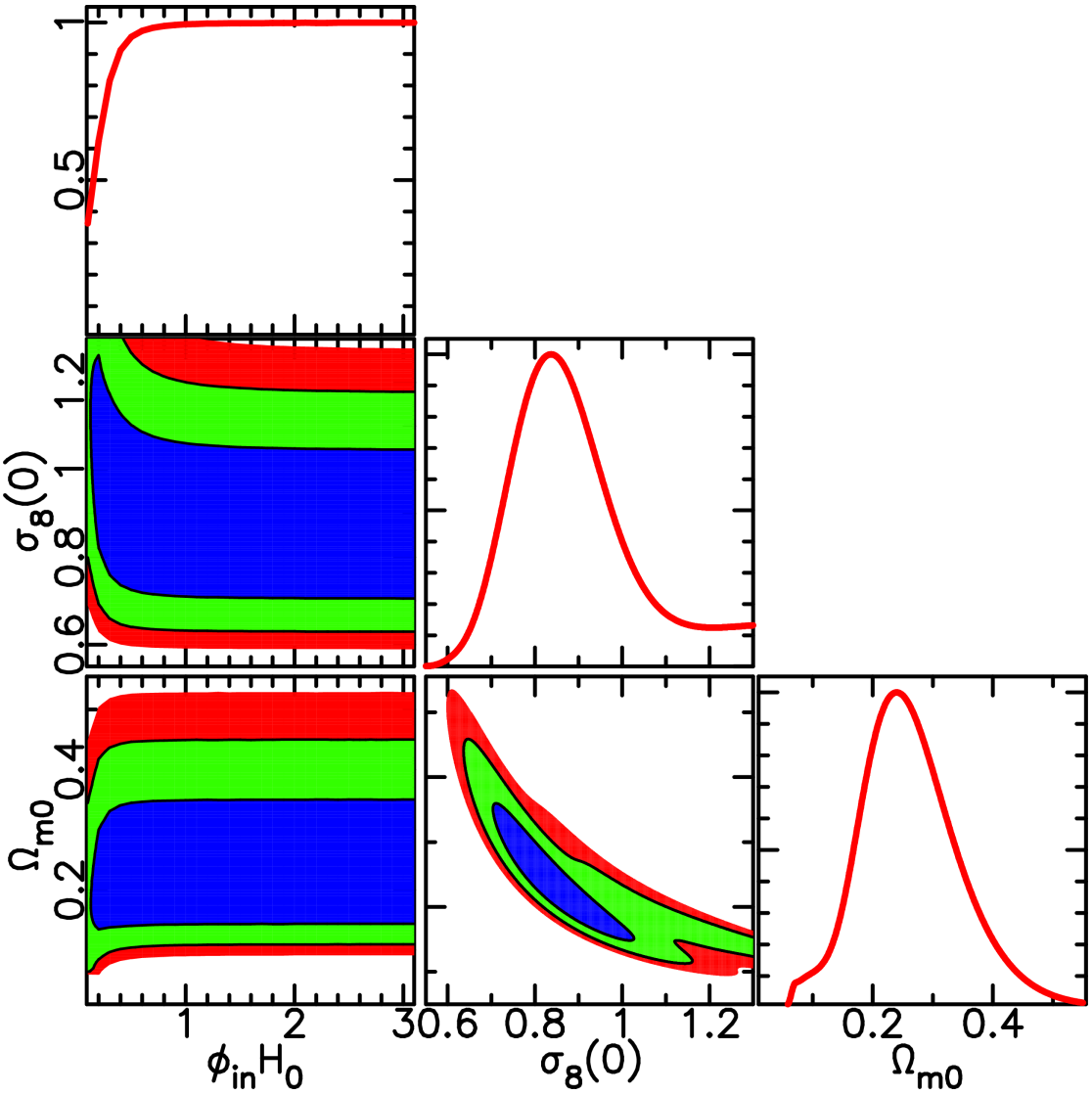


Figure 3.21: Marginalized Constraints and the likelihood for the parameters $\Omega_{m0}$, $\phi_{in}H_0$ and $\sigma_8(0)$ of the tachyon model with exponential potential. The 2D-contours filled with blue, green and red colours show 68%, 95% and 99% confidence region respectively. We do not include results for the parameter $w_{\phi_{in}}$ because it is not constrained by the data we use (see sections 3.3.1 and 3.3.2 for details).

appropriately [158].

In figures 3.20 and 3.21, we show the marginalized contours of 68%, 95% and 99% confidence region for the tachyon model with inverse square potential and the exponential potential respectively. We also show the one dimensional likelihood for each parameter. We find that the constraints on the parameter $\phi_{in}H_0 > 0.081$ at 99% confidence level for model with exponential potential have no upper bound on it. This can also be seen in the likelihood function of the parameter $\phi_{in}H_0$ which becomes constant for larger values. We have checked it for arbitrarily large values of this parameter. For tachyon model with inverse square potential $\phi_{in}H_0 \gtrsim 0.001$. Since only the square of the parameter $\phi_{in}H_0$ appears in the equations, we show results only for positive branch. We obtain similar results as have been shown in our previous study with background data [158]. As mentioned earlier, a smaller value of $\phi_{in}H_0$ leads to $w_{\phi 0}$ away from $-1$ and allows dark energy to be perturbed. We conclude that the growth-rate data we use does not rule out perturbations in dark energy. When the value of parameter $\phi_{in}H_0$ is small, say less than 0.1, data prefers a relatively smaller value of $\Omega_{m0}$ and a larger value of $\sigma_8(0)$. This correlation is found for both the potentials. Since, a large range of initial field is allowed by the data, we do not need to fine tune the value of the parameter $\phi_{in}H_0$.

We also show constraints in the $\Omega_{m0}-\sigma_8(0)$ plane and find them to be consistent with the observations. In table 3.2, we show the best fit values of parameters along with their 68%, 95% and 99% confidence range for tachyon model with both the potentials, as well as for $\Lambda CDM$ model. In figure 3.22, we compare the constraints on $\Omega_{m0}-\sigma_8(0)$ plane for tachyon models with constraint for the $\Lambda CDM$ model. Here, the black dot and triangle show the best fit values for Planck-2015 [66] and Planck-2018 [60] respectively. The constraints on $(\Omega_{m0}, \sigma_8)$ for $\Lambda CDM$ model are $(0.3156\pm 0.0091,\ 0.831\pm 0.013)$ from Planck-2015 (TT,TE,EE+lowP) at 68% confidence [66] and $(0.3166 \pm 0.0084,\ 0.8120 \pm 0.0073)$ from Planck-2018 (TT,TE,EE+lowE) at 68% confidence [60]. We find that Planck-2015 and Planck-2018 best fit points are at $2.9\sigma$ and $2.26\sigma$ levels respectively for $\Lambda CDM$ model. Similar result has also been found between 'Gold-2017' growth rate data and Planck-2015 data for $\Lambda CDM$ model, see [9] for more details. This tension is reduced in the tachyon models. The best fit values of Planck-2015 and Plank-2018 are at $1.93\sigma$ and $1.66\sigma$ levels respectively for the tachyon model with inverse square potential. For the tachyon model with exponential potential these points are at $2.45\sigma$ and $1.86\sigma$ levels respectively. Therefore, we can see that inclusion of perturbation in dark energy with $w_{\phi 0} \neq -1$ reduces the tension between RSD data and Planck data.

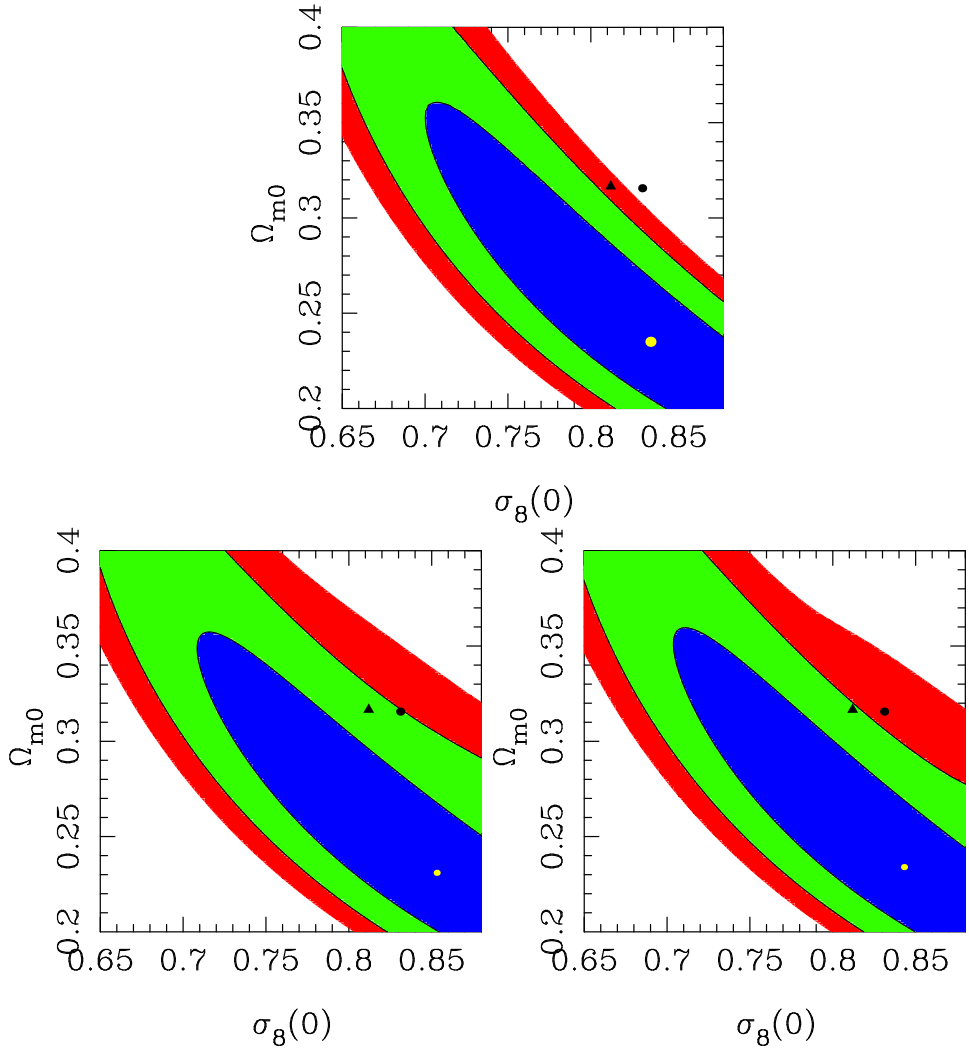


Figure 3.22: Marginalized constraints on $\Omega_{m0} - \sigma_8(0)$ plane. Blue, green and red colors represent the 68%, 95% and 99% confidence region respectively. Top plot is for $\Lambda CDM$ model whereas bottom left and right plots are for the tachyon model with inverse square and exponential potentials respectively. The black dot and triangle show the best fit values for Planck-2015 [66] and Planck-2018 [60] respectively.

To compare the models, we calculate Bayesian evidence for all the three models. The Bayesian evidence or model likelihood is defined in the equation (1.107). Clearly, the evidence is the average value of the likelihood over entire parameter space. Two models $M_0$ and $M_1$ can be compared using the ratio of their Bayesian evidences known as the Bayes factor $B_{01}$, defined in equation (1.112). The Bayes factor indicate the change in relative odds between the models after arrival of data. If $B_{01} > (<)1$ then the model $M_0$ is more (less) favorable than the model $M_1$ by the given data. The Jeffreys' scale provides an empirically calibrated scale for strength of evidence to compare the two models [98]. A notable property of the evidence is that it does not penalize the parameter which is unconstrained by the data [93], e.g. in our case the initial value of the equation of state $w_{in}$. There are other popular and simpler way to compare different models, namely Akaike Information criterion (AIC) and Bayesian Information criterion (BIC) [93, 94, 95]. These methods require only the maximum likelihood to compare models [93, 94]. These criterion are derived using various assumptions, e.g. Gaussianity of the posterior distribution. These assumptions are not valid for the tachyon models, as posteriors (particularly for $\phi_{in}H_0$) are not Gaussian. Therefore, we do not use AIC or BIC for comparison and rely on evidence calculation and Bayes factor. We find that $B_{01} = 0.996$ and $B_{02} = 1.019$, where '0' stands for $\Lambda CDM$ model, '1' for tachyon models with inverse square potential and '2' for tachyon models with exponential potential. For this calculation we take uniform or flat prior for all three models. Since, Bayes factor $1 < B < \sqrt{10}$ is only a weak evidence [98], we clearly find that the RSD data, we use, does not exclusively favor any of these models. Therefore, we conclude that the tachyon models are as good as $\Lambda CDM$ model to satisfy this data set.

## 3.4 Summary and Conclusions

In this chapter, we have studied perturbations in tachyon scalar field dark energy and their effect on matter clustering. We consider two tachyon scalar field potentials, the inverse square potential and the exponential potential. We begin with a homogeneous dark energy with equation of state $w_{\phi_{in}} = -1$ and evolve our equations with time. Gravitational potential remain constant in matter dominated era, and decay as dark energy starts to dominate the energy budget. For the $\Lambda CDM$ model evolution of gravitational potential is scale independent, whereas for the tachyon models it depends on scale. Decay of gravitation potential in future for tachyon models slows down as we go for larger scales. The matter and dark energy perturbations are coupled with each other and if the equation of state of dark energy $w_\phi \neq -1$ then dark

| Model | $\chi_{min}$ | $\phi_{in}H_0$ | $\Omega_{m0}$ | $\sigma_8(0)$ |
|---|---|---|---|---|
| $\Lambda CDM$ | 12.260 | - | $0.235^{+0.125+0.209+0.306}_{-0.085-0.116-0.140}$ | $0.836^{+0.175+0.286+0.401}_{-0.135-0.193-0.242}$ |
| Tachyon With $V(\phi) \propto e^{-\phi/\phi_a}$ | 12.252 | $> 0.081$ | $0.234^{+0.125+0.209+0.306}_{-0.085-0.149-0.194}$ | $0.843^{+0.183+0.897+1.807}_{-0.139-0.197-0.248}$ |
| Tachyon with $V(\phi) \propto \phi^{-2}$ | 12.255 | $\gtrsim 0.001$ | $0.231^{+0.126+0.210+0.307}_{-0.084-0.131-0.180}$ | $0.853^{+0.191+0.742+1.597}_{-0.144-0.204-0.255}$ |

Table 3.2: The table lists the best fit values of $\Omega_{m0}$ and $\sigma_8(0)$ along with their $1\sigma$, $2\sigma$ and $3\sigma$ confidence ranges for the $\Lambda CDM$ model as well as tachyon model with both the potentials. In column-2 we show the lower bound on the parameter $\phi_{in}H_0$. To constrain the parameters we use 22 RSD data points compiled and tabulated in [9, 92].

energy is not distributed homogeneously. Distribution of inhomogeneity in tachyon dark energy, like in other scalar field models, is a scale dependent phenomenon. The dark energy density contrast $\delta_\phi$ is higher in magnitude at larger scales than it is at shorter scale, opposite to the matter density contrast $\delta_m$ which is higher at shorter scales. In matter-dominated era at sub-Hubble scales, $\delta_m \propto a(t)$ for tachyon models as well as for the $\Lambda CDM$ model. In dark energy dominated era, its evolution is suppressed. Future evolution of matter density contrast is significantly different in all three models. At super-Hubble scales, $\delta_m$ rises again for the inverse square potential, and falls for the exponential potential, whereas for the $\Lambda CDM$ model it remains a constant. In the matter dominated era, dark energy density contrast $\delta_\phi$ evolves monotonically at same rate at all scales with $a(t)$. Although the magnitude of $\delta_\phi$ is much smaller than that of $\delta_m$ in matter dominated era, its growth rate is higher. We also study the effect of parameters, $\phi_{in}H_0$ and $w_{\phi 0}$, on the evolution of $\delta_m$ and $\delta_\phi$. These two parameters are correlated and as we increase the value of $\phi_{in}H_0$, $w_{\phi 0} \to -1$ (a $\Lambda CDM$ value).

We have also studied the evolution linear growth function $D_m^+ = \delta_m/\delta_{m0}$ and the growth rate $f = \frac{d\ ln\ \delta_m}{d\ ln\ a}$. Evolution of $D_m^+$, at sub-Hubble scales is scale independent, whereas it depends on scale for larger scales. This is true for for all the three models. At higher redshift (in matter dominated era), the growth rate $f$ for tachyon models is higher than the $\Lambda CDM$ model, and as evolution approaches dark energy dominated era, growth rate falls, even below the value for $\Lambda CDM$ model. To show

the agreement between theory and observation, we calculated $f\sigma_8(z)$ for the three models and compared it with RSD data. We find that the tachyon models are in good agreement with the data. If the value of parameter $\phi_{in}H_0$ is small (or $w_{\phi 0}$ is large), the tachyon models show significant difference from the $\Lambda CDM$ model. As $w_{\phi 0} \to -1$, for larger $\phi_{in}H_0$, tachyon models coincide with the $\Lambda CDM$ model.

The tachyon dark energy density contrast, $\delta_\phi < 10^{-4}\delta_m$ at scales $\lambda_p < 10^3\ Mpc$ with both the potentials. Therefore at these sub-Hubble scales, dark energy inhomogeneities can be neglected. If the dark energy equation of state $w_{\phi 0} \neq -1$, then at Hubble and super-Hubble scales, $\delta_\phi$ become significant. For example at the scale of $\lambda_p = 10^5\ Mpc$, for $\phi_{in}H_0 = 0.8$ the ratio $(\delta_\phi/\delta_m)_{z=0} = 0.2645$ and 0.1060 for the inverse square and the exponential potential respectively. Since at these scales $\delta_m$ itself very small, $\delta_\phi$ contributes significantly.

We constrain the free parameters of the $\Lambda CDM$ model as well as tachyon model with both the potentials using Redshift Space Distortion data. For the tachyon model, we constrain $\Omega_{m0}$, $\phi_{in}H_0$ and $\sigma_8(0)$. We find that there is a lower bound on $\phi_{in}H_0$ and all larger values are allowed by the RSD data. This feature has also been seen in analysis with the background data [158]. The smaller value of $\phi_{in}H_0$ implies a larger value of $w_{\phi 0}$ and a larger $(\delta_\phi/\delta_m)_{z=0}$. We therefore conclude that growth-rate data allows for perturbations in dark energy. In the $\Omega_{m0} - \sigma_8(0)$ plane, we find that there is a tension of $2.9\sigma$ ($2.26\sigma$) between the redshift space distortion data and Planck-2015 (Planck-2018) best fit value for $\Lambda CDM$ model. A similar result has also been reported in [9]. This tension is reduced slightly, when $w_{\phi 0} \neq -1$ and perturbations in dark energy are considered, for the tachyon models. This is true for both the potentials. We compare tachyon models with $\Lambda CDM$ model by calculating the ratio of the Bayesian evidences or the Bayes factor $B_{01}$. We find that the tachyon models are as good as the $\Lambda CDM$ model to satisfy the RSD data we use.

# Chapter 4

# Summary and Future Directions

In this thesis, we present a detailed study of cosmological consequences of a tachyon scalar field dark energy. This field is a viable model, and it has been shown that the tachyon scalar field can effectively explain dark energy. Apart from explaining accelerated expansion, an important property of this model is that its equation of state becomes dust like at early times, i.e., the equation of state parameter becomes zero in the past. This 'tachyon dust' can potentially be a candidate of combined dark energy and dark matter. The dynamics of the Universe in this case are driven by what is known as the 'runaway' potential. This model is consistent with the observations and constraints on the parameters are stringent. The theoretical problems and observational inconsistencies that $\Lambda CDM$ model suffers from are less severe in this model. These considerations make this description of dark energy an interesting alternative to both fluid and canonical scalar field models.

In the first part of this work, we have used two runaway potentials, an inverse square potential and an exponential potential, and revisit the constraints on their parameters as well as on the other cosmological parameters. For this work we set our initial condition at present epoch and solve dynamical equations backward in time, i.e., with increasing redshift. We find the constraints on the present value of the tachyon scalar field and the equation of state parameter of dark energy for these potentials. We also constrain the present day matter density parameter for these models. We restrict ourselves to low redshift data. We use the Baryon acoustic Oscillation data (from SDSS DR12, 6dFGS, SDSS DR7, WingleZ surveys), direct measurement of Hubble parameter (H(z)) data and Supernova-Ia Union 2.1 data. These are diverse data sets and are complementary to one another. We find that the present day matter density parameter is constrained to the values $\Omega_{m0} = 0.285^{+0.023}_{-0.022}$ at the $3\sigma$ confidence for both the potentials. The value of $\Omega_{m0}$ for tachyon model

is in agreement with its value for flat $\Lambda CDM$ model constrained using the JLA data within $1\sigma$. However, there is a tension with constraints from Planck and BAO DR12 data .

The data puts only a lower bound on the parameter $\phi_0 H_0$ ($\phi_0$ is the present value of the tachyon field and $H_0$ is the Hubble constant) which is oder unity, and all larger values are allowed. This way, we need not fine-tune this parameter to get present day accelerated expansion. The parameters $w_{\phi 0}$ ( the present day equation of state parameter ) and $\phi_0 H_0$ are correlated. As we increase the value of $\phi_0 H_0$ the present equation of state of dark energy $w_{\phi 0} \to -1$. Therefore, for sufficiently larger values of $\phi_0 H_0$, the tachyon models are capable of mimicking a cosmological constant like equation of state. Setting up the constraints on the parameters, we explore the evolution of the Universe in the past and in the future. We find that for tachyon model, the Universe goes through a transition from decelerated to accelerated expansion between redshifts $0.61 \lesssim z_{ac} \lesssim 0.80$. For tachyon model with exponential potential the equation of state $w_\phi$ rises to value larger than $-1/3$ (for smaller value of $\phi_0 H_0$ ) in future, and the Universe once again goes to a decelerating phase. Therefore, in the case of this potential there is no 'future horizon problem'. We find that constraints on tachyon models are stringent and these are as good as $\Lambda CDM$ model to be consistent with the low redshift data we have used. Background data alone can not rule out degeneracy between models. We study effect of perturbations in tachyon dark energy in oder to get constraints on parameters from observations beyond distance measurements.

In the second part of this work, we have focused on the growth of structure in the Universe in presence of a perturbed tachyon dark energy. The field equations remain invariant under gauge transformation, therefor we are free to choose any frame to work with. Going from one frame to other and by scaling coordinates, we can make small perturbations large and vice versa. To fix this problem, we choose to work in a fixed gauge and calculate all physical quantities of interest in it. We use the Newtonian conformal gauge and solve the Einstein's equations considering all perturbed quantities up to linear oder. We consider perturbation in scalar field as $\phi(\bar{x}, t) = \bar{\phi}(t) + \delta\phi(\bar{x}, t)$, and derive dynamical equation for perturbed part of the scalar field $\delta\phi(\bar{x}, t)$ using conservation of energy-momentum tensor. We set our initial condition at just after epoch of decoupling, $z = 1000$, considering dark energy initially homogeneous. We use the same two tachyon potentials that have been used in background dynamics study. We set $\Omega_{m0} = 0.285$, the best fit value by background data, and $\phi_{in} H_0 \approx \phi_0 H_0$. The results for these models are then compared with the results for $\Lambda CDM$ model.

The gravitational potential remains constant in the matter dominated era, but in dark energy dominated era it decays. For tachyon model, this phenomenon is scale dependent in contrast to $\Lambda CDM$ model. At sub-Hubble scales, all three models show similar behavior, but at Hubble and super-Hubble scales they show significant difference. At sub-Hubble scales matter density contrast $\delta_m \propto a$ in matter dominated era for all three models. As the dark energy starts to dominate, its growth is suppressed, as gravitational potential decays. Dark energy density contrast $\delta_\phi$ evolves at the same rate at all scales in matter dominated era, whereas in dark energy dominated era it is suppressed. At larger scales the $\delta_\phi$ is higher in magnitude than it is for the shorter scales; this behavior is opposite to that of the matter sector. At sub-Hubble scales, evolution of linear growth factor $D_m^+ = \delta_m/\delta_{m0}$ is scale independent in all the three models, but at larger scales it is scale dependent. For smaller value of the parameter $\phi_{in}H_0$ ($w_{\phi 0} > -1$) these models show significant difference, but for larger value of this parameter, $w_{\phi 0} \to -1$ and all three models coincide.

We also study evolution of the logarithmic growth rate $f = \frac{d\ ln\ \delta_m}{d\ ln\ a}$. The growth rate decreases as we go to larger and larger scales. In the matter-dominated era, the growth rate is higher for tachyon models, than it is for the $\Lambda CDM$ model at all scales. In recent past, growth rate starts slowing down, and for tachyon models it decays so fast that it comes below $\Lambda CDM$ model. To compare with observations, we calculate $f\sigma_8(z)$ for all three models, and compare it with redshift space distortion (RSD) data. We find all these models are in good agreement with data, and as $w_{\phi 0} \to -1$ these models are indistinguishable. We also study the effect of early perturbation in dark energy by varying the parameter $w_{\phi_{in}}$. We find that early perturbations in dark energy show damped oscillation and die out first. There is no effect on the growth of matter at sub-Hubble scales. These effects are only visible at larger scales. Using the RSD data, we constrain the parameters of the models as well as $\Omega_{m0}$ and $\sigma_8(0)$. We find that there is a tension of $\approx 3\sigma$ between RSD growth rate data and Planck-2.15/2018 CMB data for $\Lambda CDM$ model. For tachyon models this tension is reduced bellow $2\sigma$ level. Finally, comparing the ratio $(\delta_\phi/\delta_m)_{z=0}$ at different scales, we find that although the clustering in dark energy at sub-Hubble scales ($\lambda_p < 1000\ Mpc$) is insignificant as compared to matter clustering, it becomes significant at Hubble and super-Hubble scales.

At small scales, dark energy can be considered homogeneous, but different backgrounds can make a difference. Therefore, the next step in this study would be to compare the effect of different dark energy models on evolution of matter clustering and parameter constrain. Only background observation can not remove the degeneracy between models. Perturbation can break the degeneracy via the 'Integrated

Sachs-Wolf Effect' (ISW effect), since it affects the low $l$ CMB angular power spectrum. Since the dark energy perturbations are significant at scales comparable to the Hubble radius, its effects are expected to be seen prominently in the ISW effect. Therefore, it is important to investigate ISW effect in tachyon model and compare it with other dynamical dark energy models. One can investigate the possibility of getting the ISW signal in the CMB temperature anisotropies by cross-correlating with large-scale structure surveys. Using the cross-correlation data of the ISW signal with other background and growth-rate data, we can constrain cosmological parameters. We can therefore attempt to rule out or compare different dark energy models. Since tachyon models are viable cosmological models, various aspects of tachyon cosmology merits further study.

# Appendix A

# Appendix : Permission to Re-use Figures

## A.0.1 License agreement to reuse figures 1.1 and 1.2



Copyright Clearance Center Marketplace™

### IOP Publishing, Ltd - License Terms and Conditions

This is a License Agreement between Avinash Singh ("You") and IOP Publishing, Ltd ("Publisher") provided by Copyright Clearance Center ("CCC"). The license consists of your order details, the terms and conditions provided by IOP Publishing, Ltd, and the CCC terms and conditions.

All payments must be made in full to CCC.

| | | | |
|---|---|---|---|
| **Order Date** | 01-Jun-2020 | **Type of Use** | Republish in a thesis/dissertation |
| **Order license ID** | 1038599-1 | **Publisher** | IOP Publishing |
| **ISSN** | 0034-4885 | **Portion** | Chart/graph/table/figure |

LICENSED CONTENT

| | | | |
|---|---|---|---|
| **Publication Title** | Reports on Progress in Physics | **Country** | United Kingdom of Great Britain and Northern Ireland |
| **Author/Editor** | Institute of Physics (Great Britain), Physical Society (Great Britain), Institute of Physics and the Physical Society., Institute of Physics Publishing. | **Rightsholder** | IOP Publishing, Ltd |
| | | **Publication Type** | Journal |
| **Date** | 01/01/1934 | | |
| **Language** | English | | |

REQUEST DETAILS

| | | | |
|---|---|---|---|
| **Portion Type** | Chart/graph/table/figure | **Distribution** | Worldwide |
| **Number of charts / graphs / tables / figures requested** | 2 | **Translation** | Original language of publication |
| | | **Copies for the disabled?** | No |
| **Format (select all that apply)** | Print, Electronic | | |

| | | | |
|---|---|---|---|
| **Who will republish the content?** | Academic institution | **Minor editing privileges?** | No |
| **Duration of Use** | Life of current edition | **Incidental promotional use?** | No |
| **Lifetime Unit Quantity** | Up to 499 | **Currency** | USD |
| **Rights Requested** | Main product | | |

NEW WORK DETAILS

| | | | |
|---|---|---|---|
| **Title** | Aspects of tachyon field cosmology | **Institution name** | Indian Institute of Science Education and Research, Mohali, India. |
| **Instructor name** | H. K. Jassal | **Expected presentation date** | 2020-09-30 |

ADDITIONAL DETAILS

| | | | |
|---|---|---|---|
| **Order reference number** | N/A | **The requesting person / organization to appear on the license** | Avinash Singh |

REUSE CONTENT DETAILS

| | | | |
|---|---|---|---|
| **Title, description or numeric reference of the portion(s)** | Figure 3 and Figure 4 on page 5 | **Title of the article/chapter the portion is from** | Dark energy two decades after: observables, probes, consistency tests |
| **Editor of portion(s)** | N/A | **Author of portion(s)** | Dragan Huterer and Daniel L Shafer |
| **Volume of serial or monograph** | 81 | **Issue, if republishing an article from a serial** | Rep. Prog. Phys. 81 (2018) 016901 |
| **Page or page range of portion** | 5 | **Publication date of portion** | 2017-12-12 |

PUBLISHER TERMS AND CONDITIONS



## A.0.2 License agreement to reuse figure 1.5

Copyright Clearance Center Marketplace™

## Annual Reviews, Inc. - License Terms and Conditions

This is a License Agreement between Avinash Singh ("You") and Annual Reviews, Inc. ("Publisher") provided by Copyright Clearance Center ("CCC"). The license consists of your order details, the terms and conditions provided by Annual Reviews, Inc., and the CCC terms and conditions.

All payments must be made in full to CCC.

| | | | |
|---|---|---|---|
| **Order Date** | 01-Jun-2020 | **Type of Use** | Republish in a thesis/dissertation |
| **Order license ID** | 1038598-1 | **Publisher** | ANNUAL REVIEWS |
| **ISSN** | 1545-4282 | **Portion** | Chart/graph/table/figure |

### LICENSED CONTENT

| | | | |
|---|---|---|---|
| **Publication Title** | Annual review of astronomy and astrophysics | **Rightsholder** | Annual Reviews, Inc. |
| | | **Publication Type** | e-Journal |
| **Date** | 01/01/1963 | **URL** | http://arjournals.annualreviews.org/loi/astro |
| **Language** | English | | |
| **Country** | United States of America | | |

### REQUEST DETAILS

| | | | |
|---|---|---|---|
| **Portion Type** | Chart/graph/table/figure | **Distribution** | Worldwide |
| **Number of charts / graphs / tables / figures requested** | 1 | **Translation** | Original language of publication |
| | | **Copies for the disabled?** | No |
| **Format (select all that apply)** | Print, Electronic | **Minor editing privileges?** | No |
| **Who will republish the content?** | Academic institution | **Incidental promotional use?** | No |
| **Duration of Use** | Life of current edition | **Currency** | USD |





| | |
|---|---|
| **Lifetime Unit Quantity** | Up to 499 |
| **Rights Requested** | Main product |

### NEW WORK DETAILS

| | | | |
|---|---|---|---|
| **Title** | Aspects of tachyon field cosmology | **Institution name** | Indian Institute of Science Education and Research, Mohali, India |
| **Instructor name** | H. K. Jassal | **Expected presentation date** | 2020-09-30 |

### ADDITIONAL DETAILS

| | | | |
|---|---|---|---|
| **Order reference number** | N/A | **The requesting person / organization to appear on the license** | Avinash Singh |

### REUSE CONTENT DETAILS

| | | | |
|---|---|---|---|
| **Title, description or numeric reference of the portion(s)** | Figure 3. Growth of linear density perturbations in a flat universe with dark energy. | **Title of the article/chapter the portion is from** | Dark Energy and the Accelerating Universe |
| | | **Author of portion(s)** | Joshua A. Frieman, Michael S. Turner and Dragan Huterer |
| **Editor of portion(s)** | N/A | | |
| **Volume of serial or monograph** | N/A | **Issue, if republishing an article from a serial** | Annu. Rev. Astron. Astrophys. 2008. 46:385–432 |
| **Page or page range of portion** | 391 | **Publication date of portion** | 2008-06-03 |

## CCC Republication Terms and Conditions

1. Description of Service; Defined Terms. This Republication License enables the User to obtain licenses for republication of one or more copyrighted works as described in detail on the relevant Order Confirmation (the "Work(s)"). Copyright Clearance Center, Inc. ("CCC") grants licenses through the Service on behalf of the rightsholder identified on the Order Confirmation (the "Rightsholder"). "Republication", as used herein, generally

## A.0.3 License agreement to reuse figure 1.7

**American Physical Society**
**Reuse and Permissions License**

31-May-2020

This license agreement between the American Physical Society ("APS") and Avinash Singh ("You") consists of your license details and the terms and conditions provided by the American Physical Society and SciPris.

**Licensed Content Information**

| | |
|---|---|
| **License Number:** | **RNP/20/MAY/026381** |
| **License date:** | 31-May-2020 |
| **DOI:** | 10.1103/PhysRevD.93.103503 |
| **Title:** | Comparison of thawing and freezing dark energy parametrizations |
| **Author:** | G. Pantazis, S. Nesseris, and L. Perivolaropoulos |
| **Publication:** | Physical Review D |
| **Publisher:** | American Physical Society |
| **Cost:** | USD $ 0.00 |

**Request Details**

**Does your reuse require significant modifications**: No

| | |
|---|---|
| **Specify intended distribution locations:** | Worldwide |
| **Reuse Category:** | Reuse in a thesis/dissertation |
| **Requestor Type:** | Student |
| **Items for Reuse:** | Figures/Tables |
| **Number of Figure/Tables:** | 1 |
| **Figure/Tables Details:** | Fig. 1. hawing and freezing quintessence models (dottedcurves) with corresponding best CPL curves (continuous curves). |
| **Format for Reuse:** | Print and Electronic |
| **Total number of print copies:** | Up to 1000 |

**Information about New Publication:**

| | |
|---|---|
| **University/Publisher:** | Indian Institute of Science Education and Reserch, Mohali, India |
| **Title of dissertation/thesis:** | Aspects of tachyon field cosmology |
| **Author(s):** | Avinash Singh |
| **Expected completion date:** | Sep. 2020 |

**License Requestor Information**

| | |
|---|---|
| **Name:** | Avinash Singh |
| **Affiliation:** | Individual |
| **Email Id:** | avinashsingh@iisermohali.ac.in |
| **Country:** | India |

# Bibliography


[1] D. Scolnic, S. Casertano, A. Riess, A. Rest, E. Schlafly, R. J. Foley et al., *Supercal: Cross-calibration of Multiple Photometric Systems to Improve Cosmological Measurements with Type Ia Supernovae*, *ApJ* **815** (2015) 117 [1508.05361].

[2] S. Alam, M. Ata, S. Bailey, F. Beutler, D. Bizyaev, J. A. Blazek et al., *The clustering of galaxies in the completed SDSS-III Baryon Oscillation Spectroscopic Survey: cosmological analysis of the DR12 galaxy sample*, *Monthly Notices of the Royal Astronomical Society* **470** (2017) 2617.

[3] D. Huterer and D. L. Shafer, *Dark energy two decades after: observables, probes, consistency tests*, *Reports on Progress in Physics* **81** (2017) 016901.

[4] S. Perlmutter, G. Aldering, G. Goldhaber, R. A. Knop, P. Nugent, P. G. Castro et al., *Measurements of $\Omega$ and $\Lambda$ from 42 high-redshift supernovae*, *The Astrophysical Journal* **517** (1999) 565.

[5] A. G. Riess, A. V. Filippenko, P. Challis, A. Clocchiatti, A. Diercks, P. M. Garnavich et al., *Observational evidence from supernovae for an accelerating universe and a cosmological constant*, *The Astronomical Journal* **116** (1998) 1009.

[6] P. J. E. Peebles, *Tests of cosmological models constrained by inflation*, *ApJ* **284** (1984) 439.

[7] S. M. Carroll, W. H. Press and E. L. Turner, *The cosmological constant*, *Annual Review of Astronomy and Astrophysics* **30** (1992) 499.

[8] S. M. Carroll, *The Cosmological constant*, *Living Rev. Rel.* **4** (2001) 1 [astro-ph/0004075].

[9] S. Nesseris, G. Pantazis and L. Perivolaropoulos, *Tension and constraints on modified gravity parametrizations of $G_{\rm eff}(z)$ from growth rate and planck data*, *Phys. Rev. D* **96** (2017) 023542.

[10] H. K. Jassal, J. S. Bagla and T. Padmanabhan, *Observational constraints on low redshift evolution of dark energy: How consistent are different observations?*, *Phys. Rev. D* **72** (2005) 103503.

[11] G. Efstathiou, *Constraining the equation of state of the Universe from distant Type Ia supernovae and cosmic microwave background anisotropies*, *Monthly Notices of the Royal Astronomical Society* **310** (1999) 842.

[12] S. Lee, *Constraints on the dark energy equation of state from the separation of CMB peaks and the evolution of $\alpha$*, *Phys. Rev. D* **71** (2005) 123528.

[13] A. Tripathi, A. Sangwan and H. K. Jassal, *Dark energy equation of state parameter and its evolution at low redshift*, *JCAP* **1706** (2017) 012 [1611.01899].

[14] A. Sangwan, A. Mukherjee and H. K. Jassal, *Reconstructing the dark energy potential*, *JCAP* **1801** (2018) 018 [1712.05143].

[15] W. Zheng and H. Li, *Constraints on parameterized dark energy properties from new observations with principal component analysis*, *Astroparticle Physics* **86** (2017) 1 .

[16] M. Rezaei, M. Malekjani, S. Basilakos, A. Mehrabi and D. F. Mota, *Constraints to Dark Energy Using PADE Parameterizations*, *The Astrophysical Journal* **843** (2017) 65.

[17] W. Yang, S. Pan and A. Paliathanasis, *Latest astronomical constraints on some non-linear parametric dark energy models*, *Monthly Notices of the Royal Astronomical Society* **475** (2018) 2605.

[18] B. Ratra and P. J. E. Peebles, *Cosmological Consequences of a Rolling Homogeneous Scalar Field*, *Phys. Rev.* **D37** (1988) 3406.

[19] E. V. Linder, *The Dynamics of Quintessence, The Quintessence of Dynamics*, *Gen. Rel. Grav.* **40** (2008) 329 [0704.2064].

[20] D. Huterer and H. V. Peiris, *Dynamical behavior of generic quintessence potentials: Constraints on key dark energy observables*, *Phys. Rev.* **D75** (2007) 083503 [astro-ph/0610427].

[21] I. Zlatev, L.-M. Wang and P. J. Steinhardt, *Quintessence, cosmic coincidence, and the cosmological constant*, *Phys. Rev. Lett.* **82** (1999) 896 [astro-ph/9807002].

[22] E. J. Copeland, A. R. Liddle and D. Wands, *Exponential potentials and cosmological scaling solutions*, *Phys. Rev.* **D57** (1998) 4686 [gr-qc/9711068].

[23] A. Sangwan, A. Tripathi and H. K. Jassal, *Observational constraints on quintessence models of dark energy*, 1804.09350.

[24] C. R. Watson and R. J. Scherrer, *The Evolution of inverse power law quintessence at low redshift*, *Phys. Rev.* **D68** (2003) 123524 [astro-ph/0306364].

[25] R. J. Scherrer and A. A. Sen, *Thawing quintessence with a nearly flat potential*, *Phys. Rev.* **D77** (2008) 083515 [0712.3450].

[26] S. Unnikrishnan, H. K. Jassal and T. R. Seshadri, *Scalar field dark energy perturbations and their scale dependence*, *Phys. Rev. D* **78** (2008) 123504.

[27] H. K. Jassal, *Comparison of perturbations in fluid and scalar field models of dark energy*, *Phys. Rev. D* **79** (2009) 127301.

[28] H. K. Jassal, *Evolution of perturbations in distinct classes of canonical scalar field models of dark energy*, *Phys. Rev. D* **81** (2010) 083513.

[29] H. K. Jassal, *Scalar field dark energy perturbations and the integrated sachs-wolfe effect*, *Phys. Rev. D* **86** (2012) 043528.

[30] C. Armendariz-Picon, T. Damour and V. Mukhanov, *k-Inflation*, *Physics Letters B* **458** (1999) 209 [hep-th/9904075].

[31] C. Armendariz-Picon, V. Mukhanov and P. J. Steinhardt, *Dynamical solution to the problem of a small cosmological constant and late-time cosmic acceleration*, *Phys. Rev. Lett.* **85** (2000) 4438.

[32] C. Armendariz-Picon, V. Mukhanov and P. J. Steinhardt, *Essentials of k-essence*, *Phys. Rev. D* **63** (2001) 103510.

[33] T. Chiba, T. Okabe and M. Yamaguchi, *Kinetically driven quintessence*, *Phys. Rev. D* **62** (2000) 023511.

[34] A. Sen, *Rolling tachyon*, *Journal of High Energy Physics* **2002** (2002) 048.

[35] A. Sen, *Tachyon matter*, *Journal of High Energy Physics* **2002** (2002) 065.

[36] A. SEN, *Field theory of tachyon matter*, *Modern Physics Letters A* **17** (2002) 1797.

[37] J. S. Bagla, H. K. Jassal and T. Padmanabhan, *Cosmology with tachyon field as dark energy*, *Phys. Rev. D* **67** (2003) 063504.

[38] T. Padmanabhan, *Accelerated expansion of the universe driven by tachyonic matter*, *Phys. Rev. D* **66** (2002) 021301.

[39] G. Calcagni and A. R. Liddle, *Tachyon dark energy models: Dynamics and constraints*, *Phys. Rev. D* **74** (2006) 043528.

[40] M. Fairbairn and M. H. Tytgat, *Inflation from a tachyon fluid?*, *Physics Letters B* **546** (2002) 1 .

[41] L. Kofman and A. Linde, *Problems with tachyon inflation*, *Journal of High Energy Physics* **2002** (2002) 004.

[42] A. Feinstein, *Power-law inflation from the rolling tachyon*, *Phys. Rev. D* **66** (2002) 063511.

[43] K. Rezazadeh, K. Karami and S. Hashemi, *Tachyon inflation with steep potentials*, *Phys. Rev. D* **95** (2017) 103506.

[44] N. Barbosa-Cendejas, J. De-Santiago, G. German, J. C. Hidalgo and R. R. Mora-Luna, *Tachyon inflation in the large- n formalism*, *Journal of Cosmology and Astroparticle Physics* **2015** (2015) 020.

[45] Q. Fei, Y. Gong, J. Lin and Z. Yi, *The reconstruction of tachyon inflationary potentials*, *Journal of Cosmology and Astroparticle Physics* **2017** (2017) 018.

[46] Q. Gao, Y. Gong and Q. Fei, *Constant-roll tachyon inflation and observational constraints*, *Journal of Cosmology and Astroparticle Physics* **2018** (2018) 005.

[47] N. Barbosa-Cendejas, J. De-Santiago, G. German, J. C. Hidalgo and R. R. Mora-Luna, *Theoretical and observational constraints on tachyon inflation*, *Journal of Cosmology and Astroparticle Physics* **2018** (2018) 015.

[48] T. Padmanabhan and T. R. Choudhury, *Can the clustered dark matter and the smooth dark energy arise from the same scalar field?*, *Phys. Rev. D* **66** (2002) 081301.

[49] S. Sugimoto and S. Terashima, *Tachyon matter in boundary string field theory*, *Journal of High Energy Physics* **2002** (2002) 025.

[50] A. Das and A. DeBenedictis, *Inhomogeneous cosmologies with tachyonic dust as dark matter*, *General Relativity and Gravitation* **36** (2004) 1741.

[51] P. C. W. Davies, *Tachyonic dark matter*,
*International Journal of Theoretical Physics* **43** (2004) 141.

[52] M. A. Makukov, E. G. Mychelkin and V. L. Saveliev, *On possible tachyonic state of neutrino dark matter*,
*International Journal of Modern Physics: Conference Series* **41** (2016) 1660133.

[53] J. Weller and A. M. Lewis, *Large-scale cosmic microwave background anisotropies and dark energy*,
*Monthly Notices of the Royal Astronomical Society* **346** (2003) 987.

[54] R. Bean and O. Doré, *Probing dark energy perturbations: The dark energy equation of state and speed of sound as measured by wmap*,
*Phys. Rev. D* **69** (2004) 083503.

[55] T. Padmanabhan, *Theoretical Astrophysics - Volume 3, Galaxies and Cosmology*. Dec., 2002, 10.2277/0521562422.

[56] P. J. E. Peebles, *Principles of physical cosmology*. Princeton University Press, 1993.

[57] S. Carroll, *Spacetime and Geometry: An Introduction to General Relativity*. Addison-Wesley, 2003.

[58] P. Schneider, *Extragalactic Astronomy and Cosmology*. 2006.

[59] E. Hubble, *A relation between distance and radial velocity among extra-galactic nebulae*, .

[60] Planck Collaboration, N. Aghanim, Y. Akrami, M. Ashdown, J. Aumont, C. Baccigalupi et al., *Planck 2018 results- VI. Cosmological parameters*, *arXiv e-prints* (2018) arXiv:1807.06209 [1807.06209].

[61] E. Komatsu, J. Dunkley, M. R. Nolta, C. L. Bennett, B. Gold, G. Hinshaw et al., *Five-Year Wilkinson Microwave Anisotropy Probe Observations: Cosmological Interpretation*, *ApJS* **180** (2009) 330 [0803.0547].

[62] O. Farooq and B. Ratra, *Hubble parameter measurement constraints on the cosmological deceleration-acceleration transition redshift*, *The Astrophysical Journal Letters* **766** (2013) L7.

[63] S. Perlmutter, S. Gabi, G. Goldhaber, A. Goobar, D. E. Groom, I. M. Hook et al., *Measurements of the cosmological parameters $\Omega$ and $\Lambda$ from the first seven supernovae at $z \leq 0.35$*, *The Astrophysical Journal* **483** (1997) 565.

[64] J. A. Frieman, M. S. Turner and D. Huterer, *Dark energy and the accelerating universe*, *Annual Review of Astronomy and Astrophysics* **46** (2008) 385.

[65] T. Padmanabhan, *Cosmological constant-the weight of the vacuum*, *Physics Reports* **380** (2003) 235 .

[66] Planck Collaboration, Ade, P. A. R., Aghanim, N., Arnaud, M., Ashdown, M., Aumont, J. et al., *Planck 2015 results - XIII. Cosmological parameters*, *A&A* **594** (2016) A13.

[67] S. M. Carroll, *The cosmological constant*, *Living Reviews in Relativity* **4** (2001) 1.

[68] M. Chevallier and D. Polarski, *Accelerating Universes with Scaling Dark Matter*, *International Journal of Modern Physics D* **10** (2001) 213 [gr-qc/0009008].

[69] E. V. Linder, *Exploring the expansion history of the universe*, *Phys. Rev. Lett.* **90** (2003) 091301.

[70] H. K. Jassal, J. S. Bagla and T. Padmanabhan, *WMAP constraints on low redshift evolution of dark energy*, *Mon. Not. Roy. Astron. Soc.* **356** (2005) L11 [astro-ph/0404378].

[71] L. Feng and T. Lu, *A new equation of state for dark energy model*, *Journal of Cosmology and Astroparticle Physics* **2011** (2011) 034.

[72] G. A. Baker and P. Graves-Morris, *Padé Approximants*, Encyclopedia of Mathematics and its Applications. Cambridge University Press, 2 ed., 1996, 10.1017/CBO9780511530074.

[73] H. Wei, X.-P. Yan and Y.-N. Zhou, *Cosmological applications of Padé approximant*, *Journal of Cosmology and Astroparticle Physics* **2014** (2014) 045.

[74] X. Li and A. Shafieloo, *A simple phenomenological emergent dark energy model can resolve the hubble tension*, *The Astrophysical Journal* **883** (2019) L3.

[75] S. Hannestad and E. Mörtsell, *Cosmological constraints on the dark energy equation of state and its evolution*, *Journal of Cosmology and Astroparticle Physics* **2004** (2004) 001.

[76] Y. Wang and M. Tegmark, *New dark energy constraints from supernovae, microwave background, and galaxy clustering*, *Phys. Rev. Lett.* **92** (2004) 241302.

[77] G. Pantazis, S. Nesseris and L. Perivolaropoulos, *Comparison of thawing and freezing dark energy parametrizations*, *Phys. Rev. D* **93** (2016) 103503.

[78] R. R. Caldwell and E. V. Linder, *The Limits of quintessence*, *Phys. Rev. Lett.* **95** (2005) 141301 [astro-ph/0505494].

[79] G. Gupta, R. Rangarajan and A. A. Sen, *Thawing quintessence from the inflationary epoch to today*, *Phys. Rev. D* **92** (2015) 123003.

[80] S. Dutta and R. J. Scherrer, *Slow-roll freezing quintessence*, *Phys. Lett.* **B704** (2011) 265 [1106.0012].

[81] M. Sahlén, A. R. Liddle and D. Parkinson, *Quintessence reconstructed: New constraints and tracker viability*, *Phys. Rev. D* **75** (2007) 023502.

[82] Schimd, C., Tereno, I., Uzan, J.-P., Mellier, Y., van Waerbeke, L., Semboloni, E. et al., *Tracking quintessence by cosmic shear - constraints from virmos-descart and cfhtls and future prospects*, *A&A* **463** (2007) 405.

[83] T. Barreiro, B. d. Carlos and E. J. Copeland, *Nonperturbative corrections to the kähler potential*, *Phys. Rev. D* **57** (1998) 7354.

[84] P. Binétruy, *Models of dynamical supersymmetry breaking and quintessence*, *Phys. Rev. D* **60** (1999) 063502.

[85] F. Rosati, *Quintessential enhancement of dark matter abundance*, *Physics Letters B* **570** (2003) 5 .

[86] T. Ngampitipan and P. Wongjun, *Dynamics of three-form dark energy with dark matter couplings*, *Journal of Cosmology and Astroparticle Physics* **2011** (2011) 036.

[87] L. Amendola and S. Tsujikawa, *Dark Energy: Theory and Observations*. 2010.

[88] S. Dodelson, *Modern cosmology*. Academic Press, San Diego, CA, 2003.

[89] C.-P. Ma and E. Bertschinger, *Cosmological Perturbation Theory in the Synchronous and Conformal Newtonian Gauges*, *ApJ* **455** (1995) 7 [astro-ph/9506072].

[90] A. Liddle, *An introduction to modern cosmology*. Wiley, 2003.

[91] N. Kaiser, *Clustering in real space and in redshift space*, *MNRAS* **227** (1987) 1.

[92] B. Sagredo, S. Nesseris and D. Sapone, *Internal robustness of growth rate data*, *Phys. Rev. D* **98** (2018) 083543.

[93] A. R. Liddle, *Information criteria for astrophysical model selection*, *Monthly Notices of the Royal Astronomical Society: Letters* **377** (2007) L74.

[94] R. Trotta, *Applications of Bayesian model selection to cosmological parameters*, *Monthly Notices of the Royal Astronomical Society* **378** (2007) 72.

[95] L. Verde, *Statistical Methods in Cosmology*, vol. 800. 2010.

[96] R. Trotta, *Bayes in the sky: Bayesian inference and model selection in cosmology*, *Contemporary Physics* **49** (2008) 71.

[97] E. Kreyszig, *Advanced Engineering Mathematics*. John Wiley, Hoboken, NJ, ninth ed., 2006.

[98] H. Jeffreys, *Theory of Probability*. Oxford, England, 1961.

[99] H.-J. Seo and D. J. Eisenstein, *Probing dark energy with baryonic acoustic oscillations from future large galaxy redshift surveys*, *The Astrophysical Journal* **598** (2003) 720.

[100] W. J. Percival, R. C. Nichol, D. J. Eisenstein, J. A. Frieman, M. Fukugita, J. Loveday et al., *The Shape of the Sloan Digital Sky Survey Data Release 5 Galaxy Power Spectrum*, *The Astrophysical Journal* **657** (2007) 645.

[101] Busca, N. G., Delubac, T., Rich, J., Bailey, S., Font-Ribera, A., Kirkby, D. et al., *Baryon acoustic oscillations in the lyest of boss quasars*, *A&A* **552** (2013) A96.

[102] C. Blake, S. Brough, M. Colless, C. Contreras, W. Couch, S. Croom et al., *The wigglez dark energy survey: joint measurements of the expansion and growth history at $z < 1$*, *Monthly Notices of the Royal Astronomical Society* **425** (2012) 405.

[103] L. Anderson, Ã. Aubourg, S. Bailey, F. Beutler, V. Bhardwaj, M. Blanton et al., *The clustering of galaxies in the SDSS-III Baryon Oscillation Spectroscopic Survey: baryon acoustic oscillations in the Data Releases 10 and 11 Galaxy samples*, *Monthly Notices of the Royal Astronomical Society* **441** (2014) 24.

[104] A. Veropalumbo, F. Marulli, L. Moscardini, M. Moresco and A. Cimatti, *An improved measurement of baryon acoustic oscillations from the correlation function of galaxy clusters at $z \sim 0.3$*,
*Monthly Notices of the Royal Astronomical Society* **442** (2014) 3275.

[105] Delubac, Timothée, Bautista, Julian E., Busca, Nicolás G., Rich, James, Kirkby, David, Bailey, Stephen et al., *Baryon acoustic oscillations in the lyest of boss DR*11 *quasars*, *A&A* **574** (2015) A59.

[106] C.-H. Chuang, M. Pellejero-Ibanez, S. Rodríguez-Torres, A. J. Ross, G.-b. Zhao, Y. Wang et al., *The clustering of galaxies in the completed SDSS-III Baryon Oscillation Spectroscopic Survey: single-probe measurements from DR12 galaxy clustering - towards an accurate model*,
*MNRAS* **471** (2017) 2370 [1607.03151].

[107] BOSS collaboration, E. Aubourg, S. Bailey, J. E. Bautista, F. Beutler, V. Bhardwaj, D. Bizyaev et al., *Cosmological implications of baryon acoustic oscillation measurements*, *Phys. Rev. D* **92** (2015) 123516.

[108] C. Blake, E. A. Kazin, F. Beutler, T. M. Davis, D. Parkinson, S. Brough et al., *The wigglez dark energy survey: mapping the distance-redshift relation with baryon acoustic oscillations*,
*Monthly Notices of the Royal Astronomical Society* **418** (2011) 1707.

[109] D. J. Eisenstein, I. Zehavi, D. W. Hogg, R. Scoccimarro, M. R. Blanton, R. C. Nichol et al., *Detection of the baryon acoustic peak in the large-scale correlation function of sdss luminous red galaxies*, *The Astrophysical Journal* **633** (2005) 560.

[110] O. Farooq, F. R. Madiyar, S. Crandall and B. Ratra, *Hubble parameter measurement constraints on the redshift of the deceleration-acceleration transition, dynamical dark energy, and space curvature*, *The Astrophysical Journal* **835** (2017) 26.

[111] O. Farooq, D. Mania and B. Ratra, *Hubble parameter measurement constraints on dark energy*, *The Astrophysical Journal* **764** (2013) 138.

[112] L. Samushia and B. Ratra, *Cosmological constraints from hubble parameter versus redshift data*, *The Astrophysical Journal Letters* **650** (2006) L5.

[113] D. Stern, R. Jimenez, L. Verde, M. Kamionkowski and S. A. Stanford, *Cosmic chronometers: constraining the equation of state of dark energy. I: H ( z )*

*measurements*, *Journal of Cosmology and Astroparticle Physics* **2010** (2010) 008.

[114] M. Moresco, A. Cimatti, R. Jimenez, L. Pozzetti, G. Zamorani, M. Bolzonella et al., *Improved constraints on the expansion rate of the universe up to $z \sim 1.1$ from the spectroscopic evolution of cosmic chronometers*, *Journal of Cosmology and Astroparticle Physics* **2012** (2012) 006.

[115] C.-H. Chuang and Y. Wang, *Modelling the anisotropic two-point galaxy correlation function on small scales and single-probe measurements of $H(z)$, $DA(z)$ and $f(z)\sigma_8(z)$ from the sloan digital sky survey DR7 luminous red galaxies*,
*Monthly Notices of the Royal Astronomical Society* **435** (2013) 255.

[116] Y. Chen and B. Ratra, *Hubble parameter data constraints on dark energy*, *Physics Letters B* **703** (2011) 406 .

[117] C. Zhang, H. Zhang, S. Yuan, S. Liu, T.-J. Zhang and Y.-C. Sun, *Four new observational H(z) data from luminous red galaxies in the Sloan Digital Sky Survey data release seven*,
*Research in Astronomy and Astrophysics* **14** (2014) 1221 [1207.4541].

[118] J. Simon, L. Verde and R. Jimenez, *Constraints on the redshift dependence of the dark energy potential*, *Phys. Rev. D* **71** (2005) 123001.

[119] M. Moresco, *Raising the bar: new constraints on the Hubble parameter with cosmic chronometers at $z \sim 2$* ,
*Monthly Notices of the Royal Astronomical Society: Letters* **450** (2015) L16.

[120] M. Moresco, L. Pozzetti, A. Cimatti, R. Jimenez, C. Maraston, L. Verde et al., *A 6% measurement of the hubble parameter at $z \sim 0.45$: direct evidence of the epoch of cosmic re-acceleration*,
*Journal of Cosmology and Astroparticle Physics* **2016** (2016) 014.

[121] A. Font-Ribera, D. Kirkby, N. Busca, J. Miralda-Escudé, N. P. Ross, A. Slosar et al., *Quasar-Lyman $\alpha$ forest cross-correlation from BOSS DR11: Baryon Acoustic Oscillations*,
*Journal of Cosmology and Astroparticle Physics* **2014** (2014) 027 [1311.1767].

[122] M. Guidry and B. Messer, *The physics and astrophysics of type ia supernova explosions*, *Frontiers of Physics* **8** (2013) 111.

[123] N. Suzuki, D. Rubin, C. Lidman, G. Aldering, R. Amanullah, K. Barbary et al., *The hubble space telescope cluster supernova survey. v. improving the dark-energy constraints above $z > 1$ and building an early-type-hosted supernova sample*, *The Astrophysical Journal* **746** (2012) 85.

[124] P. M. Garnavich, S. Jha, P. Challis, A. Clocchiatti, A. Diercks, A. V. Filippenko et al., *Supernova limits on the cosmic equation of state*, *The Astrophysical Journal* **509** (1998) 74.

[125] J. L. Tonry, B. P. Schmidt, B. Barris, P. Candia, P. Challis, A. Clocchiatti et al., *Cosmological results from high-z supernovae*, *The Astrophysical Journal* **594** (2003) 1.

[126] B. J. Barris, J. L. Tonry, S. Blondin, P. Challis, R. Chornock, A. Clocchiatti et al., *Twenty-three high-redshift supernovae from the institute for astronomy deep survey: Doubling the supernova sample at $z > 0.7$*, *The Astrophysical Journal* **602** (2004) 571.

[127] A. Goobar, S. Perlmutter, G. Goldhaber, R. A. Knop, P. Nugent, P. G. Castro et al., *The acceleration of the universe: Measurements of cosmological parameters from type ia supernovae*, *Physica Scripta* **2000** (2000) 47.

[128] S. González-Gaitán, A. Conley, F. B. Bianco, D. A. Howell, M. Sullivan, K. Perrett et al., *The rise time of normal and subluminous type ia supernovae*, *The Astrophysical Journal* **745** (2012) 44.

[129] Astier, P., Guy, J., Regnault, N., Pain, R., Aubourg, E., Balam, D. et al., *The supernova legacy survey: measurement of $\Omega_m, \Omega_\Lambda$ and w from the first year data set the first year data set*, *A&A* **447** (2006) 31.

[130] A. V. Filippenko, *Type Ia Supernovae and Cosmology*, pp. 97–133. Springer Netherlands, Dordrecht, 2005.

[131] Y.-S. Song and W. J. Percival, *Reconstructing the history of structure formation using redshift distortions*, *Journal of Cosmology and Astroparticle Physics* **2009** (2009) 004.

[132] D. Huterer, D. L. Shafer, D. M. Scolnic and F. Schmidt, *Testing ΛCDM at the lowest redshifts with SN ia and galaxy velocities*, *Journal of Cosmology and Astroparticle Physics* **2017** (2017) 015.

[133] S. J. Turnbull, M. J. Hudson, H. A. Feldman, M. Hicken, R. P. Kirshner and R. Watkins, *Cosmic flows in the nearby universe from Type Ia supernovae*, *Monthly Notices of the Royal Astronomical Society* **420** (2012) 447.

[134] M. J. Hudson and S. J. Turnbull, *The Growth Rate of Cosmic Structure from Peculiar Velocities at Low and High Redshifts*, *ApJL* **751** (2012) L30 [1203.4814].

[135] M. Davis, A. Nusser, K. L. Masters, C. Springob, J. P. Huchra and G. Lemson, *Local gravity versus local velocity: solutions for $\beta$ and non-linear bias*, *Monthly Notices of the Royal Astronomical Society* **413** (2011) 2906.

[136] M. Feix, A. Nusser and E. Branchini, *Growth rate of cosmological perturbations at $z \sim 0.1$ from a new observational test*, *Phys. Rev. Lett.* **115** (2015) 011301.

[137] C. Howlett, A. J. Ross, L. Samushia, W. J. Percival and M. Manera, *The clustering of the SDSS main galaxy sample - II. Mock galaxy catalogues and a measurement of the growth of structure from redshift space distortions at $z = 0.15$*, *Monthly Notices of the Royal Astronomical Society* **449** (2015) 848.

[138] C. Blake, I. K. Baldry, J. Bland-Hawthorn, L. Christodoulou, M. Colless, C. Conselice et al., *Galaxy And Mass Assembly (GAMA): improved cosmic growth measurements using multiple tracers of large-scale structure*, *Monthly Notices of the Royal Astronomical Society* **436** (2013) 3089.

[139] L. Samushia, W. J. Percival and A. Raccanelli, *Interpreting large-scale redshift-space distortion measurements*, *Monthly Notices of the Royal Astronomical Society* **420** (2012) 2102.

[140] A. G. Sánchez, F. Montesano, E. A. Kazin, E. Aubourg, F. Beutler, J. Brinkmann et al., *The clustering of galaxies in the SDSS-III Baryon Oscillation Spectroscopic Survey: cosmological implications of the full shape of the clustering wedges in the data release 10 and 11 galaxy samples*, *Monthly Notices of the Royal Astronomical Society* **440** (2014) 2692.

[141] C.-H. Chuang, F. Prada, M. Pellejero-Ibanez, F. Beutler, A. J. Cuesta, D. J. Eisenstein et al., *The clustering of galaxies in the SDSS-III Baryon Oscillation Spectroscopic Survey: single-probe measurements from CMASS anisotropic galaxy clustering*, *Monthly Notices of the Royal Astronomical Society* **461** (2016) 3781.

[142] Pezzotta, A., de la Torre, S., Bel, J., Granett, B. R., Guzzo, L., Peacock, J. A. et al., *The vimos public extragalactic redshift survey (vipers) - the growth of structure at $0.5 < z < 1.2$ from redshift-space distortions in the clustering of the pdr-2 final sample*, *A&A* **604** (2017) A33.

[143] G.-B. Zhao, Y. Wang, S. Saito, H. Gil-Marín, W. J. Percival, D. a. Wang et al., *The clustering of the SDSS-IV extended Baryon Oscillation Spectroscopic Survey DR14 quasar sample: a tomographic measurement of cosmic structure growth and expansion rate based on optimal redshift weights*, *MNRAS* **482** (2019) 3497 [1801.03043].

[144] T. Okumura, C. Hikage, T. Totani, M. Tonegawa, H. Okada, K. Glazebrook et al., *The Subaru FMOS galaxy redshift survey (FastSound). IV. New constraint on gravity theory from redshift space distortions at $z \sim 1.4$*, *Publications of the Astronomical Society of Japan* **68** (2016) .

[145] P. J. E. Peebles and B. Ratra, *Cosmology with a Time-Variable Cosmological "Constant"*, *ApJL* **325** (1988) L17.

[146] P. J. E. Peebles and B. Ratra, *The cosmological constant and dark energy*, *Rev. Mod. Phys.* **75** (2003) 559.

[147] E. J. Copeland, M. R. Garousi, M. Sami and S. Tsujikawa, *What is needed of a tachyon if it is to be the dark energy?*, *Phys. Rev. D* **71** (2005) 043003.

[148] J. M. Aguirregabiria and R. Lazkoz, *Tracking solutions in tachyon cosmology*, *Phys. Rev. D* **69** (2004) 123502.

[149] Y. Wang and S. Wang, *Distance priors from planck and dark energy constraints from current data*, *Phys. Rev. D* **88** (2013) 043522.

[150] Betoule, M., Kessler, R., Guy, J., Mosher, J., Hardin, D., Biswas, R. et al., *Improved cosmological constraints from a joint analysis of the SDSS-II and SNLS supernova samples*, *A&A* **568** (2014) A22.

[151] A. de la Macorra and C. Stephan-Otto, *Quintessence restrictions on negative power and condensate potentials*, *Phys. Rev. D* **65** (2002) 083520.

[152] I. Zlatev, L. Wang and P. J. Steinhardt, *Quintessence, cosmic coincidence, and the cosmological constant*, *Phys. Rev. Lett.* **82** (1999) 896.

[153] A. Riazuelo and J.-P. Uzan, *Quintessence and gravitational waves*, *Phys. Rev. D* **62** (2000) 083506.

[154] T. Matos and L. Arturo Ureña López, *Further analysis of a cosmological model with quintessence and scalar dark matter*, *Phys. Rev. D* **63** (2001) 063506.

[155] A. A. Sen, G. Gupta and S. Majumdar, *Constraining thawing quintessence*, *Monthly Notices of the Royal Astronomical Society* **420** (2012) 1309.

[156] P. G. Ferreira and M. Joyce, *Structure formation with a self-tuning scalar field*, *Phys. Rev. Lett.* **79** (1997) 4740.

[157] C. Wetterich, *An asymptotically vanishing time-dependent cosmological "constant".*, *A&A* **301** (1995) 321 [hep-th/9408025].

[158] A. Singh, A. Sangwan and H. Jassal, *Low redshift observational constraints on tachyon models of dark energy*, *Journal of Cosmology and Astroparticle Physics* **2019** (2019) 047.

[159] B. L'Huillier, A. Shafieloo, D. Polarski and A. A. Starobinsky, *Defying the laws of gravity I: model-independent reconstruction of the Universe expansion from growth data*, *MNRAS* **494** (2020) 819 [1906.05991].